Design and Implementation of
Discrete Type 1 and Type 2 Controllers with Residual Feedback for
Modal Adaptive Optics

by

Peter John Hampton
B. Eng., University of Victoria, 2002

A Thesis Submitted in Partial Fulfillment of
the Requirements for the Degree of

MASTER OF APPLIED SCIENCE

in the Department of Electrical and Computer Engineering

Supervisors: Dr. C. Bradley and Dr. P. Agathoklis

Abstract

This thesis deals with the design, implementation and experimental validation of digital controllers for an Adaptive Optics (AO) test bench. The AO model has been modeled using a discrete model and this model was validated using experimental measurements. The controllers developed consist of 1-D parallel controllers, one for each mode of the optical system. Two controllers were designed and analyzed for the system: (i) a Type 1 controller that exhibits improved bandwidth over standard AO controllers and (ii) a Type 2 controller that is capable of low frequency prediction and can provide exceptionally low following error if the quantization noise sources are sufficiently small.

The implementation of the controllers on the AO test bench was considered and the problems arising from the quantization of the output of the controller due to hardware limitations were studied. Controller implementations that improve the performance of the system with respect to stability despite the non-linear effects of the quantizer are provided.

The controllers developed were implemented and their performance was evaluated and compared with the results expected from theoretical analysis. The experimental results are very close to the ones expected from the theoretical analysis except when the quantization effects become significant.

Table of Contents

List of Tables

List of Figures

Abbreviations

ALTAIR	ALTitude conjugated Adaptive optics for Infra-Red
AO	Adaptive Optics
CAO	Classic Adaptive Optics
CCD	Charge Coupled Device. Converts light into proportional electric current
DM	Deformable Mirror
TG	Turbulence Generator
TT	Tip Tilt Mirror
UVic	University of Victoria
VLT	Very Large Telescope
WFS	Wave Front Sensor

Notation

Symbol	Usage
c	Small letter represent a scalar variable or constant
c^*	Complex conjugate of c
c_m	Indexed scalar coefficient
$c_{m,n}$	Scalar coefficient with two indices
$\hat{c}$	Estimate of c
$\bar{c}$	Vector
$f(x)$	Function of independent variable x
$f(x,y)$	Function of independent variables x and y
$f_{m,n}(x,y)$	Polynomial function with maximum power term of $x^m y^n$
$C(z)$	Function in the z (Discrete) domain
$C(s)$	Function in the s (Continuous) domain
C	Capital letter indicates a matrix or a maximum index
C_{MxN}	Matrix of size MxN
$G(\,)$	Open loop transfer function
$T(\,)$	Closed loop transfer function
$E(\,)$	Closed loop error transfer function
$Z\{\,\}$	Z transform of the function within { }
$F\{\,\}$	Fourier transform of the function within { }

Acknowledgements

I would like to thank my supervisors, Dr. Colin Bradley and Dr. Pan Agathoklis, for their guidance, insights and support that made this body of work possible. I'd also like to thank Dr. Rodolphe Conan for his constructive criticisms of these new controller designs and his imparted knowledge of adaptive optics.

I would also like to thank the other researchers that this work depended on; Brian Wallace, for the design, assembly and characterization of the adaptive optics system. Aaron Hilton, for developing the foundation of computer programs that my controller required. Jeff Kennedy, for fabricating many of the system components. Onur Keskin, for developing and characterizing the turbulence generator.

Last but certainly not least, I would like to thank the staff at the Herzburg Institute of Astrophysics. Particularly Glen Herriot and Dr. Jean-Pierre Véran for their guidance and instruction of adaptive optics applied to the Altair AO system, which started me on this path.

This work is dedicated, in loving memory, to my grandmother

Audrey Hunter

Chapter 1

Introduction

Adaptive optics (AO) is a technique that compensates for atmospheric turbulence by quickly adjusting the light path in the optics. Some applications of AO are ground based astronomy, ground observation satellites and laser communications. The AO system studied in this thesis is a model of a ground based telescope. An AO system enables the telescope to achieve much better resolution, closer to its theoretical resolving power.

The AO system developed at the University of Victoria is used to simulate and study an AO system. The five main components of this AO system are; the laser light source, the turbulence generator (TG), the tip tilt mirror (TT), the deformable mirror (DM), the wave front sensor (WFS) and the science camera. Beyond these components are the optics to properly magnify and conjugate the beam, as well as the iris. The optical design is described in detail in [1]. The effects of turbulence and the design of the TG are given in [2]. Both of these topics are beyond the scope of this thesis, but a short introduction is provided in Sections 1.3 to 1.6.

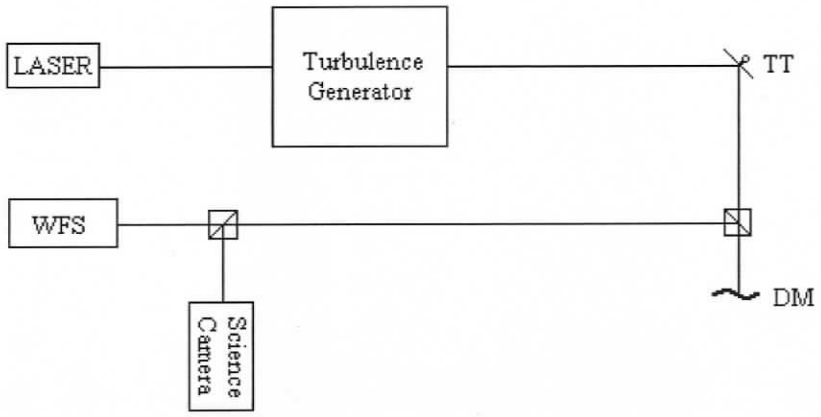

Figure 1.1: Simplified lay out of the basic components of the UVic AO system

1.1 Thesis Organization

This thesis contains 6 chapters. The first chapter is a brief introduction to the components of AO systems and the motivations of this thesis.

Chapter two shows three modeling approaches of an AO system in the continuous domain. The conversion of these models to the discrete domain is shown. The result of this analysis is supported by experimental measurements of the response of the WFS output to changes to the computer output.

Chapter three shows the design of Type 1 and Type 2 controllers that could be used instead of a simple integrator. Generally, a Type 1 controller contains one integrator and a Type 2 controller contains two integrators. In this thesis, a controller that only consists of a single integrator is referred to as such, or as the CAO controller. Any further reference to a Type 1 controller is to the new controller developed in this thesis that consists of one integrator, two additional poles and one zero. The Type 1 controller has appropriate zero and pole placements that would improve the bandwidth without amplifying the noise. The Type 2 controller improves performance by providing prediction of the low frequency input signal, at the cost of amplification of system noise. This noise amplification was reduced by filtering, but remains present. These designs can be solved with the Sylvester matrix, but a more compact form is also provided specifically for the design of digital controllers.

Chapter four is devoted to the implementation of the controllers designed in chapter three. There were two important issues for the implementation. First was the selection of a 2D modal basis for the DM shapes. By defining which shapes are permitted on the DM, spatial aliasing can be reduced. A set of shapes were developed that are simple to implement and defined well on a square grid. Second was the inclusion of the

residual error due to output quantization into the implementation design to reduce the negative impact of quantization of the DM actuator signals. This technique reduces the impact of quantization noise on the closed loop system and allows the system to remain stable when the output signal is clipped.

Chapter five provides evidence gathered from the UVic AO test bench that the methods of chapters three and four are operational and functioning in a manner that is consistent with the modeled and simulated responses.

Chapter six gives the overall conclusions from this work and the proposed areas of future work for this system and laboratory.

1.2 Motivation

The motivation for the controller development carried out in this project can be summarized as follows. Current AO systems use a simple integrator for the control of the DM. They employ sophisticated adaptive methods to optimize the gain of the controller in order to find the optimal trade off between bandwidth and noise amplification. This integrator is often approached as a continuous integrator for the system model, even though it is implemented in a computer. This gives an imprecise model of the actual operation and could impair the optimization process. This gives two areas of possible improvement: (i) find a model that is a better match to the real system and (ii) find a controller that improves the bandwidth without the sacrifice of noise amplification. The motivation of controller development was further extended to the development of a predictive controller.

A secondary motivation was that the Zernike polynomials use polar coordinates [3] and the use of this set for the shapes on the DM causes spatial aliasing for high order

polynomials. This is because the DM uses a Cartesian grid, so the polar resolution is lacking for high order Zernike polynomials. This aliasing limits the number of shapes that the DM can produce. An area for improvement was the development of a polynomial set that provides more shapes before aliasing occurs.

A third motivation was that current AO systems amplify the output quantization noise. An implementation scheme was necessary that does not amplify this noise source. This method also provided a stable implementation of the predictive controller.

One aspect of an AO system that needs further development, but was not a topic of this thesis, is the implementation of an adaptive process for the new controllers. This process should optimize the balance between bandwidth and the input noise amplification depending on the observation conditions and thus achieve further improvement of the system.

1.3 The Wave Front

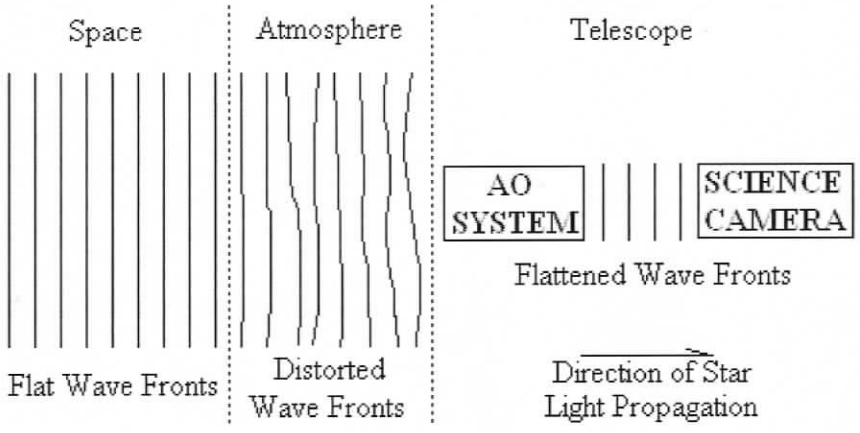

Figure 1.2: Transformations of the wave front from space to the science camera

Light has properties of waves and its shape can be defined by a wave front. The wave front from a point source expands radially. This is similar to how waves expand on the surface of a still pond when a small rock is dropped into it. Only instead of expanding as

a circle, light expands as a sphere. When the light has traveled a long distance, the radius of this sphere can be considered infinite. The surface of a sphere with infinite radius is flat.

Figure 1.2 shows the flat wave fronts arriving at the atmosphere from the source star. The wave fronts become distorted as they pass through the atmosphere to the telescope. The telescope captures a small portion of the light that reaches Earth and feeds it into the AO system. The light that leaves the AO system is ideally flat when it strikes the science camera.

The wave front distortion is caused by the effects of heat differences, wind speed and the non-uniform distribution of gases and materials in the atmosphere. The goal of an AO system is to make this distorted wave front as flat as possible. Then, the quality of ground based observations approaches that of satellite telescopes (e.g. Hubble), provided that the primary mirror in both have the same diameter. Ground based telescopes with AO can be used to obtain better observations than satellites because ground based telescopes can be far larger.

The light source used to measure the wave front is called a guide star. A laser is the reference light source that acts as the guide star in this experimental system. It is a 5mw red laser of wavelength 632.5nm. It generates a collimated beam that is 25 mm in diameter. This entire beam is passed through the TG. After the TG, lenses and the iris maintain the light beam diameter to less than 2.74 mm in order to properly illuminate the DM.

1.4 Wave Front Distortion

As mentioned in section 1.3, the atmosphere distorts the wave front. This distortion is caused by heat and wind. The effect of heat and wind on light can be observed simply by looking across a long stretch of pavement on a hot day. Objects in the distance look distorted and the distortion changes with time. The strength of the distortion is related to the temperature and the rate of change for the distortion is related to the wind speed. The TG, shown in Figure 1.3, is used on the UVic test bench to simulate atmospheric turbulence [2].

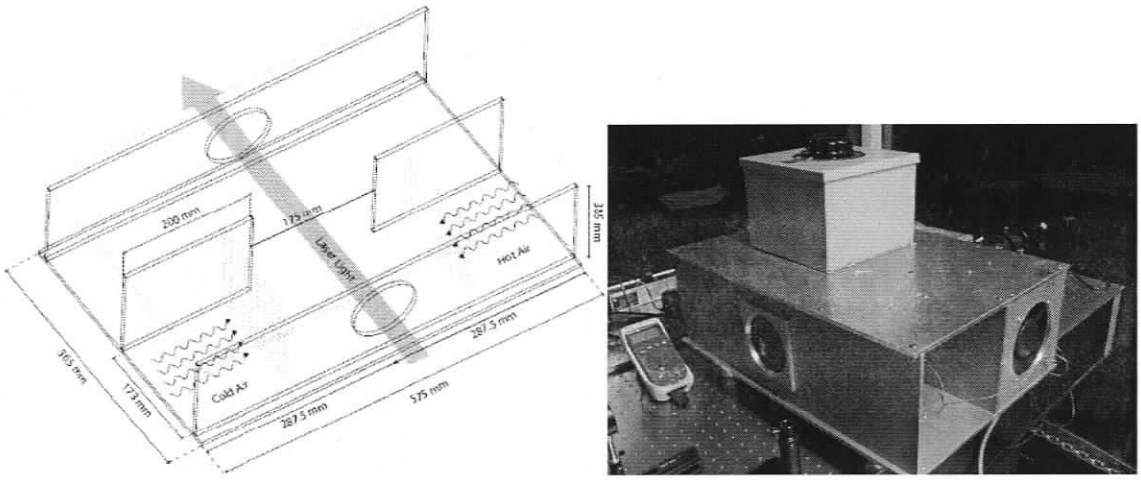

Figure 1.3: Turbulence generator diagram (left) and photograph (right)

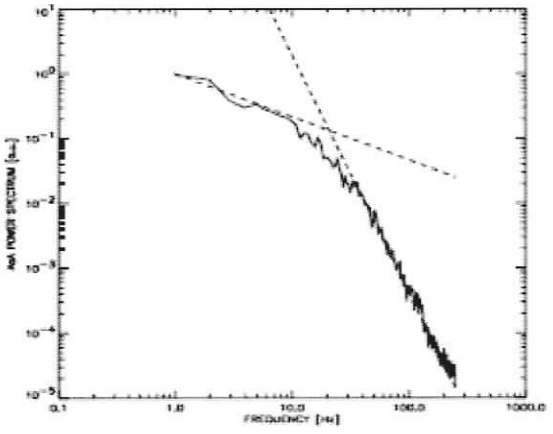

Figure 1.4: Kolmogoroff turbulence power spectrum
(arbitrary power scale)

Figure 1.4 shows generated turbulence that conforms to Kolmogoroff turbulence [2]. This means that the low frequency power is proportional to $f^{2/3}$ and the high frequency power is proportional to $f^{11/3}$. These are represented by the dashed line asymptotes. The knee frequency is the point that these two asymptotes intersect. The knee frequency for this particular experiment is shown as 20 Hz. However, real atmospheric turbulence has a knee frequency at approximately 1 Hz. The high frequency power drops at approximately 37 dB/decade, so the power above about 10 times the knee frequency becomes insignificant compared to the quantization noise for this system.

1.5 Wave Front Detection

The shape of a wave front can not be directly measured. However, the gradient of the wave front can be measured. A beam of light that is passed through a pinhole will continue along its angle of incidence. It was shown in 1899 by Hartmann [4] that placing a 2D array of pinholes in the path of a beam of light will cause each section of the beam to travel at its angle of incidence [5]. When the wave front is distorted, the angle of incidence is different for each sub-section. If a detector is placed after the pinholes, the angle can be measured. This angle is effectively the local gradient of the wave front. Because it is a gradient, the constant phase offset is lost.

It was shown by Shack and Platt that an array of lenslets could be used instead of an array of pinholes [5]. The light from each lenslet are brought to focal points and the displacements from each reference point relates to the local angle of incidence. This method is called the Shack-Hartmann Wave Front Sensor (WFS) and is the method used in the experimental set up at the UVic lab.

The UVic AO detector is a Dalsa CCD camera that can take up to 522 pictures per second. The pixels have 8-bit resolution. It uses an 11x11 lenslet array with a focal length of 8 mm.

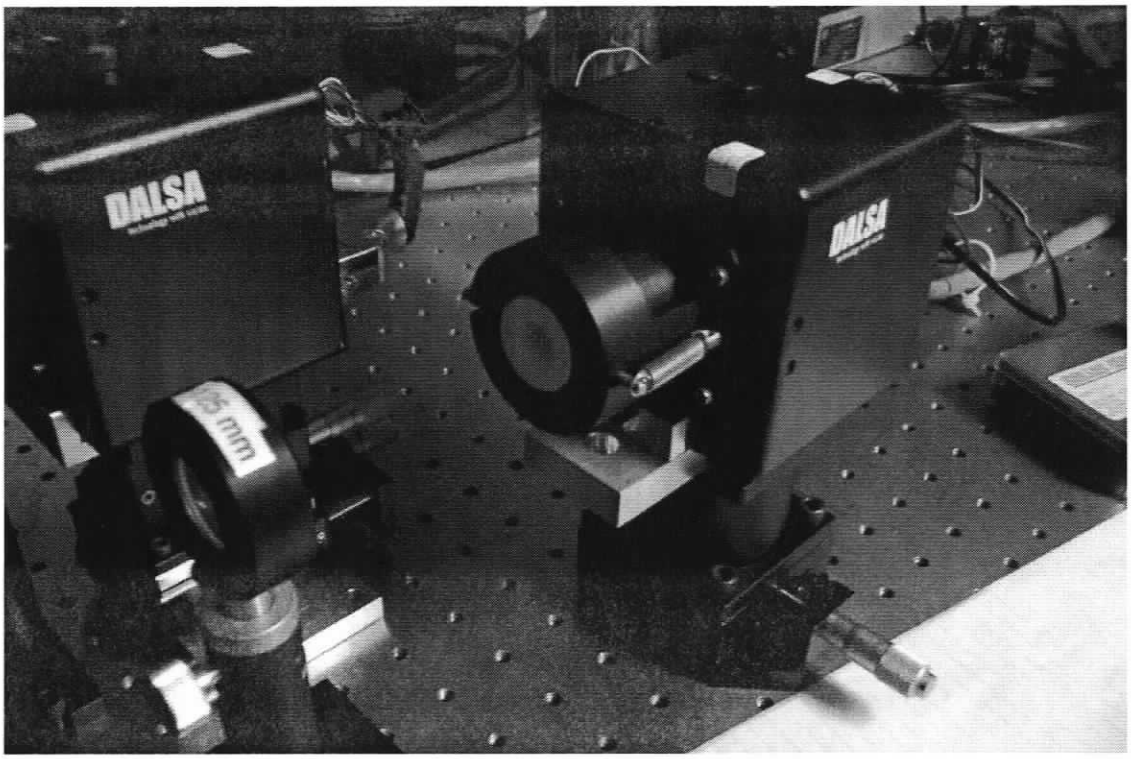

Figure 1.5: Wave front sensor photograph

1.6 Wave Front Correction

This system has two components that can be used to correct the wave front. The first component is the tip tilt mirror (TT). This is a flat mirror that can change its angle in two ideally orthogonal axes. This TT is used to steer the guide star beam to the reference position on the science camera. Its range is ±1 milliradian on both the x and y axis. Its dynamic response is a slew rate of 0.5 radians/second. At the current sampling rate of 261 samples/second the TT can move 1.92 milliradians in one sample. The current system was designed assuming the mirror will not be moving more than 1.92 milliradians in one sample.

The DM is used to correct for the higher order optical aberrations. It is a 12x12 grid of 140 actuators. There are only 140 actuators because each of the 4 corners does not have an actuator. This grid is 3.3mm by 3.3mm. Each actuator has a stroke of 1.2 μm. The upper electrode is attracted to the lower electrode by a voltage difference and is shown in Figure 1.7. The voltage applied to an actuator has a quadratic relationship to the actuator displacement. The inverse of this relationship is used to convert the desired displacement to an appropriate voltage before driving the DM so that the relationship between the controller signals and the actual displacement is linear.

The actuator grid is optically magnified so that it has the same spacing on the WFS as the spacing of the WFS sub-aperture grid. These grids are offset of each other so that each actuator is surrounded by 4 WFS spots and each WFS spot is surrounded by 4 actuators [6].

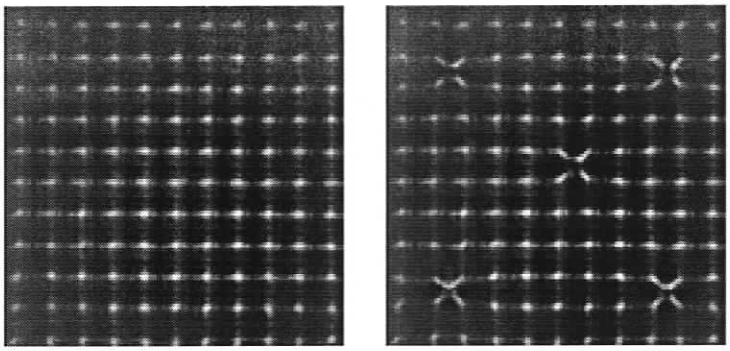

Figure 1.6: WFS measuring a flat DM (left) and 5 lowered actuators (right)

The goal of the controller is to make the centroid under each lenslet of the WFS maintain their respective reference point. If this is accomplished for all lenslets, it is equivalent to flattening the distorted wave front. When the wave front is flat, there is zero net distortion of the light between the source star and the science camera. A common controller for an AO system is an integrator implemented in a computer with an adjustable gain. This gain is tuned with an adaptive process that balances the error caused

by the controller's inability to perfectly follow the input against the error caused by the amplification of the system noise generated by the sensor and actuator signal quantization.

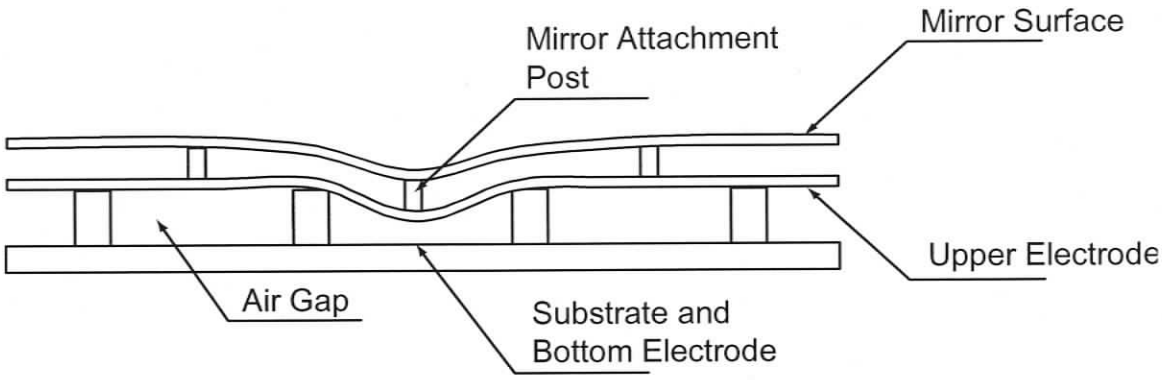

Figure 1.7: Deformable mirror diagram

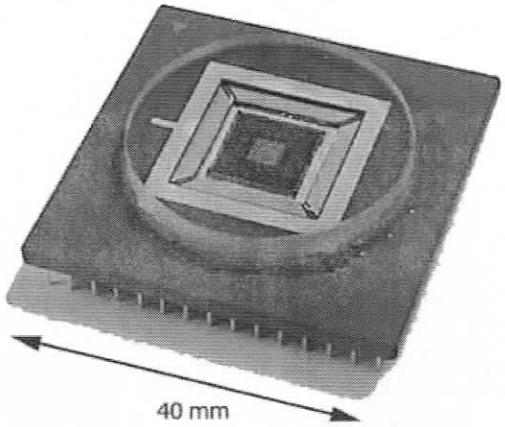

Figure 1.8: Boston Micromachines deformable mirror photograph

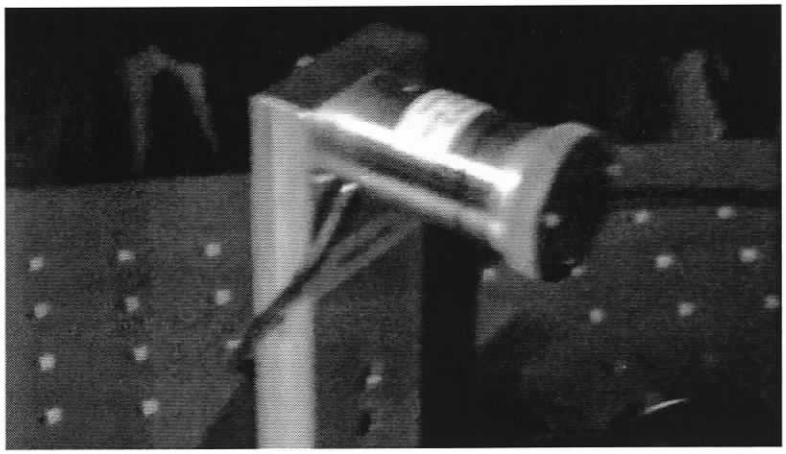

Figure 1.10: Tip tilt mirror photograph

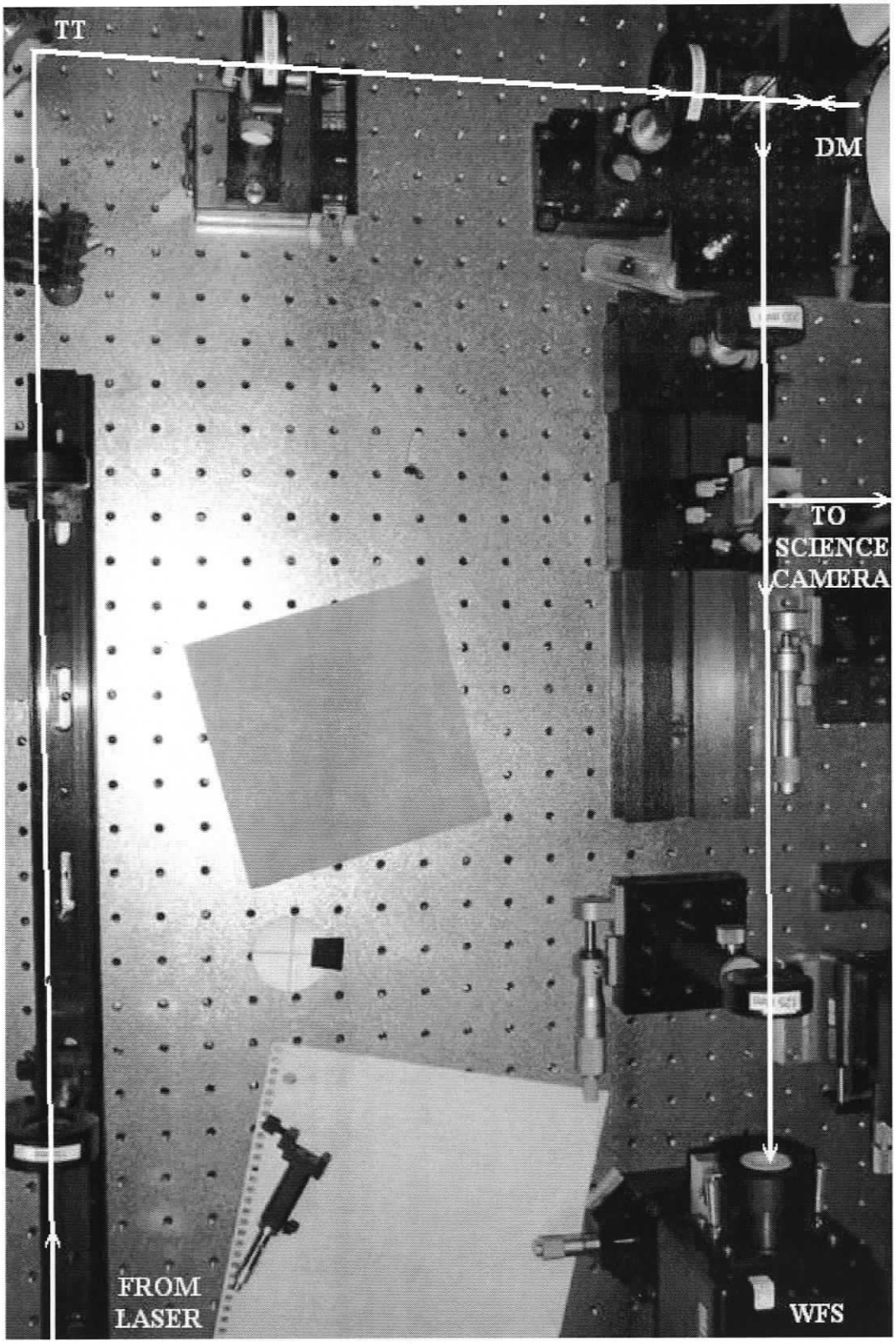

Figure 1.10: Photograph of the layout of TT, DM and WFS with primary beam path overlay

Chapter 2

Modeling

2.1 Classical Adaptive Optics Systems

2.1.1 Continuous System Model

The AO systems currently in use on telescopes have been designed using a continuous open loop system model. For example, the Altair AO system (mounted on the Gemini North Telescope) was designed using the open loop model of equation (2.1). There are four parts of the model that are shown respectively in equation (2.1) and can be found in [9]; (i) the camera was modeled as a zero-order hold, (ii) the time difference between the sample time and the camera integration time was modeled as a time shift of T_s-T_i seconds, (iii) all the other delays of the AO system were modeled as a time shift of τ seconds, and (iv) the controller itself was modeled as a continuous integrator with a variable gain, g.

$$G_{Altair}(s) = \left[\frac{1-\exp(-T_i s)}{T_i s}\right]\left[\exp(-(T_s - T_i)s)\right]\left[\exp(-\tau s)\right]\left[\frac{g}{T_s s}\right] \tag{2.1}$$

where $s = j2\pi f$

f is the frequency

T_s is the sample time

T_i is the integration time of the WFS CCD

τ is the delay of the AO loop

g is the gain

Normally the system has $T_s = T_i = \tau$. When this substitution is made (2.1) becomes (2.2). This will be referred to as the 'Classic Adaptive Optics' (CAO) continuous model.

$$G_{CAO}(s) = \left[\frac{1-\exp(-T_s s)}{T_s s}\right]\left[\exp(-T_s s)\right]\left[\frac{g}{T_s s}\right] \tag{2.2}$$

A similar approach was taken for the Very Large Telescope (VLT) Planet Finder project [10]. For this model, T_i, T_s and τ were already considered equal. The four stages of this model are; (i) the camera integration time, (ii) sample and hold stage, (iii) delay of transfer to computer and calculation and finally (iv) the model of the integrator for control as shown in equation (2.3).

$$G_{VLT}(s) = \left[\frac{1-\exp(-T_s s)}{T_s s}\right]\left[\frac{1-\exp(-T_s s)}{T_s s}\right]\left[\exp(-T_s s)\right]\left[\frac{g}{1-\exp(-T_s s)}\right] \tag{2.3}$$

This approach used an appropriate continuous model for the integrator implemented in a computer. However, cancellation reduces it to the CAO model in equation (2.2).

The closed loop output transfer function is found by inserting the open loop model into equation (2.4). This is used to understand how noise signals will be passed to the DM. Another important transfer function to consider is the error transfer function shown in equation (2.6). The amplitude response of this is referred to as the rejection ratio. It is used to show how well the system will follow an input signal. Together, these are used in current AO systems to balance the input following error with the noise error propagated to the DM.

$$T(s) = \frac{output(s)}{input(s)} = \frac{G(s)}{1+G(s)} \tag{2.4}$$

$$error(s) = input(s) - output(s) \tag{2.5}$$

$$E(s) = \frac{error(s)}{input(s)} = 1 - T(s) = \frac{1}{1+G(s)} \tag{2.6}$$

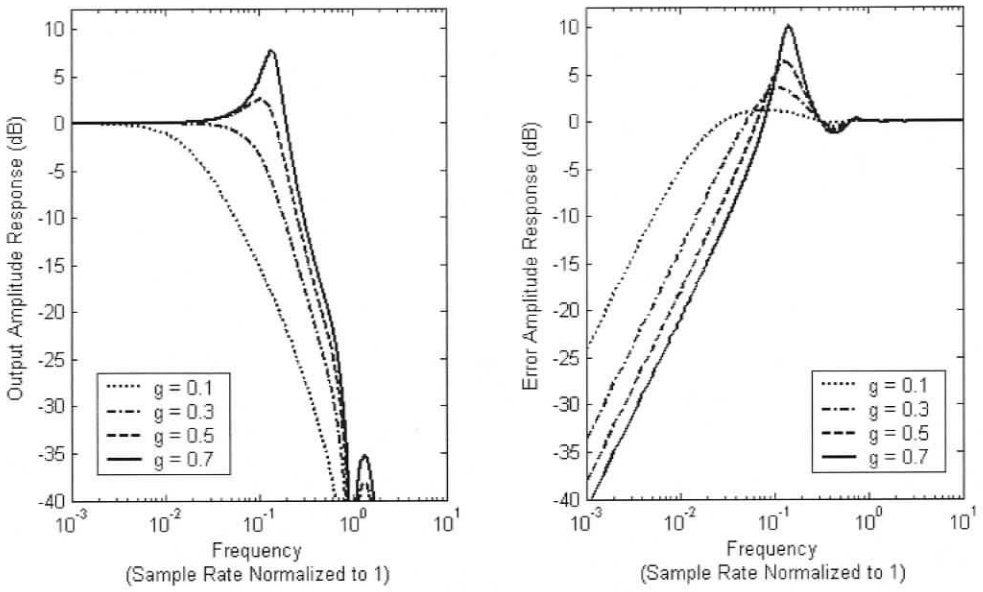

Figure 2.1: Amplitude response of the continuous output transfer function, equation (2.2) (left) and its rejection ratio (right) for various gain, g, and with $T_s = 1$

2.1.2 Discrete System Model

Since AO systems are controlled by a computer, a discrete system model should be developed for controller design. The portion of $G_{CAO}(s)$ external to the controller (response of DM and WFS) is considered to be $G_{Ext}(s)$ as in equation (2.7).

$$G_{Ext}(s) = \left[\frac{1-\exp(-T_s s)}{T_s s}\right]\left[\exp(-T_s s)\right] \tag{2.7}$$

To convert this continuous model to a discrete model, a sample and hold model must also be applied. This model converts impulses spaced by the sampling time into square pulses that have duration of the sampling time.

$$G_{SH}(s) = \left[\frac{1-\exp(-T_s s)}{s}\right] \tag{2.8}$$

The Z transform [11] is used to convert the product of equations (2.7) and (2.8) into the discrete model of equation (2.11) as follows.

$$G_{Ext}(z) = Z\{G_{Ext}(s)G_{SH}(s)\}$$
$$= Z\left\{\left[\frac{1-\exp(-T_s s)}{T_s s}\right]\left[\exp(-T_s s)\right]\left[\frac{1-\exp(-T_s s)}{s}\right]\right\} \quad (2.9)$$

$$G_{Ext}(z) = z^{-1}\left(1-z^{-1}\right)^2 Z\left\{\frac{1}{T_s s^2}\right\} \quad (2.10)$$

$$G_{Ext}(z) = z^{-1}\left(1-z^{-1}\right)^2 \frac{T_s z^{-1}}{T_s\left(1-z^{-1}\right)^2} = z^{-2} \quad (2.11)$$

The discrete model found by converting the CAO model to a discrete model is simply 2 delays. A simple integrator control model will have the open loop transfer function shown in equation (2.12).

$$G_{CAO}(z) = \frac{gz^{-2}}{1-z^{-1}} \quad (2.12)$$

A formula for the output amplitude response of the CAO system can be found by finding the absolute value of the output transfer function. The CAO discrete output transfer function is shown as equation (2.13) and the discrete output amplitude response is shown as equation (2.16).

$$T_{CAO}(z) = \frac{G_{CAO}(z)}{1+G_{CAO}(z)} = \frac{gz^{-2}}{1-z^{-1}+gz^{-2}} \quad (2.13)$$

$$\left|T_{CAO}(z)\right| = \sqrt{\left(\frac{gz^{-2}}{1-z^{-1}+gz^{-2}}\right)\left(\frac{gz^{2}}{1-z^{1}+gz^{2}}\right)} \quad (2.14)$$

$$\left|T_{CAO}(z)\right| = \frac{g}{\sqrt{2+g^2-(g+1)\left(z^1+z^{-1}\right)+g\left(z^2+z^{-2}\right)}} \quad (2.15)$$

$$\left|T_{CAO}(f)\right| = \frac{g}{\sqrt{2+g^2-2(g+1)\cos\left(2\pi\frac{f}{f_s}\right)+2g\cos\left(4\pi\frac{f}{f_s}\right)}} \quad (2.16)$$

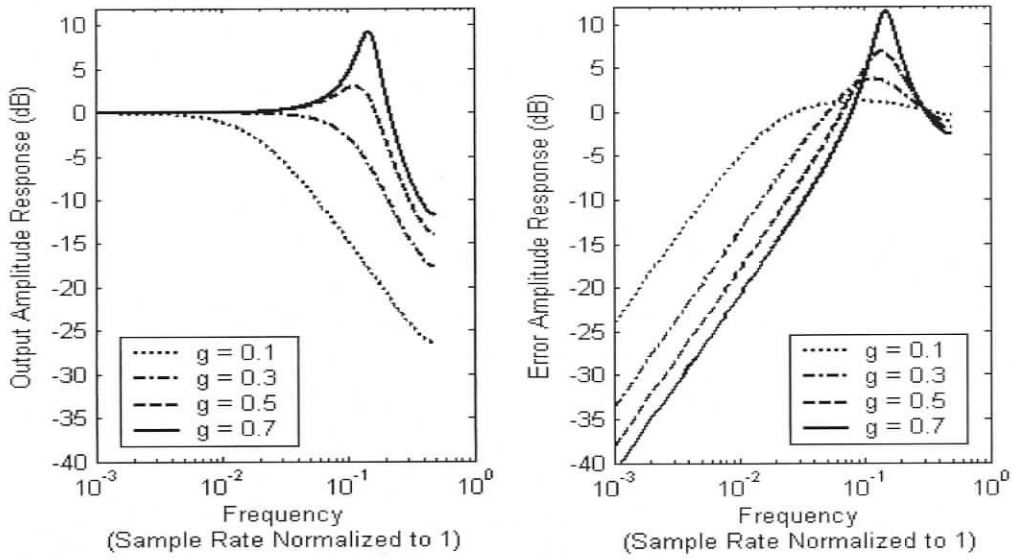

Figure 2.2: Amplitude response of the discrete output transfer function (left) and its rejection ratio (right) for various gain

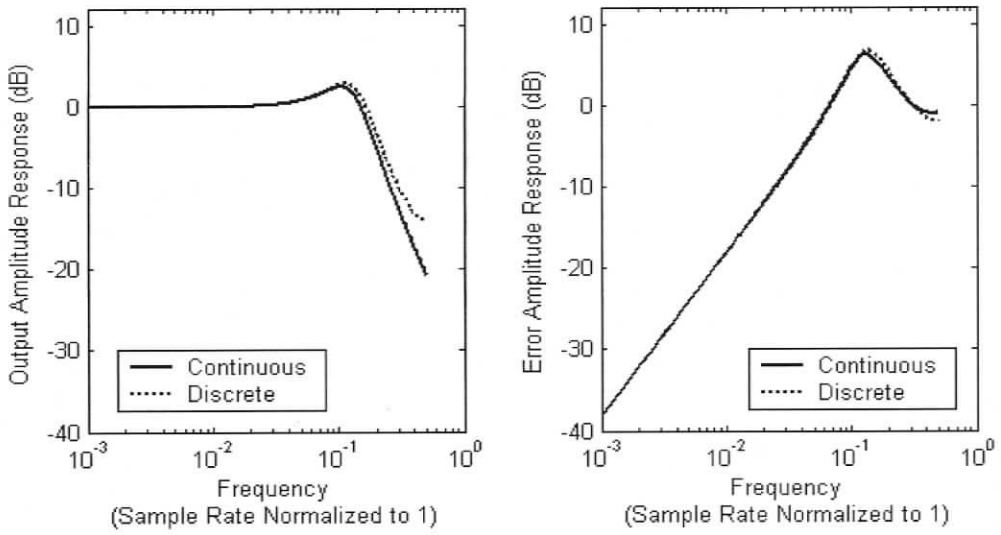

Figure 2.3: Comparison of the CAO discrete and continuous output transfer functions (left) and the respective rejection ratios (right) for a gain of 0.5

A hybrid approach is used for the AO system of Keck [12]. It uses a similar model of the dynamics of the WFS as the VLT-Planet Finder in equation (2.3), but models the controller in the Z domain. This system uses the CAO controller for its tip tilt mirror.

The discrete model is a better representation of the true system because it incorporates sampling. The plots in Figure 2.2 are indistinguishable to those of Figure 2.1 when the frequency is below 10% of the sampling rate, so either model can be useful for this range. However, when the frequency exceeds 10% of the sampling rate, the continuous output transfer function shows more suppression of high frequency signals than the discrete model. This is because the continuous model does not include the effects of sampling and aliasing. A comparison of the two models is shown in Figure 2.3 for a gain of 0.5 to illustrate this. Figure 2.4 shows the ratio of the discrete output amplitude response to the continuous output amplitude response at a gain of 0.5. This ratio is naturally equal to 1 where they are equivalent models. Therefore, this shows that the high frequency system noise is being amplified more than the continuous model suggests.

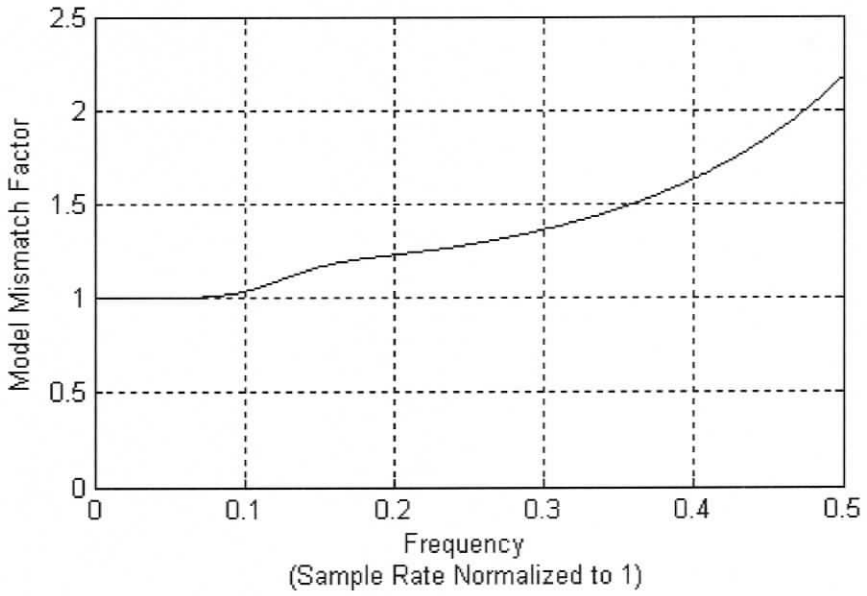

Figure 2.4: Ratio of the discrete and continuous output transfer functions

2.2 Modeling of the Optical Path

The previous section showed that existing AO systems have continuous models that translate into two delays as a discrete model. This section shows through experimentation that the AO system at UVic also follows this model.

The open loop transfer function of the optical path was determined by measurement of the input sensor response to random actuator output (as originally reported in [7]). For this experiment, an open loop controller actuated random magnitudes of a radial parabolic shape on the DM and the WFS was tuned to detect that shape. This allowed the test to be done using 1D signals even though the DM and sensor are 2D grids.

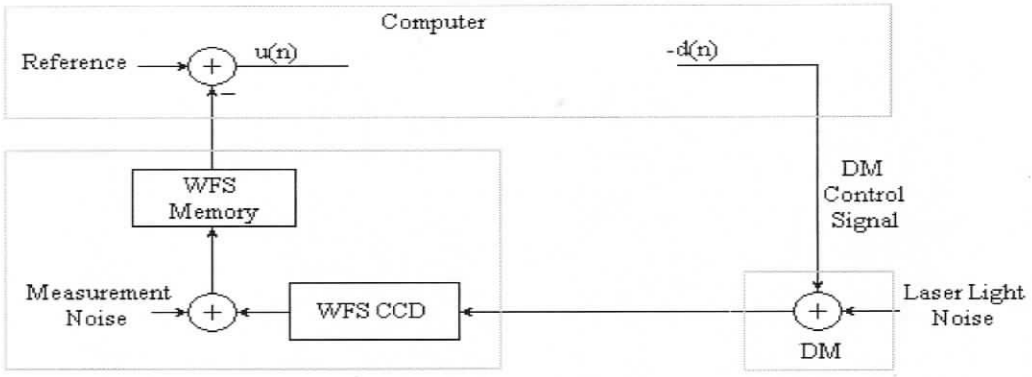

Figure 2.5: Optical feedback path

The actual measurement of the parabola on sample n, $u(n)$, was recorded for its respective random output signal, $-d(n)$. The desired measurement, $d(n)$, is the negative of the output signal because of the negative feedback path. The sample number, n, has a range of 0 to 1999 for this experiment. This information was used in the Wiener-Hopf equations [8] to determine the Wiener filter that could be applied after $u(n)$ to make the feedback path act like a negative unit feedback path with no dynamics. This approach uses the cross-correlations of the actual measurements and the desired measurements to

determine the response of the intervening channel. In this case the channel is the DM, optics, WFS and the electronics.

$$p(-k) = E[u(n-k)d(n)] \tag{2.17}$$

$$\begin{bmatrix} p(0) & p(1) & p(2) & p(3) & p(4) \end{bmatrix} = \begin{bmatrix} 0.0007 & -0.0002 & 0.2243 & 0.0125 & 0.0011 \end{bmatrix} \tag{2.18}$$

where $E[\ ]$ is the expected value operator

u is the actual measurements after the mean value is set to 0

d is the desired measurements and has 0 mean and 0.25 variance

n is the sample number and k is the sample offset

p is the cross-correlation vector of the desired and measured values

The cross-correlation vector, $p(-k)$, is the cross-correlation of the actual measurement, $u(n-k)$, and the desired measurement, $d(n)$. When k is negative, as in the results in equation (2.18), it means that the cross-correlation is between the current desired measurement and the actual measurement $|k|$ samples in the future. It is expected that $p(0)$ is insignificant because the measurement is made before the output is changed, so there can be no correlation. Therefore, since $p(1)$ has the same order of magnitude as $p(0)$, that measurement also does not contain any correlation with the desired signal. The largest cross-correlations are for

$$p(2) = E[u(n+2)d(n)] = E[u(n)d(n-2)] = 0.2243 \tag{2.19}$$

$$p(3) = E[u(n+3)d(n)] = E[u(n+1)d(n-2)] = 0.0125 \tag{2.20}$$

Note that $E[d(n)d(n)]$ (I.e. the variance of $d(n)$) is 0.25, so $u(n+2)$ is probably very close to the value of $d(n)$. The cross-correlations after $p(3)$ are on the same order of magnitude of $p(0)$, so are deemed insignificant. These results mean that there are two

delays before the input of the optical system can affect the output of the optical system. If $p(3)$ is significant, it suggests that there may be a single pole in this channel. The location of this pole will now be determined.

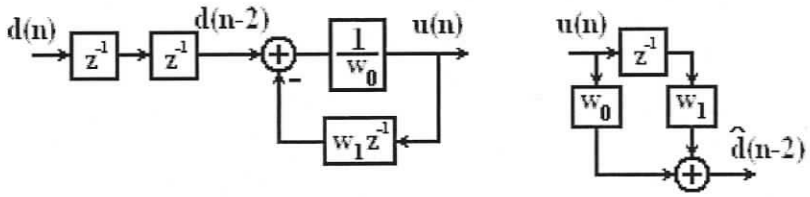

Figure 2.6: Model of the optical path dynamics (left) and the respective Wiener filter (right)

The Wiener-Hopf equation uses p along with the auto-correlation matrix, R, to determine the appropriate Wiener filter. Such filters are used to cancel the dynamics of the channel so that the output of the filter is an estimate of the desired measurement (see Figure 2.6). However, the only way to cancel a delay is through prediction. It is not desirable to have a predictor at this stage, so $d(n\text{-}2)$ will be considered the desired measurement on sample n, rather than $d(n)$. Since there is this added delay, the Wiener filter will now be derived for this particular system, rather than use assumptions on how the standard formulation of the Wiener-Hopf equation would be modified. For real numbers,

$$r(k) = E[u(n-k)u(n)] = E[u(n+k)u(n)] \tag{2.21}$$

$$R = E[uu^T] = \begin{bmatrix} r(0) & r(1) & r(2) & \cdots \\ r(1) & r(0) & r(1) & \ddots \\ r(2) & r(1) & r(0) & \ddots \\ \vdots & \ddots & \ddots & \ddots \end{bmatrix} \tag{2.22}$$

where R is the auto-correlation matrix of the measured values, u

Since there are only two values of p that are significant, only a 2x2 subsection of the R matrix is used.

$$R_{2,2} = \begin{bmatrix} r(0) & r(1) \\ r(1) & r(0) \end{bmatrix} = \begin{bmatrix} 0.2042 & 0.0120 \\ 0.0120 & 0.2042 \end{bmatrix} \tag{2.23}$$

Equation (2.24) is developed directly from Figure 2.6 (left). Then, $u(n\text{-}k)$ is multiplied by all the terms and the expected value operator is also applied in equation (2.25). Evaluating equation (2.25) at $k = 0$ and $k = 1$ gives equations (2.26) and (2.27) respectively. These equations are combined into a matrix form as shown in equation (2.28). Equation (2.29) is similar to the Wiener-Hopf equation [8]. The only difference is that in this case $p(-k+2)$ is used rather than $p(-k)$ to account for the 2 delays of the system. Equation (2.30) is the evaluation of equation (2.29) with data gathered from this experiment.

$$w_0 u(n) = d(n-2) - w_1 u(n-1) \tag{2.24}$$

$$E\left[w_0 u(n-k)u(n)\right] = E\left[u(n-k)d(n-2) - w_1 u(n-k)u(n-1)\right] \tag{2.25}$$

$$w_0 r(0) = p(2) - w_1 r(1) \tag{2.26}$$

$$w_0 r(1) = p(1) - w_1 r(0) \tag{2.27}$$

$$\begin{bmatrix} r(0) & r(1) \\ r(1) & r(0) \end{bmatrix} \begin{bmatrix} w_0 \\ w_1 \end{bmatrix} = \begin{bmatrix} p(2) \\ p(1) \end{bmatrix} \tag{2.28}$$

$$\begin{bmatrix} w_0 \\ w_1 \end{bmatrix} = R_{2,2}^{-1} \begin{bmatrix} p(2) \\ p(1) \end{bmatrix} \tag{2.29}$$

$$\begin{bmatrix} w_0 \\ w_1 \end{bmatrix} = \begin{bmatrix} 0.2042 & 0.0120 \\ 0.0120 & 0.2042 \end{bmatrix}^{-1} \begin{bmatrix} 0.2243 \\ -0.0002 \end{bmatrix} = \begin{bmatrix} 1.1023 \\ -0.0658 \end{bmatrix} \tag{2.30}$$

where w_0 and w_1 are the tap weights of the Wiener filter

The value of w_1 is very small and the corresponding zero location of this Wiener filter is at $z = 0.06$. This corresponds to a pole at $z = 0.06$ for the optical path, which has a

very fast response. As shown in later chapters, the model matched the actual system quite well without the inclusion of a Wiener filter. Therefore, a Wiener filter was found to be unnecessary and the model of the open loop optical system (excluding the controller) is z^{-2}, which is a very close approximation to current AO systems.

2.3 Conclusions

The optical feed back loop is modeled as a discrete system that has two sample delays. There are no significant dynamic effects found other than this delay. If this system was controlled by a simple integrator with variable gain, the open loop transfer function would be equation (2.12)

The models for Altair, Keck and the simulated VLT-Planet Finder have similar modeling approaches. The conversion of these CAO continuous models to discrete models also shows an optical feed back model of two sample delays. All three of these continuous open loop models reduce to the same discrete model of equation (2.12). This shows that other AO systems have similar dynamics to the AO system at the University of Victoria. Therefore, it is expected that the progress shown within this thesis can be applied to any AO system that has the CAO model.

Operational AO systems often have an optimizer for the gain. These optimizers use the model of the output transfer function and its rejection ratio to determine what gain would give the smallest error. The continuous model does not match the real system beyond 10% of the sampling rate due to the effects of aliasing and sampling. So the estimation of error due to high frequency noise will be optimistic when using a continuous model. Therefore, the discrete output amplitude response of equation (2.16) could be used for improved gain optimization on CAO systems.

Chapter 3

Digital Controller Design

A common approach in controller design is to create an arbitrary transfer function, $G_A(z)$, that when combined with the system transfer function, $G_S(z)$, forms an open loop transfer function that has the desired closed loop properties. The pole placement method in this chapter is based on a method of arbitrarily solving for the denominator of equation (3.3).

System Transfer Function

$$G_S(z) = \frac{B(z)}{A(z)} \tag{3.1}$$

Controller Transfer Function

$$G_A(z) = \frac{\beta(z)}{\alpha(z)} \tag{3.2}$$

Closed Loop Transfer Function

$$T_T(z) = \frac{C(z)}{R(z)} = \frac{G_A(z)G_S(z)}{1+G_A(z)G_S(z)} = \frac{B(z)\beta(z)}{A(z)\alpha(z)+B(z)\beta(z)} \tag{3.3}$$

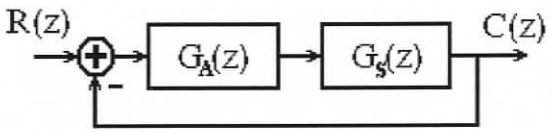

Figure 3.1: Simple closed loop control system

A polynomial solution of the pole placement problem can be found with the use of the Sylvester matrix. This method is shown in section 3.1. However, the Sylvester matrix approach solves for arbitrary polynomials and does not take into account some fixed properties of controller transfer functions. A reduced method is shown in section 3.2. Section 3.3 shows how to use the polynomial approach given fixed parameters in the designed controller. This is followed in subsequent sections by design examples.

3.1 Sylvester Matrix

The problem of pole placement for a closed loop control system can be solved using a polynomial approach called the Sylvester matrix as given by Ogata [11]. In this approach, the denominator of equation (3.3) is set to a desired polynomial, $D(z)$. If the system to be controlled is given by (3.1), then the controller given by (3.2) can be determined by the Diophantine equation (3.4).

$$\alpha(z)A(z) + \beta(z)B(z) = D(z) \tag{3.4}$$

where $A(z) = a_0 z^n + a_1 z^{n-1} + \cdots + a_{n-1} z + a_n$

$B(z) = b_0 z^n + b_1 z^{n-1} + \cdots + b_{n-1} z + b_n$

$\alpha(z) = \alpha_0 z^{n-1} + \alpha_1 z^{n-2} + \cdots + \alpha_{n-2} z + \alpha_{n-1}$

$\beta(z) = \beta_0 z^{n-1} + \beta_1 z^{n-2} + \cdots + \beta_{n-2} z + \beta_{n-1}$

$D(z) = d_0 z^{2n-1} + d_1 z^{2n-2} + \cdots + d_{2n-2} z + d_{2n-1}$

n is positive integer

The values of α(z) and β(z) can be determined with the Sylvester matrix. An example Sylvester matrix form assuming $n = 3$ is given as equation (3.5). This matrix is size $2n$x$2n$.

$$\left[\begin{array}{ccc|ccc} a_3 & 0 & 0 & b_3 & 0 & 0 \\ a_2 & a_3 & 0 & b_2 & b_3 & 0 \\ a_1 & a_2 & a_3 & b_1 & b_2 & b_3 \\ \hline a_0 & a_1 & a_2 & b_0 & b_1 & b_2 \\ 0 & a_0 & a_1 & 0 & b_0 & b_1 \\ 0 & 0 & a_0 & 0 & 0 & b_0 \end{array}\right] \left[\begin{array}{c} \alpha_2 \\ \alpha_1 \\ \alpha_0 \\ \hline \beta_2 \\ \beta_1 \\ \beta_0 \end{array}\right] = \left[\begin{array}{c} d_5 \\ d_4 \\ d_3 \\ d_2 \\ d_1 \\ d_0 \end{array}\right] \tag{3.5}$$

This is a very good method for solving the general Diophantine equation. However, this general solution does not take advantage of the digital controller form.

This method also represents the polynomials in non-causal form, therefore is not directly realizable.

3.2 Reduced Sylvester Matrix

The Diophantine equation (3.4) can be redefined with some understanding of the fixed values of some of the coefficients. The requirement for arbitrary pole placement is that $\alpha(z)$ and $\beta(z)$ must provide enough variables to allow the roots of $D(z)$ to be chosen arbitrarily. This is a relaxed requirement compared to defining $D(z)$ arbitrarily as in the previous method. Therefore, $D(z)$ can be normalized so that d_0 is always known to be 1. Also, the standard form for transfer functions is that a_0 and α_0 are also normalized to be 1. Further, for the system to be realizable, there must be a minimum of one sample delay in $\beta(z)B(z)$. This is a fixed system requirement, therefore, b_0 will always be considered to be 0.

The Diophantine equation is now redefined as equation (3.6). Another change compared to the Sylvester matrix is that the equations are represented in a causal form.

$$\alpha(z)A(z) + \beta(z)B(z) = D(z) \tag{3.6}$$

where $A(z) = 1 + a_1 z^{-1} + \cdots + a_{n-1} z^{-(n-1)} + a_n z^{-n}$

$$B(z) = b_1 z^{-1} + b_2 z^{-2} + \cdots + b_{m-1} z^{-(m-1)} + b_m z^{-m}$$

$$\alpha(z) = 1 + \alpha_1 z^{-1} + \cdots + \alpha_{m-2} z^{-(m-2)} + \alpha_{m-1} z^{-(m-1)}$$

$$\beta(z) = \beta_0 + \beta_1 z^{-1} + \cdots + \beta_{n-2} z^{-(n-2)} + \beta_{n-1} z^{-(n-1)}$$

$$D(z) = 1 + d_1 z^{-1} + \cdots + d_{n+m-2} z^{-(n+m-2)} + d_{n+m-1} z^{-(n+m-1)}$$

n and m are both non-negative integers

This means that for n fixed open loop system poles, this method will find $n-1$ arbitrary zeros. Likewise, this method will find $m-1$ open loop controller poles for m terms of $B(z)$. The matrix form in (3.7) takes advantage of the specific form of controllers. Further, it is ordered in a manner that is simpler to implement in programs such as MatLab, since the coefficients are ordered in ascending order. The resulting matrix is size $(n+m-1)\text{x}(n+m-1)$.

$$\left[\begin{array}{ccc|cccc} 1 & 0 & 0 & b_1 & 0 & 0 & 0 \\ a_1 & \ddots & 0 & b_2 & \ddots & 0 & 0 \\ a_2 & \ddots & 1 & \vdots & \ddots & \ddots & 0 \\ \vdots & \ddots & a_1 & b_m & \ddots & \ddots & b_1 \\ a_n & \ddots & a_2 & 0 & \ddots & \ddots & b_2 \\ 0 & \ddots & \vdots & 0 & 0 & \ddots & \vdots \\ 0 & 0 & a_n & 0 & 0 & 0 & b_m \end{array}\right] \left[\begin{array}{c} \alpha_1 \\ \vdots \\ \alpha_{m-1} \\ \hline \beta_0 \\ \beta_1 \\ \vdots \\ \beta_{n-1} \end{array}\right] = \left[\begin{array}{c} d_1 \\ d_2 \\ \vdots \\ \vdots \\ \vdots \\ d_{n+m-2} \\ d_{n+m-1} \end{array}\right] - \left[\begin{array}{c} a_1 \\ a_2 \\ \vdots \\ a_n \\ 0 \\ \vdots \\ 0 \end{array}\right] \tag{3.7}$$

since $d_0 = 1$, $a_0 = 1$, $\alpha_0 = 1$ and $b_0 = 0$

If it is desirable to make the inversion of this matrix require fewer computations, it can be decomposed as an LU decomposition [13]. This creates a lower triangular matrix and an upper triangular matrix that when multiplied together produce the original matrix. The above matrix is set up so that the first m-1 columns are already in lower triangular form. The corresponding upper triangular subsection would be the m-1 columns of the identity matrix. This leaves only n columns that require decomposition.

$D(z)$ is the designed closed loop polynomial for the poles of the system when the gain, g, is 1. It is common to allow adjustments to g in an implemented controller for tuning or optimization purposes. In this case the controller would be given by (3.8) and the closed loop transfer function would be (3.9). Adding $(g\text{-}1)\beta(z)B(z)$ to both sides of (3.6) gives (3.10). This shows how different gain values will affect the closed loop poles.

$$G_A(z) = g\frac{\beta(z)}{\alpha(z)} \tag{3.8}$$

$$T_T(z,g) = \frac{g\beta(z)B(z)}{\alpha(z)A(z) + g\beta(z)B(z)} \tag{3.9}$$

$$\alpha(z)A(z) + g\beta(z)B(z) = D(z) + (g-1)\beta(z)B(z) \tag{3.10}$$

Using the transfer function of equation (3.9) could be useful for minor tweaking of the implemented system. However, if the designer knows a specific path for the closed loop poles in the Z-plane, then the coefficients of $D(z)$ can be formed as functions of variables instead of fixed coefficients.

3.3 Fixed Controller Properties

The method of section 3.2 solves for the zeros and poles of the controller that are allowed to be variables. Now the case of fixed controller dynamics is considered. The controller designer may wish to filter specific frequencies or choose a certain amount of integrators. These decisions must be made part of $G_S(z)$ for the purposes of obtaining $G_A(z)$. The dynamics of the fixed portion of the controller, $G_F(z)$, is multiplied with those of the plant, $G_P(z)$, to give $G_S(z)$. When it is time to implement the final controller, $G_C(z)$, it will be $G_A(z)G_F(z)$. This is shown in Figure 3.2.

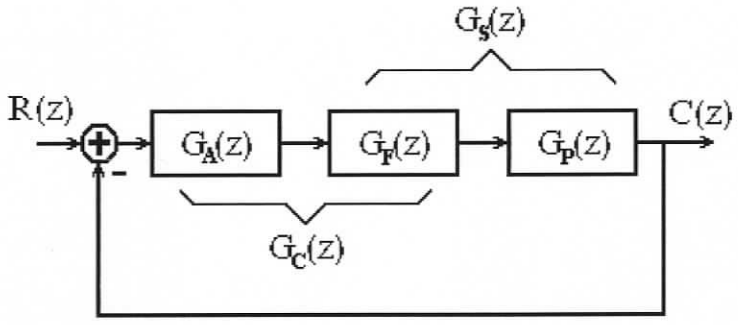

Figure 3.2: Closed loop system with fixed controller properties

For example, a plant that consists of only 2 delays is to be controlled by an integrator plus an additional unknown pole for the pole placement process. This plant is the model representing an adaptive optics system.

$$G_P(z) = z^{-2} \tag{3.11}$$

$$G_F(z) = \frac{1}{1 - z^{-1}} \tag{3.12}$$

$$G_S(z) = G_F(z)G_P(z) = \frac{z^{-2}}{1 - z^{-1}} = \frac{B(z)}{A(z)} \tag{3.13}$$

Equation (3.13) must always be normalized to have a_o = 1. Since the plant is highly responsive, it is desired to put the closed loop poles at z = 0 for maximum steady state settling speed. This is defined in equation (3.14).

$$D(z) = 1 \tag{3.14}$$

In this design example, m = 2 and n = 1 which means the solution will be found with the matrix shown in (3.15).

$$\begin{bmatrix} \alpha_1 \\ \beta_0 \end{bmatrix} = \begin{bmatrix} a_0 & b_1 \\ a_1 & b_2 \end{bmatrix}^{-1} \left\{ \begin{bmatrix} d_1 \\ d_2 \end{bmatrix} - \begin{bmatrix} a_1 \\ a_2 \end{bmatrix} \right\} \tag{3.15}$$

Substituting the values for this specific problem gives (3.16)

$$\begin{bmatrix} \alpha_1 \\ \beta_0 \end{bmatrix} = \begin{bmatrix} 1 & 0 \\ -1 & 1 \end{bmatrix}^{-1} \left\{ \begin{bmatrix} 0 \\ 0 \end{bmatrix} - \begin{bmatrix} -1 \\ 0 \end{bmatrix} \right\} = \begin{bmatrix} 1 \\ 1 \end{bmatrix} \tag{3.16}$$

This shows that to control this system with an integrator (pole at z = 1), another controller pole needs to be placed at z = -1 with a gain of 1 in order to place the closed loop poles at z = 0. The controller given in equation (3.17) is the result of the controller designed in (3.16) multiplied by the fixed controller dynamics.

$$G_C(z) = G_A(z)G_F(z) = \frac{\beta_0}{\left(1+\alpha_1 z^{-1}\right)\left(1-z^{-1}\right)} = \frac{1}{1-z^{-2}} \tag{3.17}$$

The critically damped closed loop system, $T_C(z)$, is represented by equation (3.18). This system has the same dynamics as the plant system of equation (3.11).

$$T_C(z) = \frac{G_C(z)G_P(z)}{1+G_C(z)G_P(z)} = \frac{\dfrac{1}{1-z^{-2}}z^{-2}}{1+\dfrac{1}{1-z^{-2}}z^{-2}} = \frac{z^{-2}}{1} \tag{3.18}$$

If it is desirable to have an adjustable gain, equation (3.18) can be rewritten as (3.19). This system is stable when g is between 0 and 2.

$$G_T(z) = \frac{gG_C(z)G_P(z)}{1+gG_C(z)G_P(z)} = \frac{\dfrac{1}{1-z^{-2}}gz^{-2}}{1+\dfrac{1}{1-z^{-2}}gz^{-2}} = \frac{gz^{-2}}{1+(g-1)z^{-2}} \tag{3.19}$$

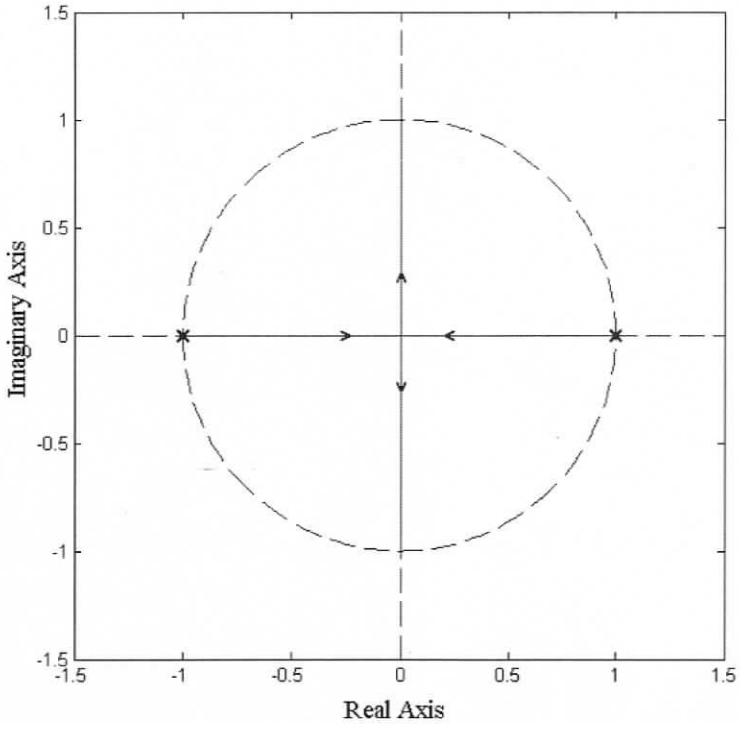

Figure 3.3: Root locus of closed loop system in the Z-plane

The closed loop system given in equation (3.19) unfortunately suffers from oscillations in practice. This is because the simple open loop pole at z = -1 corresponds to a complex pole in the continuous domain. An example of this effect is when g = 1, the odd sample signals are completely decoupled from the even sample signals because the closed loop system is z^{-2}. There is no means of forcing the even and odd samples to the same value. The system easily retains all noise at half the sampling rate. In order to reduce this effect, the output signal will be filtered.

3.4 Type 1 Controller Design

One design possibility is to use a simple two sample averaging filter. This places a zero at z = -1 which attenuates the filter magnitude to 0 at the Nyquist frequency. The plant remains the same as that in equation (3.11) and Figure 3.2, but the fixed controller properties are changed to include the filter.

$$G_F(z) = \frac{0.5 + 0.5z^{-1}}{1 - z^{-1}} \tag{3.20}$$

$$G_S(z) = G_F(z)G_P(z) = \frac{0.5z^{-2} + 0.5z^{-3}}{1 - z^{-1}} = \frac{B(z)}{A(z)} \tag{3.21}$$

The desired D(z) is still 1 as in equation (3.14). The solution is found in equation (3.22).

$$\begin{bmatrix} \alpha_1 \\ \alpha_2 \\ \beta_0 \end{bmatrix} = \begin{bmatrix} 1 & 0 & 0 \\ -1 & 1 & 0.5 \\ 0 & -1 & 0.5 \end{bmatrix}^{-1} \left\{ \begin{bmatrix} 0 \\ 0 \\ 0 \end{bmatrix} - \begin{bmatrix} -1 \\ 0 \\ 0 \end{bmatrix} \right\} = \begin{bmatrix} 1 \\ 1 \\ 0.5 \end{bmatrix} \tag{3.22}$$

$$G_A(z) = \frac{\beta_0}{1 + \alpha_1 z^{-1} + \alpha_2 z^{-2}} = \frac{1}{1 + z^{-1} + 0.5z^{-2}} \tag{3.23}$$

$$\begin{aligned} G_C(z) &= G_A(z)G_F(z) \\ &= \left(\frac{1}{1 + z^{-1} + 0.5z^{-2}} \right) \left(\frac{0.5 + 0.5z^{-1}}{1 - z^{-1}} \right) = \frac{0.5 + 0.5z^{-1}}{1 - 0.5z^{-2} - 0.5z^{-3}} \end{aligned} \tag{3.24}$$

If the controller is implemented with variable gain, the closed loop form is shown below.

$$T_{T1}(z,g) = \frac{gG_C(z)G_P(z)}{1+gG_C(z)G_P(z)}$$
$$= \frac{g\dfrac{0.5+0.5z^{-1}}{1-0.5z^{-2}-0.5z^{-3}}z^{-2}}{1+g\dfrac{0.5+0.5z^{-1}}{1-0.5z^{-2}-0.5z^{-3}}z^{-2}} = \frac{g(0.5z^{-2}+0.5z^{-3})}{1+(g-1)(0.5z^{-2}+0.5z^{-3})} \quad (3.25)$$

The analysis of the performance of this controller in the frequency and time domains is carried out in section 3.6.

3.5 Type 2 Controller Design

A Type 2 system will be designed here with this pole placement method. Since it is a Type 2 system, it requires two integrators. The benefit of having a Type 2 system is that it has 0 following error of a ramp input. Since the controlled system is a two sample delay, this results in a two sample prediction of the input when the frequencies are low.

The intended use of this controller is in astronomical adaptive optics where the input signal is related to the turbulence of the atmosphere. The power of the turbulence is concentrated in low frequencies. So another requirement imposed is that it must also be a low pass filter because it is known that high frequencies are only system noise. Otherwise, errors in prediction would be amplified greatly. The desired location of all poles for this design is at z = 0.

3.5.1 Low Pass Filter Design

Since the designed controller will have all its poles at zero, the external feedback path will be perfectly cancelled unless the system model differs from the actual system. Therefore, the closed loop transfer function can be approached as though it was a finite impulse response (FIR) filter.

The time for the system to settle increases as the order of the low pass filter increases. So, the low pass filter should be as low order as possible while having the desired effect of reducing the high frequency noise. The FIR order chosen was 5 (4 zeros). One of these zeros was locked to z = 0.75 during the optimization for reasons that will become apparent later.

The optimization was implemented as a steepest descent method. The objective function is given in equation (3.36). The gradient of the objective function was found numerically by making small perturbations to $\bar{c}$. A constant coefficient of 10^{-4} on the gradient was used to keep the step size small. The sample time is normalized to 1.

$$\min_{\bar{c}} \quad \bar{u}^T \bar{u} \tag{3.26}$$

where $\bar{u} = f(\omega) - \left|\left(c_0 + c_1 e^{-j\omega} + c_2 e^{-j2\omega} + c_3 e^{-j3\omega}\right)\left(1 - 0.75 e^{-j\omega}\right)\right|$

ω is 1000 evenly spaced samples from 0 to π to generate the vectors

$$f(\omega) = \begin{cases} 1 & for \quad 0 < \omega < \dfrac{\pi}{2} \\ 0 & for \quad \dfrac{\pi}{2} < \omega < \pi \end{cases}$$

$$\bar{c} = \begin{bmatrix} c_0 & c_1 & c_2 & c_3 \end{bmatrix}^T$$

The optimized values for $C(z)$ are given in (3.27).

$$\begin{aligned} C(z) &= c_0 + c_1 z^{-1} + c_2 z^{-2} + c_3 z^{-3} \\ C(z) &= 0.350497 + 0.701633 z^{-1} + 0.701621 z^{-2} + 0.350479 z^{-3} \end{aligned} \tag{3.27}$$

The amplitude response of $(1\text{-}0.75z^{-1})C(z)$ is given in Figure 3.4. The zeros of this filter are shown in the Z-plane on the right of Figure 3.4. The actual zeros of this filter are

$$\bar{z} = \begin{bmatrix} 0.75 & -0.999980 & -0.500921 + 0.865474i & -0.500921 - 0.865474i \end{bmatrix}^T \tag{3.28}$$

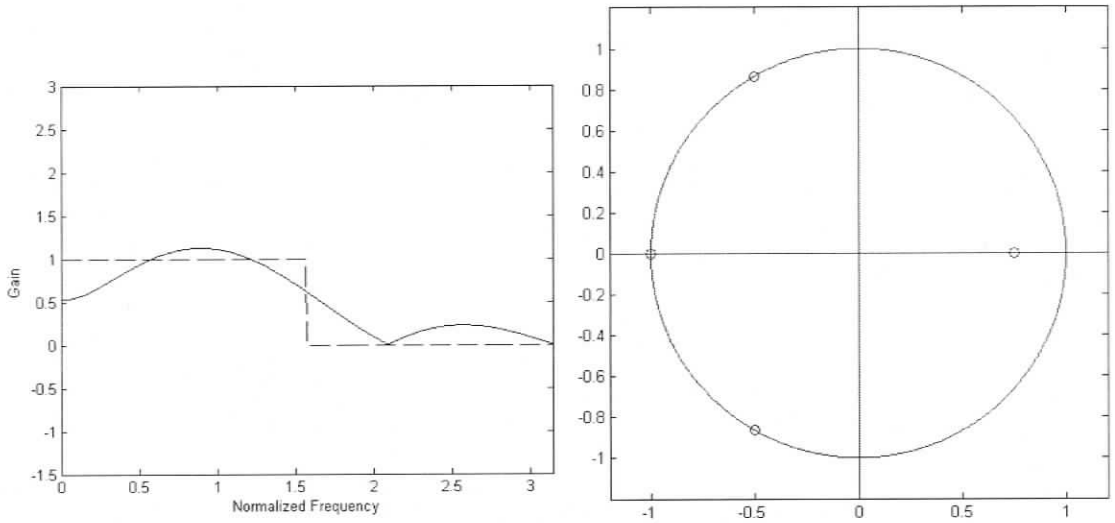

Figure 3.4: Amplitude response (left) and Z-plane zero placement (right) of an optimized 4 zero filter

3.5.2 Pole Placement Design Example

Now that the fixed portion of the controller has been defined, the arbitrary portion will now be found. Recall that the plant is to be controlled by two integrators and a low pass filter. The plant is modeled as two delays. The plant is the same as equation (3.11). Using the form discussed in section 3.3 for fixed aspects of the controller in Figure 3.2 we have

$$G_F(z) = \frac{0.350497 + 0.701633z^{-1} + 0.701621z^{-2} + 0.350479z^{-3}}{1 - 2z^{-1} + z^{-2}} \tag{3.29}$$

$$G_S(z) = \frac{0.350497z^{-2} + 0.701633z^{-3} + 0.701621z^{-4} + 0.350479z^{-5}}{1 - 2z^{-1} + z^{-2}} \tag{3.30}$$

$$A(z) = 1 - 2z^{-1} + z^{-2} \tag{3.31}$$

$$B(z) = 0.350497z^{-2} + 0.701633z^{-3} + 0.701621z^{-4} + 0.350479z^{-5} \tag{3.32}$$

In this case, m = 5 and n = 2. D(z) shall again be 1 as in equation (3.14). Placing A(z), B(z) and D(z) into the form given in (3.7) gives

$$\begin{bmatrix} 1 & 0 & 0 & 0 & 0 & 0 \\ -2 & 1 & 0 & 0 & 0.350497 & 0 \\ 1 & -2 & 1 & 0 & 0.701633 & 0.350497 \\ 0 & 1 & -2 & 1 & 0.701621 & 0.701633 \\ 0 & 0 & 1 & -2 & 0.350479 & 0.701621 \\ 0 & 0 & 0 & 1 & 0 & 0.350479 \end{bmatrix} \begin{bmatrix} \alpha_1 \\ \alpha_2 \\ \alpha_3 \\ \alpha_4 \\ \beta_0 \\ \beta_1 \end{bmatrix} = \begin{bmatrix} 0 \\ 0 \\ 0 \\ 0 \\ 0 \\ 0 \end{bmatrix} - \begin{bmatrix} -2 \\ 1 \\ 0 \\ 0 \\ 0 \\ 0 \end{bmatrix} \tag{3.33}$$

$$\begin{bmatrix} \alpha_1 \\ \alpha_2 \\ \alpha_3 \\ \alpha_4 \\ \beta_0 \\ \beta_1 \end{bmatrix} = \begin{bmatrix} 2.00000000000000 \\ 2.25044732919323 \\ 1.58340830874136 \\ 0.58295446920394 \\ 2.13854184561761 \\ -1.66330866413883 \end{bmatrix} \tag{3.34}$$

So, this will give one zero at 0.764 (previously locked at z = 0.75) and four more poles for the controller. $G_A(z)$ in figure 3.2 becomes equation (3.35).

$$G_A(z) = \frac{\beta(z)}{\alpha(z)} = \frac{2.138542 - 1.633087z^{-1}}{1 + 2z^{-1} + 2.250447z^{-2} + 1.583408z^{-3} + 0.582954z^{-4}} \tag{3.35}$$

The combination of $G_A(z)$ and $G_F(z)$ is the controller. Note that $C(z)$ is from equation (3.27).

$$G_C(z) = G_A(z)G_F(z) = \left(\frac{\beta(z)}{\alpha(z)}\right)\left(\frac{(1-0.764z^{-1})C(z)}{1-2z^{-1}+z^{-2}}\right)$$
$$\frac{0.749553 + 0.917486z^{-1} + 0.333415z^{-2} - 0.417499z^{-3} - 0.582954z^{-4}}{1 - 0.749553z^{-2} - 0.917486z^{-3} - 0.333415z^{-4} + 0.417499z^{-5} + 0.582954z^{-6}} \tag{3.36}$$

Type 2 controllers can be perceived as difficult to implement because they tend to be numerically unstable. Chapter 4 provides an implementation scheme of this system that is stable despite coefficient rounding and output quantization.

3.6 Theoretical Characteristics of Designs

The controllers studied are the standard single delay integrator control system common to astronomical adaptive optics (CAO), as well as the Type 1 and Type 2 systems designed in sections 3.4 and 3.5. The controller transfer functions (I.e. $G_c(z)$ in Figure 3.2) are

$$G_{CAO}(z) = \frac{1}{1 - z^{-1}} \tag{3.37}$$

$$G_{T1}(z) = \frac{0.5 + 0.5z^{-1}}{1 - 0.5(z^{-2} + z^{-3})} \tag{3.38}$$

$$G_{T2}(z) = \frac{0.7496 + 0.9174z^{-1} + 0.3333z^{-2} - 0.4175z^{-3} - 0.5829z^{-4}}{1 - 0.7496z^{-2} - 0.9174z^{-3} - 0.3333z^{-4} + 0.4175z^{-5} + 0.5829z^{-6}} \tag{3.39}$$

As discussed previously, the system external to the controller is modeled as two delays, z^{-2}, in the optical path. Therefore, the closed loop transfer functions of the controlled systems are as shown below. These closed loop systems were all implemented with a variable gain, g.

$$T_{CAO}(z,g) = \frac{gz^{-2}}{1 - z^{-1} + gz^{-2}} \tag{3.40}$$

$$T_{T1}(z,g) = \frac{0.5g(z^{-2} + z^{-3})}{1 + 0.5(g-1)(z^{-2} + z^{-3})} \tag{3.41}$$

$$T_{T2}(z,g) = \frac{g(0.7496z^{-2} + 0.9174z^{-3} + 0.3333z^{-4} - 0.4175z^{-5} - 0.5829z^{-6})}{1 + (g-1)(0.7496z^{-2} + 0.9174z^{-3} + 0.3333z^{-4} - 0.4175z^{-5} - 0.5829z^{-6})} \tag{3.42}$$

Obviously, the denominators of $T_{T1}(z,g)$ and $T_{T2}(z,g)$ are equal to 1 when g is 1. This makes the closed loop system operate as though it was an FIR filter. $T_{CAO}(z,g)$, which is common to operating adaptive optics systems in astronomy, does not have such a condition.

3.6.1 Range of Closed Loop Stability

Each controller is only stable for a particular range of gain. This can be solved with the either the Jury Stability Test [11] or finding the gain when the root locus first crosses the unit circle. The following table provides the gain ranges of the studied controllers.

Controller	Minimum Gain	Critically Damped	Maximum Gain
CAO	0	0.25	1
Type 1	0	1	$\sqrt{5}$
Type 2	0	1	1.438

Table 3.1: Ranges of stability and critically damped gain values for the three controller models

In order to make a fair comparison between all systems, the critically damped case will be used for response and bandwidth analysis. When a system is critically damped, the poles of the system are all real valued, but can become complex if the gain is increased.

3.6.2 Root Locus

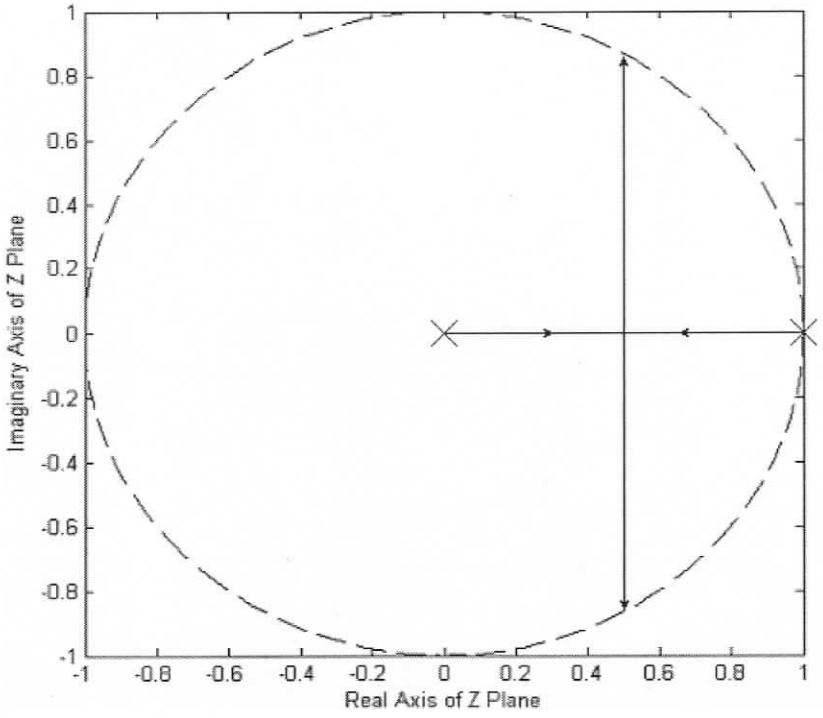

Figure 3.5: Root locus of a CAO controller

The root locus shows how the poles of the closed loop system change as the gain is varied. The 'X' markings are the initial locations of the poles when the gain is equal to 0. The 'O' markings are the zeros of the system. The lines show how the position of the poles change as the gain is increased. These poles move from the 'X' to a 'O' or towards infinity.

Such plots can help the designer visualize if the system can behave as desired with only a change of gain. The settling time of the response of the system is dependant on the distance from the center of the unit circle to the furthest pole. It is shown in Figure 3.5 that the CAO method has a minimum radius of 0.5 when the system is critically damped. The gain at this point is equal to 0.25. In contrast, the minimum radial distance for the Type 1 system is equal to 0. This is shown in Figure 3.6. Likewise, the Type 2 system was also designed to have all the poles converge on $z = 0$ at one gain value, see Figure 3.7. However, speed of the response is not only determined by the pole locations. When the poles are at $z = 0$, the speed becomes highly dependant on the number of closed loop zeros. With more zeros comes a slower response.

The angle between the positive real axis and a radial line is related to the temporal frequency. Examples are that half the sampling frequency relates to the negative real axis and a quarter of the sampling frequency relates to the positive imaginary axis. The distance between a pole and a point on the unit circle is inversely proportional to the amplification of the input signal at the respective frequency. The closer the pole gets to a point on the unit circle, the more the input signal is amplified for the respective frequency. The opposite is true for zeros. The closer a zero is to this same point, the more the input signal is attenuated.

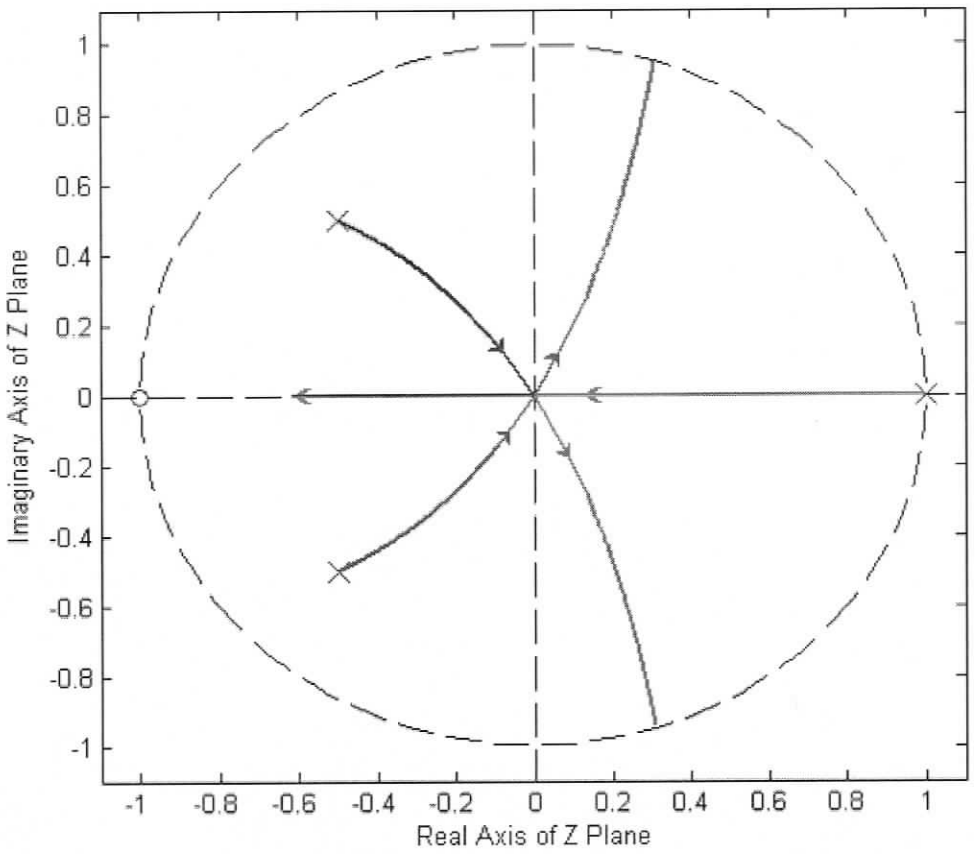

Figure 3.6: Root locus of the Type 1 controller

As the gain of all the systems is increased from the critically damped point, the poles become complex conjugate and diverge from each other. This does two things; (i) increases the amplification of low frequency input signals and (ii) increases the frequency of maximum amplification. This increases the bandwidth of the closed loop system at the same time that the noise amplification is increased.

Figure 3.6 shows that there is a zero on the negative real axis directly on the unit circle. This means that there is 0 distance between the zero and the point corresponding to half the sample frequency, therefore that frequency is attenuated to 0.

The root locus diagram in Figure 3.7 is of the Type 2 system. It has four zeros and six poles. Two of these poles are integrators ($z = 1$). The zero at 0.764 steers these two

poles around it to reach z = 0 along with the other poles when gain is equal to 1. The other three zeros are on the unit circle so the signal at 1/2 and 1/3 of the sampling rate is attenuated to 0.

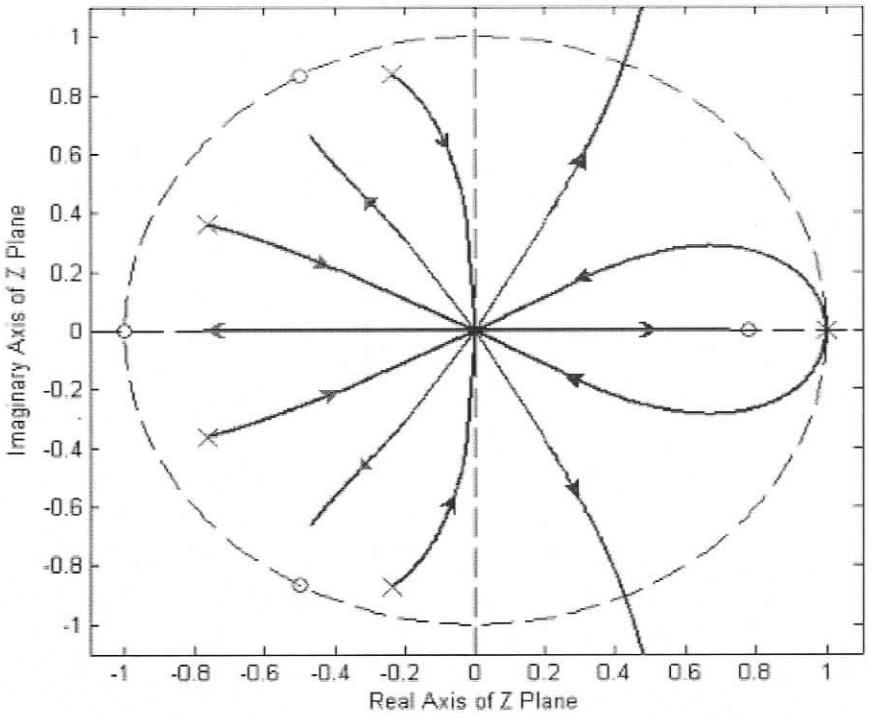

Figure 3.7: Root locus of the Type 2 controller

3.6.3 Closed Loop Impulse Response

The discrete impulse response shows how a system responds when the input signal is zero for all samples except for sample 0. At sample 0 the input signal is equal to 1. This can show how the system reacts to a given sample of noise and the time that it remains in the system.

All these systems generally have infinite impulse responses (IIR) due to the feedback. The exception to this is when $g = 1$ for the Type 1 and Type 2 cases. For this gain value these two systems have a finite impulse response (FIR) because the feedback paths cancel.

The number of samples required for the critically damped Type 1 and Type 2 systems to settle after an impulse is equal to number of coefficients of the equivalent FIR filter plus the two samples required to get the impulse through the sensor and into the controller. So, the Type 1 system settles in 4 samples and the Type 2 system settles in 7 samples. The Type 2 system reacts rather violently compared to the other systems. This is due to the predictive nature of the system. The initial impulse is assumed to be a ramp in the positive direction. Then when the input returns to 0 on the next sample, it appears that the ramp is in the negative direction. This settles out when the system has had time to lock on to the zero magnitude input signal.

The CAO controller is essentially an IIR filter. This particular system does not settle as fast. From Figure 3.8, the system settles in 10 or 11 samples. However, it has the smallest immediate reaction to the impulse of 0.25.

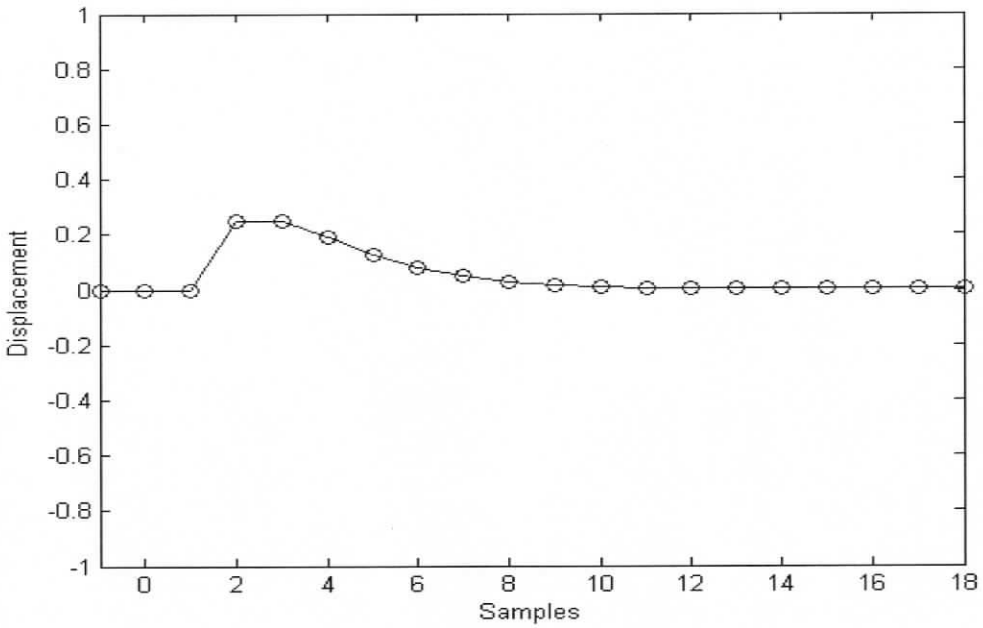

Figure 3.8: Impulse response of the closed loop CAO system

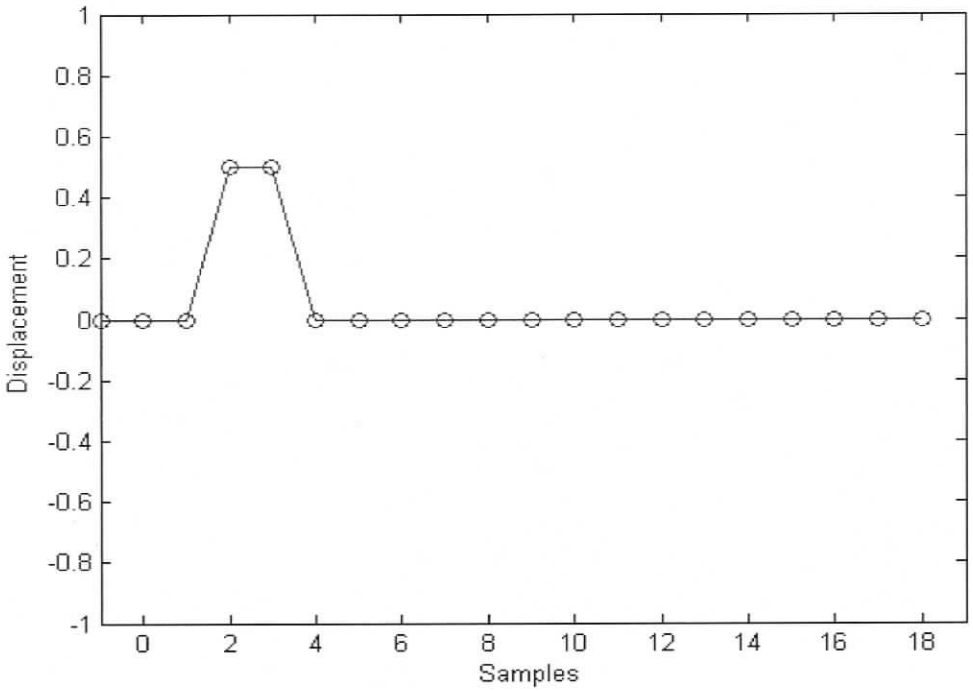

Figure 3.9: Impulse response of the closed loop Type 1 system

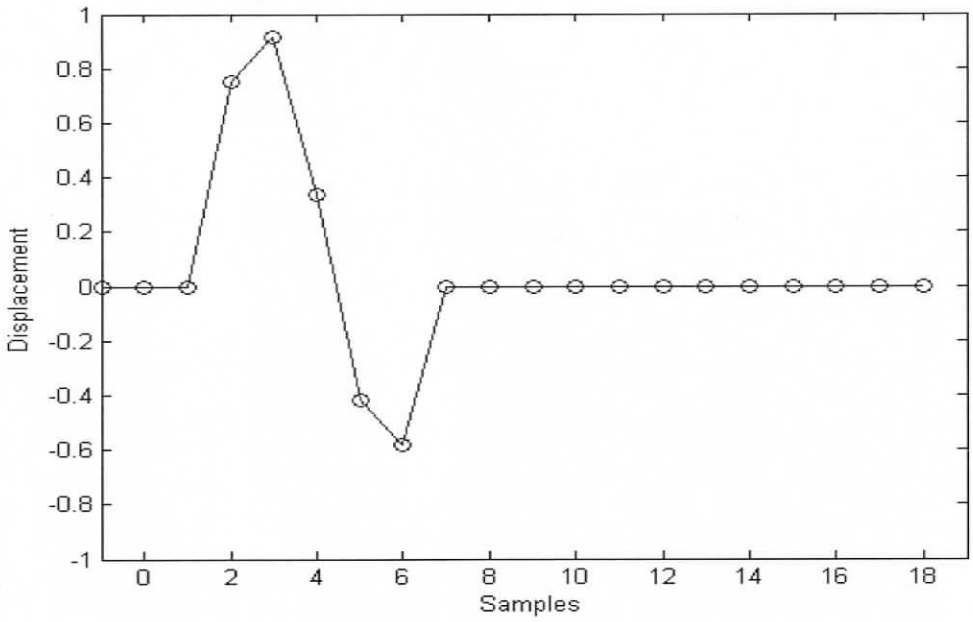

Figure 3.10: Impulse response of the closed loop Type 2 system

3.6.4 Closed Loop Step Response

The step response shows how long it takes for the system to settle on a new constant input. When the output signal is within the dashed lines, the system has settled to within 5% of the steady state input. It takes a critically damped CAO system 8 samples to settle on a constant input. The Type 1 system requires only 3 samples and the Type 2 system requires 6. Obvious trade offs for the Type 2 system is the large overshoot that peaks at the 4th sample at a value of 2 and the slower response time than the Type 1 system.

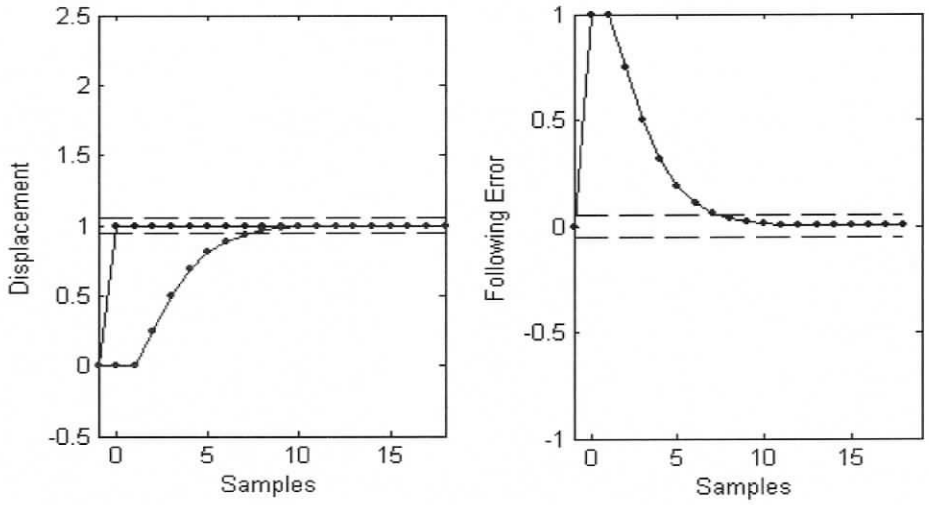

Figure 3.11: Step response of the closed loop CAO system (left) and the following error (right)

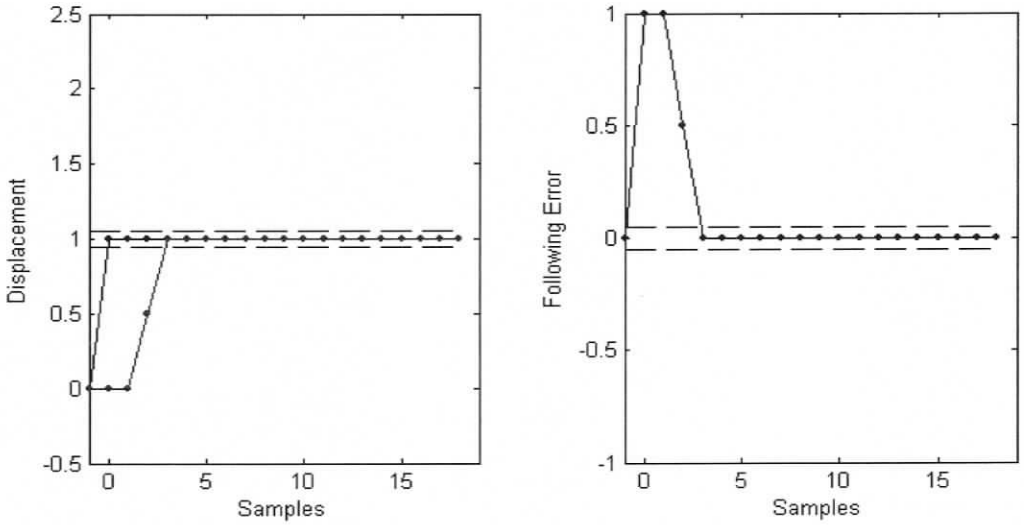

Figure 3.12: Step response of the closed loop Type 1 system (left) and the following error (right)

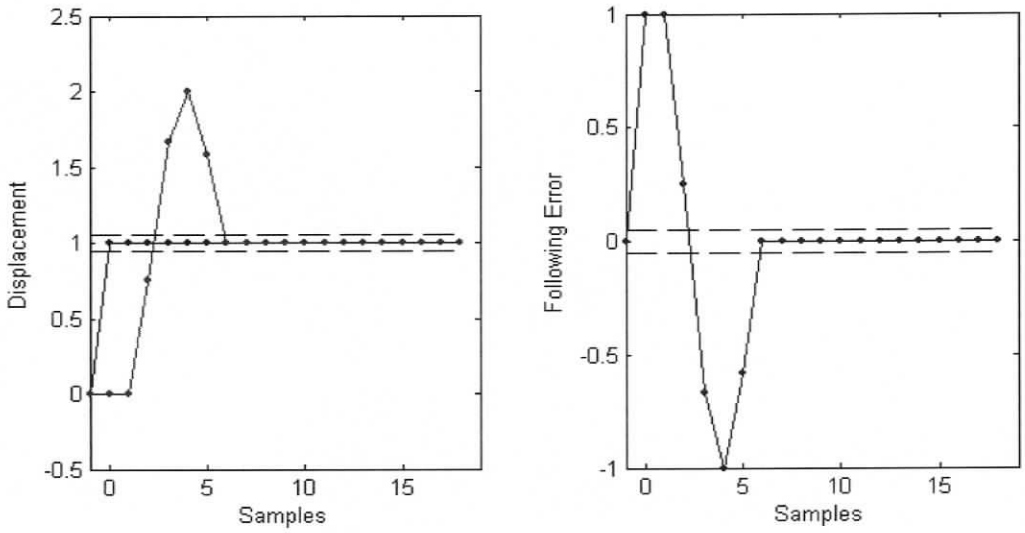

Figure 3.13: Step response of the closed loop Type 2 system (left) and the following error (right)

3.6.5 Closed Loop Ramp Response

Impulse and step inputs are not realistic inputs to the system. The system input is low frequency signals. If the frequency is low, it can be approximated by a series of ramps. The ramp response shows how much steady state following error there is in each system. The steady state value of the error can be found analytically with the methods of [11].

$$K_v = \lim_{z \to 1} \left[\frac{1 - z^{-1}}{T} G(z) \right] \tag{3.43}$$

$$e_{ss} = \frac{1}{K_v} \tag{3.44}$$

The value of e_{ss} is the following error to a unit ramp. The value of T is the sample time. In the following diagrams T is equal to 1. The functions that can be used as $G(z)$ are the open loop transfer functions of the three systems given as equations (3.37) to (3.39). The steady state ramp error for the CAO and Type 1 systems are given in the equations below.

$$K_{vCAO} = \lim_{z\to 1}\left[\left(\frac{1-z^{-1}}{T}\right)\left(\frac{gz^{-2}}{1-z^{-1}}\right)\right] = \frac{g}{T} \tag{3.45}$$

$$K_{vT1} = \lim_{z\to 1}\left[\left(\frac{1-z^{-1}}{T}\right)\left(\frac{0.5g\left(z^{-2}+z^{-3}\right)}{\left(1-z^{-1}\right)\left(1+z^{-1}+0.5z^{-2}\right)}\right)\right] = \frac{g}{2.5T} \tag{3.46}$$

The CAO gain is 0.25, so the respective K_v value is 0.25. This gives a steady state ramp error of 4. The gain of the Type 1 system is 1, so the theoretical K_v is 0.4. Therefore the error will be 2.5. Figures 3.14 and 3.15 show the response of the models to the ramps and that the steady state error is the same as the above calculations.

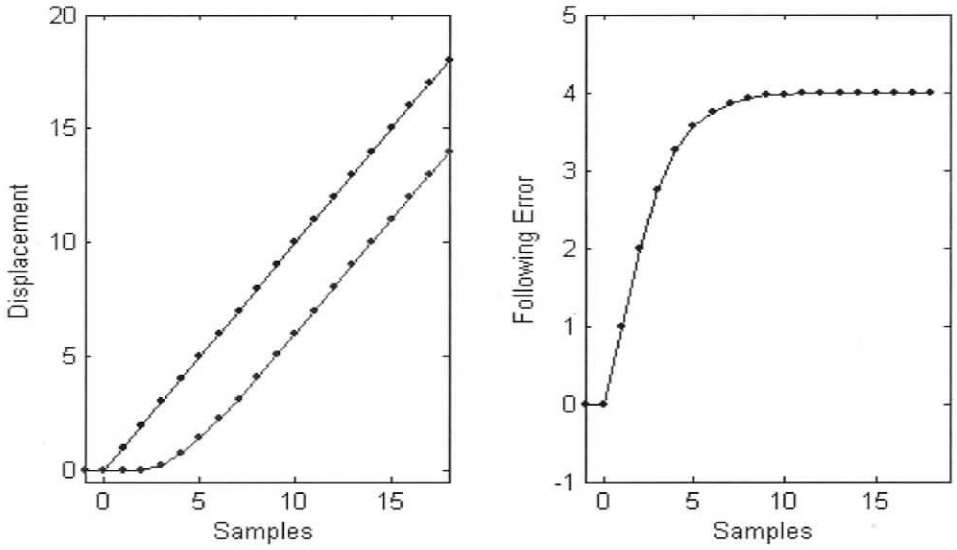

Figure 3.14: Ramp response of the closed loop CAO system (left) and the following error (right)

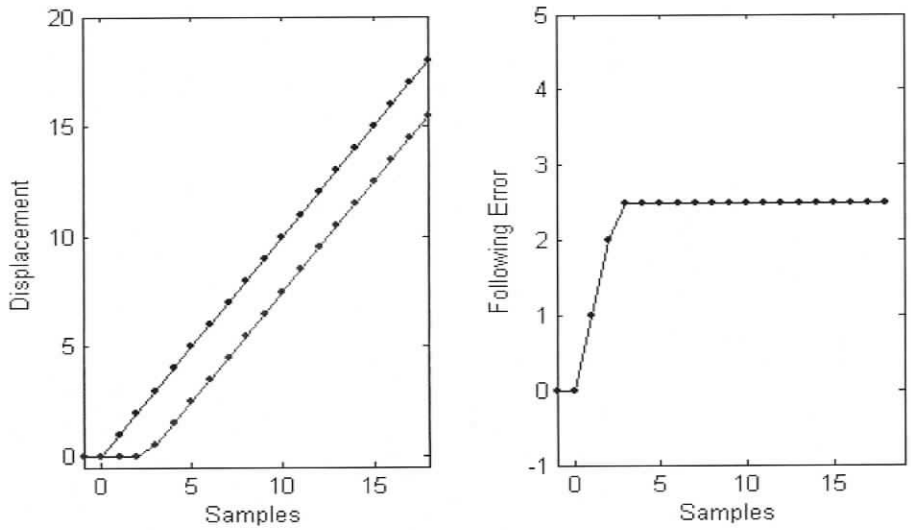

Figure 3.15: Ramp response of the closed loop Type 1 system (left) and the following error (right)

Finally, the Type 2 system shows where it is best suited. It provides zero following error of a ramp in just 6 samples. The Type 2 system has two integrators, therefore K_v is infinite. This means that the steady state ramp error for a Type 2 system is 0. This is also the case for the simulation presented in Figure 3.16. Note that the controller is getting the measurement two samples after the event occurred. Therefore, the controller is predicting the atmospheric turbulence measurement by two samples to predict an appropriate control signal to keep the error at 0.

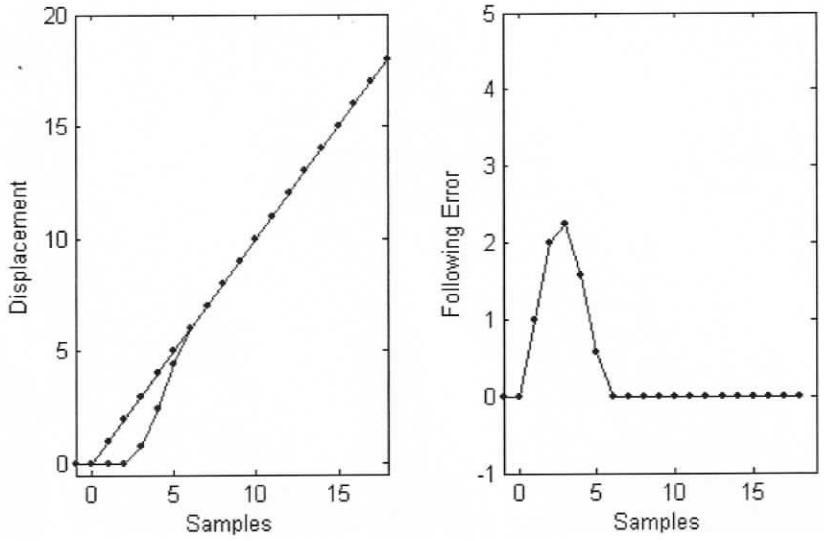

Figure 3.16: Ramp response of the closed loop Type 2 system (left) and the following error (right)

3.6.6 Closed Loop Amplitude and Phase Responses

The amplitude response is the magnitude of the ratio of the power spectrum of the output signal to the power spectrum of the input signal. This shows how the input is amplified or attenuated as it is transformed into the output signal. The phase response shows how the input signal is delayed before affecting the output signal.

This section shows the amplitude responses of the DM to either an input signal of the turbulent atmosphere or the noise generated by the WFS. Both of these input signals can be considered to be generated at the same point in the control system. These amplitude response plots are generally used to see how the noise signal will be amplified or attenuated.

Figure 3.17 shows the responses of the critically damped CAO system which is equation (3.40) with g = 0.25. The Type 1 system is equation (3.41) with g = 1. Figures 3.18 and 3.19 illustrate that the Type 1 system also does not amplify the noise. Its phase delay is less than the CAO approach, which is why there is an improvement in the 0dB bandwidth shown in Figure 3.24.

The Type 2 system is equation (3.42) with $g = 1$. Its response shown in Figure 3.20 shows that the input can be amplified higher than 0dB. It is expected that noise would be the only significant signal affected by this amplification. However, the peak amplification is approximately 7.7 dB which is similar to the CAO system with a gain of 0.7 as shown in Figure 2.2. The phase response of the Type 2 system is shown along with the phase response of a simple two sample delay system. This is to illustrate that the Type 2 system has less phase delay for the low frequency spectrum than the two sample delay caused by the interaction of the DM, WFS and the computer. This means that the Type 2 system is making some prediction of the future value of the input until 9% of the

sampling rate. This prediction can be seen from the ramp response plot in figure 3.16 of the previous section. Note that 10^0 is 1 and represents 100% of the sampling rate.

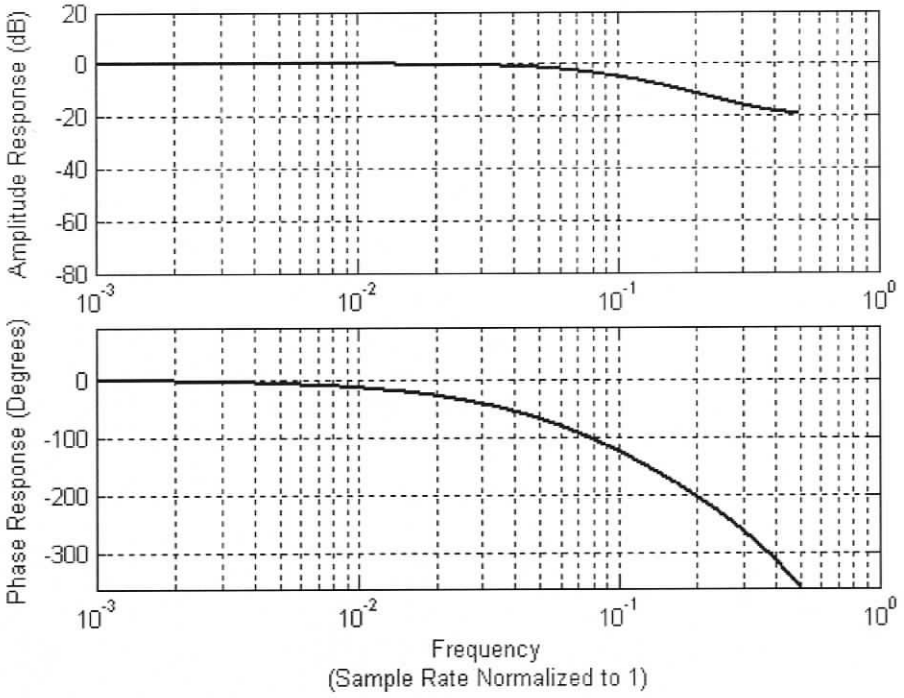

Figure 3.17: Amplitude and phase response of the critically damped closed loop CAO system

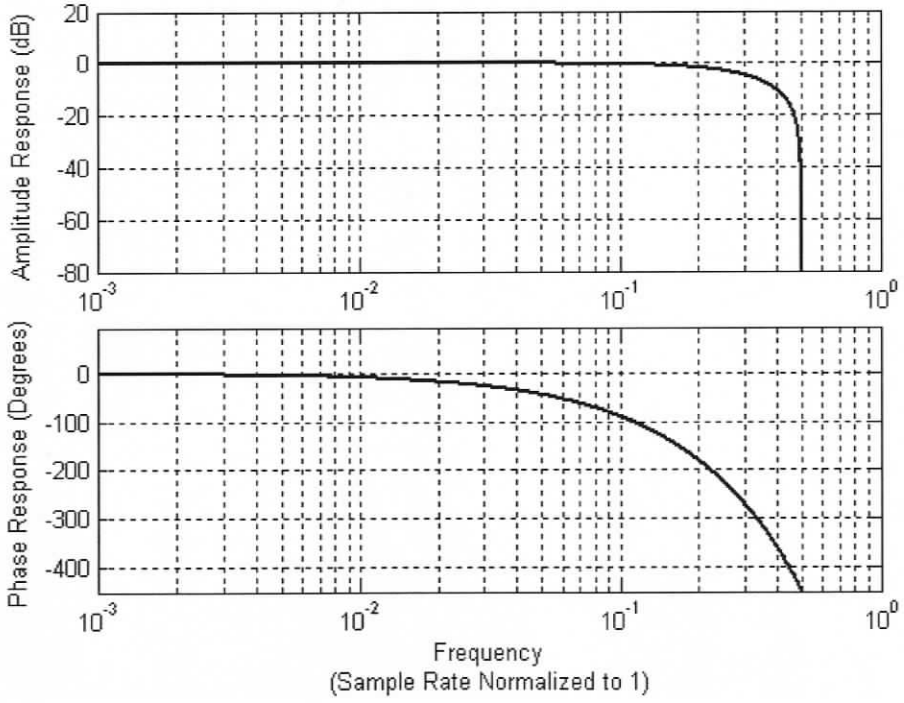

Figure 3.18: Amplitude and phase response of the critically damped closed loop Type 1 system

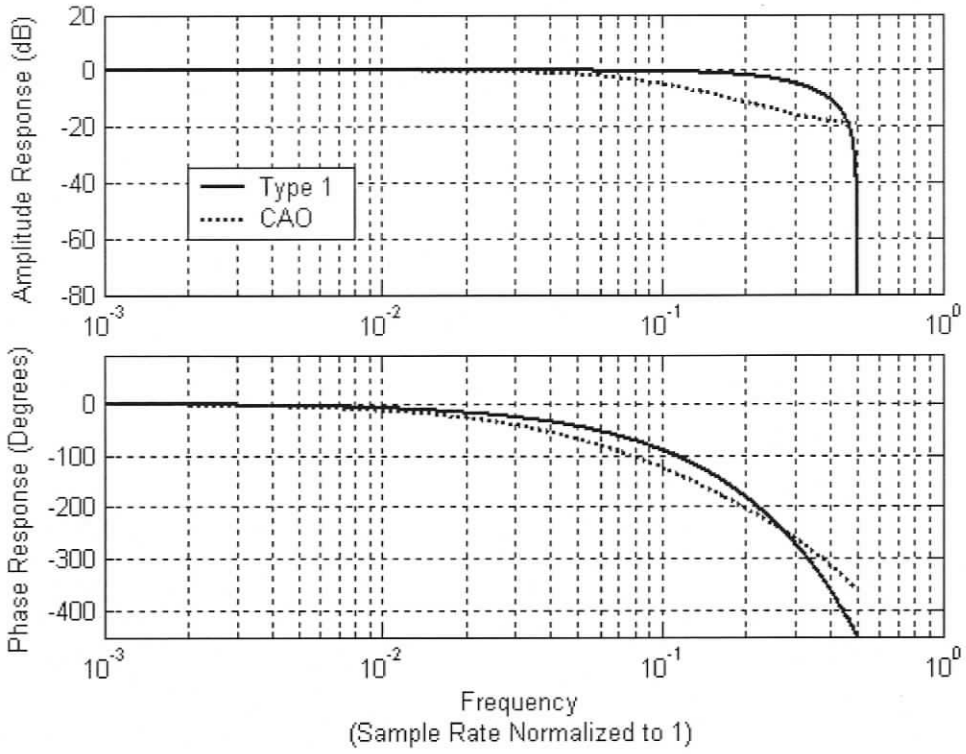

Figure 3.19: Amplitude and phase responses of the critically damped closed loop CAO and Type 1 systems

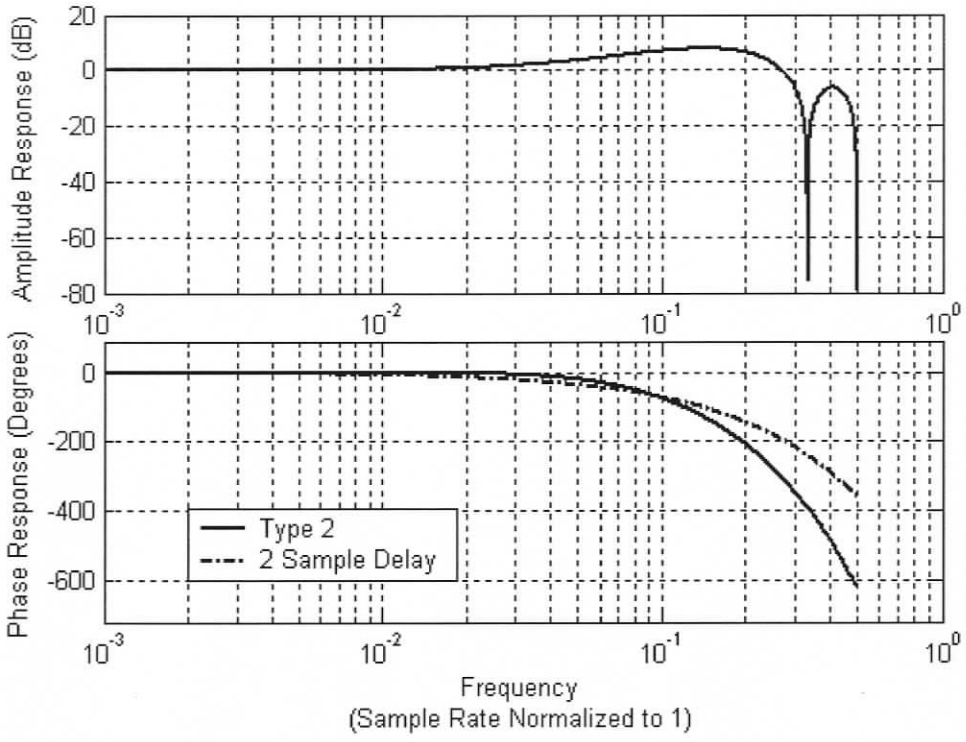

Figure 3.20: Amplitude and phase responses of the critically damped closed loop Type 2 system and 2 delays

3.6.7 Theoretical Rejection Ratio

Another important signal to study is the error signal. The goal of this system is to bring the error to 0. The rejection ratio is a term used in adaptive optics for the amplitude response of the error signal to the input signal in the absence of noise. This is the absolute value of the general form of equation (2.6). Multiplying the input signal with the rejection ratio gives the expected error spectrum in the absence of noise. The input signal occupies the very low frequencies compared to the sampling rate, so only the response up to the first crossing of the 0dB line is important for following atmospheric turbulence. The frequency relating to this point is called the 0dB bandwidth.

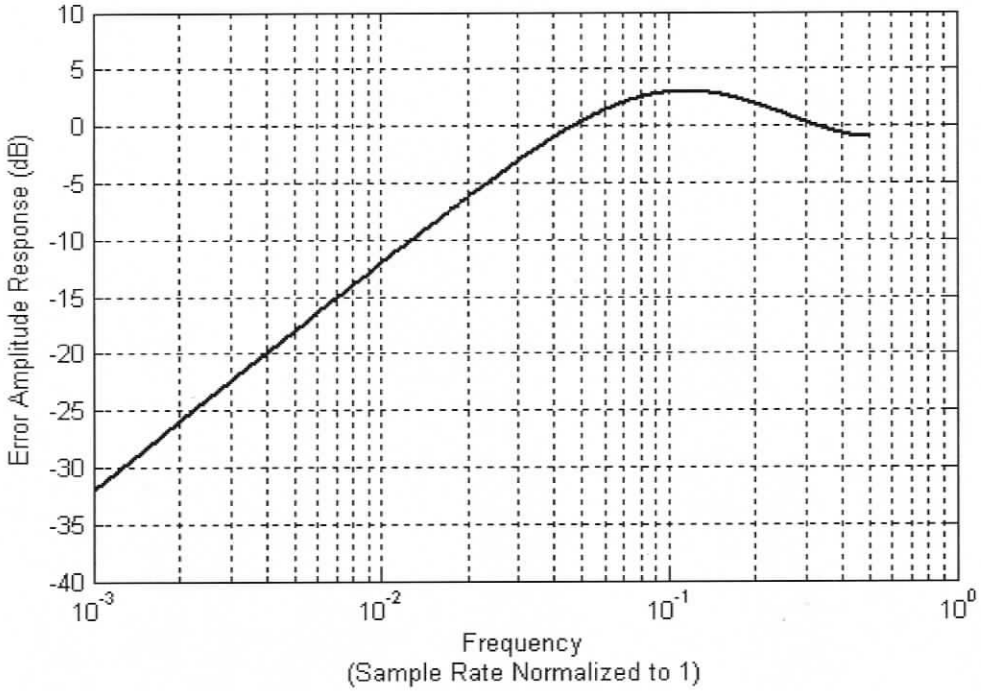

Figure 3.21: Rejection ratio of the critically damped closed loop CAO system

The error amplitude response shown in Figure 3.21 is the critically damped CAO system. Its 0dB bandwidth is approximately 4.5% of the sampling rate. From this point, the slope toward 0 Hz is 20dB/decade as expected from a system with a single integrator for control. However, the -20dB point is at 0.4% showing that the slope is not exactly

20dB/decade at the 0dB point. Therefore a fair approximation of the bandwidth may be 4%.

The Type 1 system has a 0dB bandwidth of about 6.5% and a -20dB point at 0.65%. So for this system the 20dB/decade slope is true up to the 0dB point. Therefore, the Type 1 system has an increase of 62.5% real bandwidth over the CAO system without amplifying the quantization noise.

Finally, the Type 2 system has a 0dB bandwidth of 6% of the sampling rate. However, from this point the slope is 40dB/decade towards zero Hz. It has a -20dB point of about 1.9% of the sampling rate. The frequency points that correspond to -20dB on Figure 3.24 can be used to see this comparison. This means that that the frequency that has 10% peak following error (-20dB) is almost 5 times higher in frequency for the Type 2 system over the critically damped CAO method.

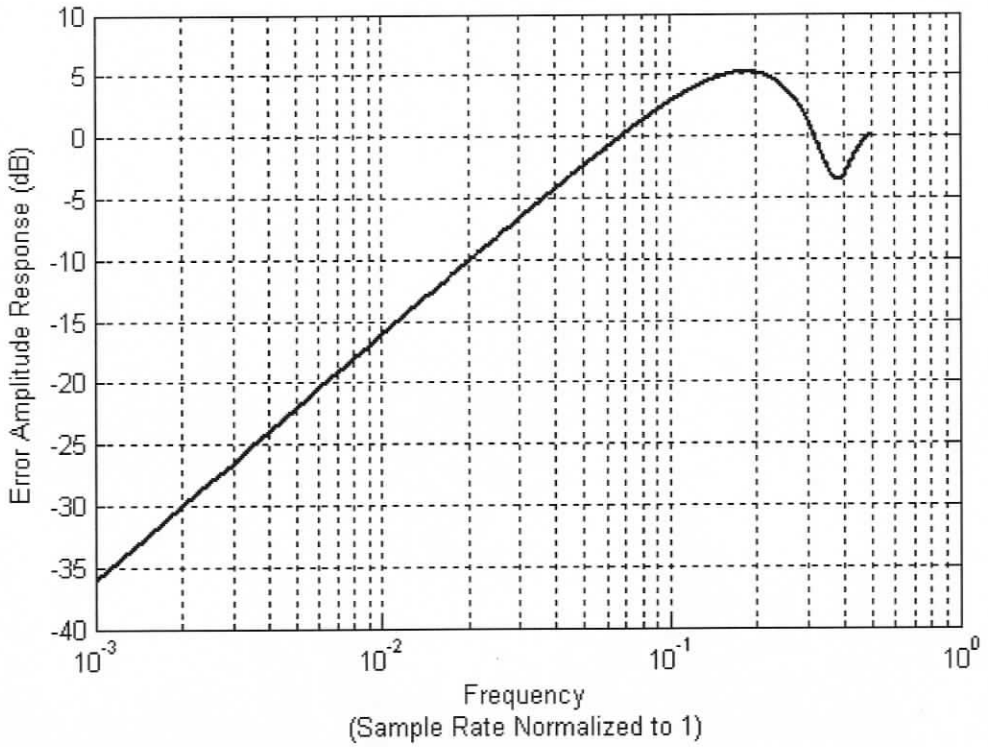

Figure 3.22: Rejection ratio of the critically damped closed loop Type 1 system

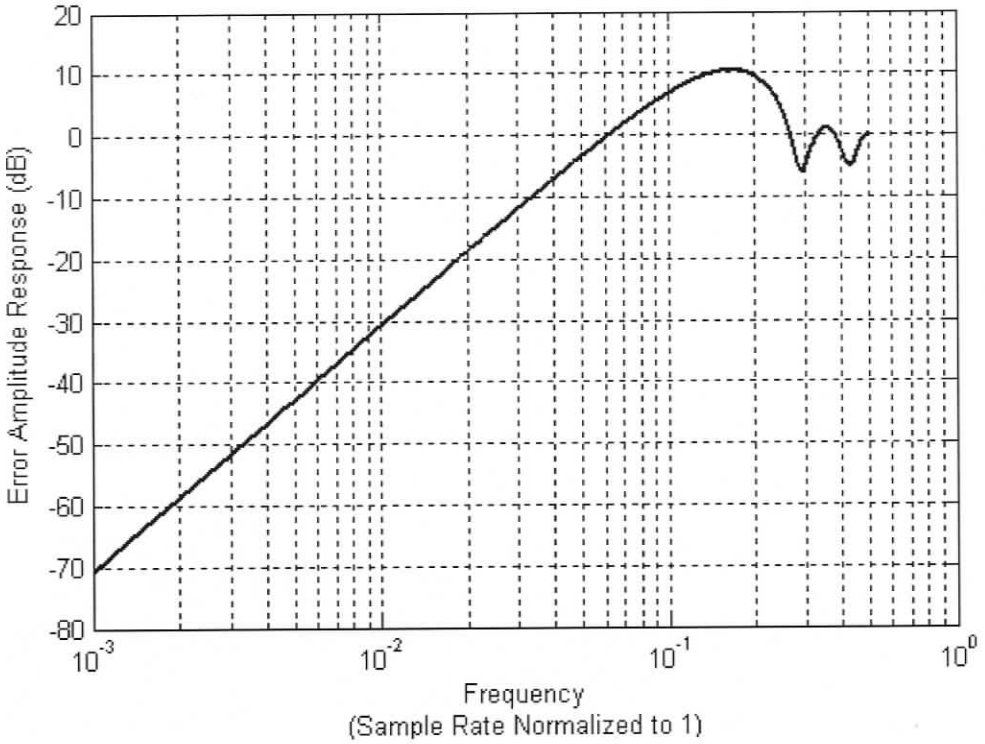

Figure 3.23: Rejection ratio of the critically damped closed loop Type 2 system

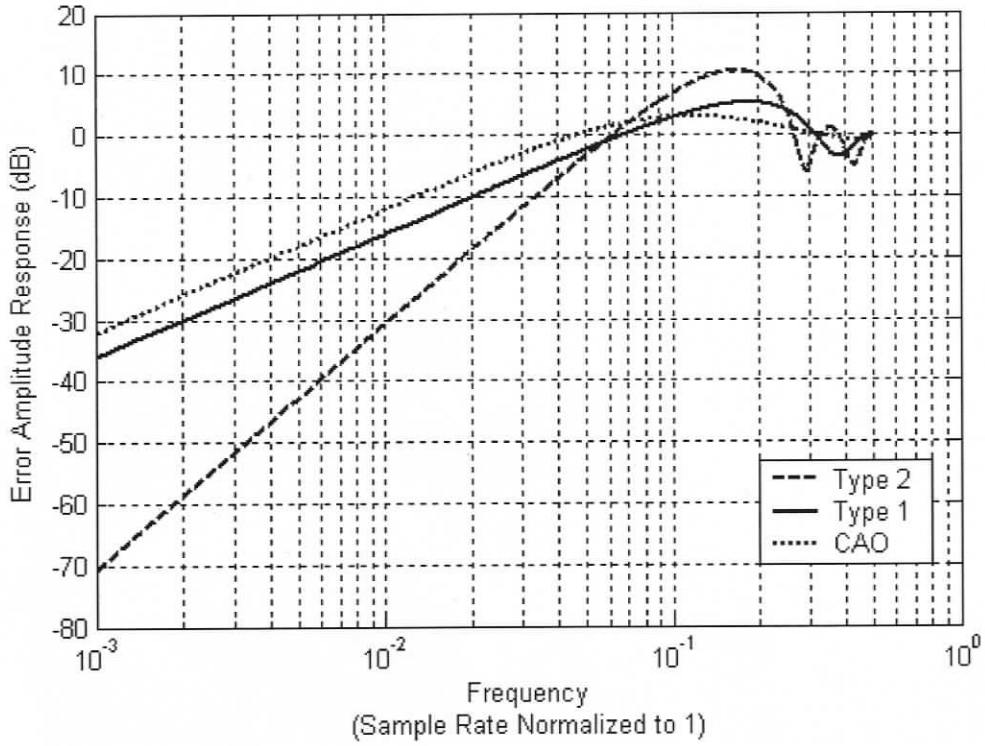

Figure 3.24: Comparison of the error amplitude responses of the three critically damped systems

Alternatively, the amount of correction at 0.4% of the sampling rate can be compared. The CAO method will have 10% error at this frequency, the Type 1 system will have 6.3% error and the Type 2 system will have 0.47% error. The Type 2 system can follow a low frequency input signal with orders of magnitude less error than the single integrator control of the CAO and Type 1 methods. The trade off is the amplification of noise. This system would be very useful if the noise on the input signal can be guaranteed to be small.

Error (dB)	Error (%)	CAO BW (%)	Type 1 BW (%)	Type 2 BW (%)
0	100	4.5	6.5	6
-3	70.7	3	4.6	5.1
-6	50	2.1	3.2	4.2
-20	10	0.4	0.65	1.9

Table 3.2: Theoretical bandwidth for various amplitudes of error

The rejection ratio is useful to determine the noiseless error, but the real following error is the error transfer function multiplied by the input plus the noise that propagates to the DM. The trade off between noise amplification and the 0dB bandwidth is balanced to minimize the real error. The noise source is the WFS. The DM noise is ignored for now.

$$Output(z) = T(z)(Input(z) + Noise(z)) \tag{3.47}$$

$$Error(z) = Input(z) - Output(z) \tag{3.48}$$

$$Error(z) = (1 - T(z))Input(z) - T(z)Noise(z) \tag{3.49}$$

3.7 Conclusions

The Sylvester matrix is always size $2n$ by $2n$, where n is the order of $A(z)$ or $B(z)$ (which ever is higher). The Reduced Sylvester matrix formulation used here uses a matrix that is $n+m-1$ by $n+m-1$ which is always smaller than the Sylvester matrix. This improvement was found because the Sylvester matrix is for the general case for arbitrary $A(z)$, $B(z)$ and $D(z)$. The reduced method presented in section 3.2 is for digital control systems that will

always have $a_o = \alpha_o = d_o = 1$ and $b_o = 0$. The simple design example shown in section 3.3 would have been solved with a 4 by 4 Sylvester matrix, as opposed to 2 by 2 with the reduced form.

The Type 1 system designed in section 3.4 required averaging of the desired output signal in order to attenuate the Nyquist frequency noise 0. This was done because the unfiltered controller could follow the Nyquist frequency as though it was a zero Hz signal. The even and odd samples were completely decoupled, so a steady state difference between them developed.

The Type 2 system designed in section 3.5 was also filtered. This was to reduce the noise amplification. A fixed zero was assumed to be at z = 0.75 for the optimization process. The Reduced Sylvester matrix determined that this zero must be placed at 0.764. This was considered to be close enough to the assumed value to not require another filter optimization.

The critically damped Type 1 system provides 62.5% higher real bandwidth than the critically damped CAO system. This was accomplished with out amplifying any frequency. It is conceded that this method does not attenuate the upper frequencies as well as the CAO method. However, this should not be a noticeable difference since the noise source is sensor quantization, and is followed by the output quantizer. The output should have coarser quantization than the input sensor.

The Type 2 system has lower following error by orders of magnitude over the other two presented systems. Its limitation is that it amplifies noise as well. This may be acceptable as the peak is approximately the same as when the gain is high in a CAO system.

Chapter 4

Implementation

The controllers designed in Chapter 3 will be used to control the DM to produce the desired wave front correction. The DM is illuminated on a circular section that is 2.74 mm (10 actuators) in diameter. The WFS is consequently illuminated on a circular section that is 9 lenslets in diameter. This creates a control problem with 80 outputs (illuminated DM actuators) with 122 inputs (x and y measurements for 61 illuminated WFS lenslets). Instead of solving this as a 2D problem, the approach used here is based on using a set of decoupled parallel 1D controllers that each control an orthogonal mode measured by the WFS. The interaction between these DM modes and the WFS is measured during the initialization process in order to convert WFS measurements into modal error. The process of converting WFS measurement to modal error is also discussed in section 4.1.8.

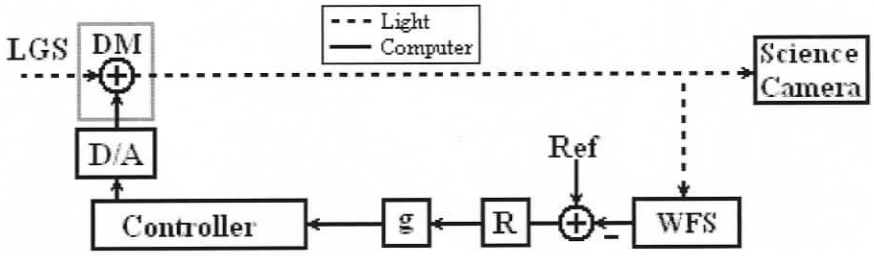

Figure 4.1: Closed loop system layout

Figure 4.1 shows the closed loop system layout. The light from the laser guide star (LGS) reflects off the DM and is split. Part of the light proceeds to the science camera and the rest is captured by the WFS, which converts the light into a digital picture. The current measurement of the WFS spot positions are subtracted from the

reference positions, denoted by 'Ref' in Figure 4.1. This WFS error signal is multiplied by the reconstructor matrix, R, to obtain the modal error. This error is multiplied by a gain, g. Then this signal is given to the controller. The controller, consisting of parallel 1D controllers (one for each mode) generates a set of new actuator positions and sends this data to the D/A converter.

In this chapter, different approaches to create a set of orthogonal modes are presented. A problem faced when building these sets are the invisible modes of the system. These are shapes that the DM can produce that the WFS can not detect. These occur because the WFS measures the wavefront at discrete sample points rather than provide a measurement of the continuous shape. For example, the WFS is confused by aliasing when the DM alternates the actuators to high and low in a checkerboard pattern. This creates "saddle" shapes at all the WFS measurement points and the measured slope would be 0, incorrectly indicating that the wavefront is flat. Such invisible shapes can be produced when the actuators of the DM are free to actuate independently. This is only one of many possible shapes that cause some amount of aliasing in the sensor and must be removed for the system to be stable.

A common problem in discrete control systems is signal quantization. This has been discussed in the literature for finite word length systems where all computations in the controller are precision limited to a certain number of bits [14][15][16]. For such systems, the round off needs to be treated as an unknown noise source and methods are given for making a controller robust in spite of quantization. The controllers are optimized to minimize the effect of the unknown noise signals.

There are two locations in the UVic AO system where quantization is an issue: (i) the unknown noise source within the WFS, and (ii) the output control voltage to each DM actuator supplied by the 8-bit D/A card. Section 4.2 provides a method to incorporate the control signal quantization into the controller for improved performance.

4.1 Modal Control

4.1.1 Motivation

The WFS detects planar wave front aberrations and the DM is shaped in order to flatten the wave front. The controller was implemented using a modal control scheme. This means that the actuators move to form the sum of well-defined shapes, rather than moving independently. When the DM actuators move independently, shapes can develop that have higher spatial frequency than the Nyquist frequency of the WFS. By defining the shapes that are permitted to appear on the DM, this source of aliasing can be eliminated.

It was shown by Dai [17] that an error is caused by the cross talk between the individual modes of any orthogonal modal set that are sensed by a WFS unless its set of derivatives are also orthogonal. Dai did not provide such a set and one is not provided here. This error develops from high order modes that are present in the wave front that are not part of the modal set used by the sensor. These high order modes are sensed as parts of lower order modes, so this corresponds to a form of aliasing error. So, it would be desirable for the given sampling geometry to be able to include as many modes as possible in the sensor that could be present in the turbulence. It was shown by Dai that given a 6x6 WFS, the Zernike modes discussed in section 4.1.2 were limited to 25

modes. The set of Cartesian based modes given in section 4.1.4 could use a set of 35 modes for the same sensor as reported in [18].

4.1.2 Zernike Basis

Wavefront aberrations, in optical systems, have traditionally been modeled using the Zernike polynomials [3]. Zernike polynomials are ideal for circular apertures because they employ a polar coordinate system and are orthogonal on a continuous surface. However, both the DM and WFS are square grids. The problem with using a polar set on a sampled square grid is that as the radius decreases, the resolution of the angular dimension decreases. Also, as the angle changes, the resolution of the radius varies periodically every 90 degrees with maximum resolution on the x and y axis and minimum resolution on the lines x = ±y. For reference, the Zernike modes are defined as

$$\begin{aligned} Z_{even\ j} &= \sqrt{n+1}R_n^m(r)\sqrt{2}\cos m\theta \\ Z_{odd\ j} &= \sqrt{n+1}R_n^m(r)\sqrt{2}\sin m\theta \end{aligned} \Bigg\} \quad m \neq 0$$
$$Z_j = \sqrt{n+1}R_n^0(r) \qquad m = 0 \tag{4.1}$$

$$\text{where} \quad R_n^m(r) = \sum_{s=0}^{(n-m)/2} \frac{(-1)^s (n-s)!}{s![(n+m)/2-s]![(n-m)/2-s]!} r^{n-2s} \tag{4.2}$$

m and n are integers, $m \leq n$ and n - $|m|$ = even

j is the index of the particular Zernike mode

Orthogonality on a continuous surface does not imply orthogonality of the samples. To apply these modes to a grid, one must evaluate the Zernike modes for all grid points and then orthogonalize the data set. A method for this is QR decomposition [13].

4.1.3 Legendre Basis

An alternate approach is to use a polynomial set that is defined in Cartesian coordinates. One approach was given by Southwell [19]. This approach used the products of Legendre

polynomials and appropriate coefficients to make the set of polynomials orthogonal on the given grid. This approach did not provide an ordering of the modes or an indication of what shapes are usable on a given grid. A general form was not provided, but an example of one of these modes is given below. Equations (4.4) and (4.5) are different for almost every shape. Equations (4.6) and (4.7) are determined by the actuator geometry.

$$L_7(x,y) = n_7 F_7(x,y) \tag{4.3}$$

where $F_7(x,y) = \left(5y^2 - d_N\right)x$ (4.4)

$$n_7^2 = \frac{15}{3d_N^2 g_N - 5d_N^3} \tag{4.5}$$

$$g_N = 3\left(\frac{D}{2}\right)^2\left(1 - \frac{7}{3N^2}\right) \tag{4.6}$$

$$d_N = \left(\frac{D}{2}\right)^2\left(1 - \frac{1}{N^2}\right) \tag{4.7}$$

N^2 is the number of samples of a square grid.

D is the width of the square grid

This method provides an orthogonal set of modes defined on a grid directly, but the designer must manually solve the orthogonal conditions for all used modes.

4.1.4 Cartesian Basis

The methods discussed in section 4.1.2 and 4.1.3 are both complicated approaches to finding an orthogonal modal basis. Rather than using Legendre polynomials directly, each mode will be initially defined as

$$p_{m,n}(x,y) = x^m y^n \tag{4.8}$$

where m and n are non-negative integers

This can be displayed as a matrix of functions as in equation (4.9).

$$P_{MxN} = \begin{bmatrix} 1 & x & x^2 & \cdots & x^M \\ y & xy & x^2y & \cdots & x^My \\ y^2 & xy^2 & x^2y^2 & \cdots & x^My^2 \\ \vdots & \vdots & \vdots & \ddots & \vdots \\ y^N & xy^N & x^2y^N & \cdots & x^My^N \end{bmatrix} \tag{4.9}$$

where M and N are the maximum m and n of the set

Both the Legendre and Zernike approaches provide a 1D ordering of the modes. This method can be ordered according to a matrix location where $m + 1$ is the column and $n + 1$ is the row, as above. The maximum order (exponent) of each shape is $m + n$. Sets of equivalent order are on the diagonal lines perpendicular to the main diagonal. For example, the fourth order shapes are x^4, y^4, x^3y, xy^3 and x^2y^2. The process of making these shapes orthogonal is given in section 4.1.7.

4.1.5 Critical Sampling and Actuation

It is important to have an understanding of the minimum necessary samples required for such 2D polynomials and where those sample points must occur. First consider the problem of sampling a 1D polynomial of equation (4.10). The Vandermonde matrix can be formed to provide the M+1 equations necessary to solve for vector c for an order M 1D polynomial as in equation (4.11). This matrix is always invertible as long as the samples occur at unique points.

$$f(x) = \sum_{m=0}^{M} c_m x^m \tag{4.10}$$

$$\begin{bmatrix} f(x_0) \\ f(x_1) \\ \vdots \\ f(x_M) \end{bmatrix} = \begin{bmatrix} x_0^0 & x_0^1 & \cdots & x_0^M \\ x_1^0 & x_1^1 & \cdots & x_1^M \\ \vdots & \vdots & \ddots & \vdots \\ x_M^0 & x_M^1 & \cdots & x_M^M \end{bmatrix} \begin{bmatrix} c_0 \\ c_1 \\ \vdots \\ c_M \end{bmatrix} \tag{4.11}$$

A similar approach can be taken with the 2D case. For arbitrary M and N, the 2D polynomial can be defined as

$$f(x,y)=\sum_{m=0}^{M}\sum_{n=0}^{N}c_{m,n}x^{m}y^{n} \tag{4.12}$$

$$\begin{bmatrix} f(x_0,y_0) & f(x_0,y_1) & \cdots & f(x_0,y_N) & f(x_1,y_0) & f(x_1,y_1) & \cdots & f(x_1,y_N) \\ & & & \cdots & f(x_M,y_0) & f(x_M,y_1) & \cdots & f(x_M,y_N) \end{bmatrix}^T =$$

$$\begin{bmatrix} x_0^0\begin{Bmatrix} y_0^0 & y_0^1 & \cdots & y_0^N \\ y_1^0 & y_1^1 & \cdots & y_1^N \\ \vdots & \vdots & \ddots & \vdots \\ y_N^0 & y_N^1 & \cdots & y_N^N \end{Bmatrix} & x_0^1\begin{Bmatrix} y_0^0 & y_0^1 & \cdots & y_0^N \\ y_1^0 & y_1^1 & \cdots & y_1^N \\ \vdots & \vdots & \ddots & \vdots \\ y_N^0 & y_N^1 & \cdots & y_N^N \end{Bmatrix} & \cdots & x_0^M\begin{Bmatrix} y_0^0 & y_0^1 & \cdots & y_0^N \\ y_1^0 & y_1^1 & \cdots & y_1^N \\ \vdots & \vdots & \ddots & \vdots \\ y_N^0 & y_N^1 & \cdots & y_N^N \end{Bmatrix} \\ x_1^0\begin{Bmatrix} y_0^0 & y_0^1 & \cdots & y_0^N \\ y_1^0 & y_1^1 & \cdots & y_1^N \\ \vdots & \vdots & \ddots & \vdots \\ y_N^0 & y_N^1 & \cdots & y_N^N \end{Bmatrix} & x_1^1\begin{Bmatrix} y_0^0 & y_0^1 & \cdots & y_0^N \\ y_1^0 & y_1^1 & \cdots & y_1^N \\ \vdots & \vdots & \ddots & \vdots \\ y_N^0 & y_N^1 & \cdots & y_N^N \end{Bmatrix} & \cdots & x_1^M\begin{Bmatrix} y_0^0 & y_0^1 & \cdots & y_0^N \\ y_1^0 & y_1^1 & \cdots & y_1^N \\ \vdots & \vdots & \ddots & \vdots \\ y_N^0 & y_N^1 & \cdots & y_N^N \end{Bmatrix} \\ \vdots & \vdots & \ddots & \vdots \\ x_M^0\begin{Bmatrix} y_0^0 & y_0^1 & \cdots & y_0^N \\ y_1^0 & y_1^1 & \cdots & y_1^N \\ \vdots & \vdots & \ddots & \vdots \\ y_N^0 & y_N^1 & \cdots & y_N^N \end{Bmatrix} & x_M^1\begin{Bmatrix} y_0^0 & y_0^1 & \cdots & y_0^N \\ y_1^0 & y_1^1 & \cdots & y_1^N \\ \vdots & \vdots & \ddots & \vdots \\ y_N^0 & y_N^1 & \cdots & y_N^N \end{Bmatrix} & \cdots & x_M^M\begin{Bmatrix} y_0^0 & y_0^1 & \cdots & y_0^N \\ y_1^0 & y_1^1 & \cdots & y_1^N \\ \vdots & \vdots & \ddots & \vdots \\ y_N^0 & y_N^1 & \cdots & y_N^N \end{Bmatrix} \end{bmatrix} \begin{bmatrix} c_{0,0} \\ c_{0,1} \\ \vdots \\ c_{0,N} \\ c_{1,0} \\ c_{1,1} \\ \vdots \\ c_{1,N} \\ \vdots \\ c_{M,0} \\ c_{M,1} \\ \vdots \\ c_{M,N} \end{bmatrix}$$

(4.13)

A 2D matrix based on the Vandermonde approach can also be defined as in equation (4.13). Using the definition of the 1D Vandermonde matrix, the y-based sub-matrix block is linearly independent only if there are at least N+1 unique sample points in the y direction. If this is minimally satisfied, this sub-matrix is an invertible square matrix of size $(N+1)^2$. Likewise, these sub-matrices are only linearly independent of each other if the x-based coefficients are linearly independent of each other. This requires M+1 unique samples in the x direction. This means there will be (M+1) by (M+1) sub-matrices to build the matrix of equation (4.13). This matrix is size $(MN+M+N+1)^2$. Using a sample

grid of size (M+1)x(N+1) provides the appropriate and necessary (MN+M+N+1) unique samples to make the 2D Vandermonde-type matrix invertible. An example is shown as equation 4.14 for $M = 2$ and $N = 1$.

$$\begin{bmatrix} f(x_0,y_0) \\ f(x_0,y_1) \\ f(x_1,y_0) \\ f(x_1,y_1) \\ f(x_2,y_0) \\ f(x_2,y_1) \end{bmatrix} = \begin{bmatrix} 1\begin{Bmatrix}1 & y_0\\ 1 & y_1\end{Bmatrix} & x_0\begin{Bmatrix}1 & y_0\\ 1 & y_1\end{Bmatrix} & x_0^2\begin{Bmatrix}1 & y_0\\ 1 & y_1\end{Bmatrix} \\ 1\begin{Bmatrix}1 & y_0\\ 1 & y_1\end{Bmatrix} & x_1\begin{Bmatrix}1 & y_0\\ 1 & y_1\end{Bmatrix} & x_1^2\begin{Bmatrix}1 & y_0\\ 1 & y_1\end{Bmatrix} \\ 1\begin{Bmatrix}1 & y_0\\ 1 & y_1\end{Bmatrix} & x_2\begin{Bmatrix}1 & y_0\\ 1 & y_1\end{Bmatrix} & x_2^2\begin{Bmatrix}1 & y_0\\ 1 & y_1\end{Bmatrix} \end{bmatrix} \begin{bmatrix} c_{0,0} \\ c_{0,1} \\ c_{1,0} \\ c_{1,1} \\ c_{2,0} \\ c_{2,1} \end{bmatrix} \tag{4.14}$$

4.1.6 Modal Sensing

Piston represents the first Zernike mode and is the average actuator position. Piston is invisible to the WFS because its gradient is 0 regardless of its magnitude. Hence, the implemented system must control the piston in open loop and it is measured from the control signals rather than the mirror shape. This also complicates the issue of critical sampling, but can be solved by expanding on the method given in section 4.1.5. For a given M and N, the gradient of the function is

$$\nabla f(x,y) = \begin{bmatrix} \sum_{m=1}^{M}\sum_{n=0}^{N} mc_{m,n}x^{m-1}y^{n} \\ \sum_{m=0}^{M}\sum_{n=1}^{N} nc_{m,n}x^{m}y^{n-1} \end{bmatrix} \tag{4.15}$$

This implies that the sensor needs to provide x-direction slope data on a grid of size Mx(N+1) and y-direction slope data on a grid of size (M+1)xN to solve each of the two polynomials in equation (4.15) independently. If these are combined into an over-determined 2D Vandermonde-type matrix, the coefficients can be solved in the least squares sense.

If each sample point provides both the x and y slope (as in the case of this sensor) these grids can be overlapped and the sample grid becomes $(M+1)$x$(N+1)$ minus one of the corners. Since the average elevation is not detectable, this still has one sample point for each $x^m y^n$ of the set. For simplicity, it can be stated that for a given set of shapes defined by maximum powers M and N, $(M+1)$x$(N+1)$ sample points provide sufficient data to determine the polynomial coefficients provided that the sensor is a magnitude or slope sensor.

4.1.7 Modal Set Selection and Orthogonalization

For the implemented system, the wave front sensor has 9x9 sensor points. The deformable mirror has 10x10 distinct actuators. It is obvious from the preceding discussion that the modal set can be defined with $M = 9$ and $N = 9$. Any shape outside of this set would likely cause aliasing in the sensor, so they are avoided.

In order to make the system behave as though each shape is independently controlled, the shapes must be orthogonal. Each of the shapes defined in equation (4.9) provides a unique shape (given sufficient grid points) but are not orthogonal to each other. The steps to obtain the required orthogonal basis are as follows. This is accompanied by a small example of a 3x3 grid with 4 shapes.

1. Normalize the range of the grid to -1 to 1.

$$x = \begin{bmatrix} -1 & 0 & 1 \\ -1 & 0 & 1 \\ -1 & 0 & 1 \end{bmatrix} \qquad y = \begin{bmatrix} 1 & 1 & 1 \\ 0 & 0 & 0 \\ -1 & -1 & -1 \end{bmatrix}$$

2. Select the shapes required from equation (4.9)

$$p_{0,0} = 1 \qquad p_{1,0} = x \qquad p_{0,1} = y \qquad p_{1,1} = xy$$

3. Evaluate each of these shapes on the normalized grid.

$$p_{0,0}(x,y)=\begin{bmatrix}1 & 1 & 1\\ 1 & 1 & 1\\ 1 & 1 & 1\end{bmatrix} \qquad p_{1,0}(x,y)=\begin{bmatrix}-1 & 0 & 1\\ -1 & 0 & 1\\ -1 & 0 & 1\end{bmatrix}$$

$$p_{0,1}(x,y)=\begin{bmatrix}1 & 1 & 1\\ 0 & 0 & 0\\ -1 & -1 & -1\end{bmatrix} \qquad p_{1,1}(x,y)=\begin{bmatrix}-1 & 0 & 1\\ 0 & 0 & 0\\ 1 & 0 & -1\end{bmatrix}$$

4. Determine a linear ordering for the shapes based on increasing sum of powers, including 0 for x^0y^0. The order chosen is 1, x, y, xy.

5. Represent each shape as a column vector. Build a matrix by placing the column vectors in the order determined in step 4.

$$A=\begin{bmatrix}1 & -1 & 1 & -1\\ 1 & -1 & 0 & 0\\ 1 & -1 & -1 & 1\\ 1 & 0 & 1 & 0\\ 1 & 0 & 0 & 0\\ 1 & 0 & -1 & 0\\ 1 & 1 & 1 & 1\\ 1 & 1 & 0 & 0\\ 1 & 1 & -1 & -1\end{bmatrix}$$

6. Use QR Decomposition to obtain an orthogonal matrix from the one built in step 5. The orthogonal Q matrix later becomes the modal matrix. The R matrix is discarded.

$$QR = A$$

$$Q = \begin{bmatrix} 0.333 & -0.4082 & 0.4082 & -0.5 \\ 0.333 & -0.4082 & 0 & 0 \\ 0.333 & -0.4082 & -0.4082 & 0.5 \\ 0.333 & 0 & 0.4082 & 0 \\ 0.333 & 0 & 0 & 0 \\ 0.333 & 0 & -0.4082 & 0 \\ 0.333 & 0.4082 & 0.4082 & 0.5 \\ 0.333 & 0.4082 & 0 & 0 \\ 0.333 & 0.4082 & -0.4082 & -0.5 \end{bmatrix}$$

7. Remove the first column vector from Q to remove x^0y^0 from the set. Removal at this point ensures that the set is also orthogonal to the invisible x^0y^0 shape.

$$\begin{bmatrix} Modal \\ Matrix \end{bmatrix} = \begin{bmatrix} -0.4082 & 0.4082 & -0.5 \\ -0.4082 & 0 & 0 \\ -0.4082 & -0.4082 & 0.5 \\ 0 & 0.4082 & 0 \\ 0 & 0 & 0 \\ 0 & -0.4082 & 0 \\ 0.4082 & 0.4082 & 0.5 \\ 0.4082 & 0 & 0 \\ 0.4082 & -0.4082 & -0.5 \end{bmatrix}$$

The following figure is a representation of the result of this method for P_{6x6} for a 12x12 grid. Piston is in the left corner and the three modes that surround it are *x*, *y* and *xy*.

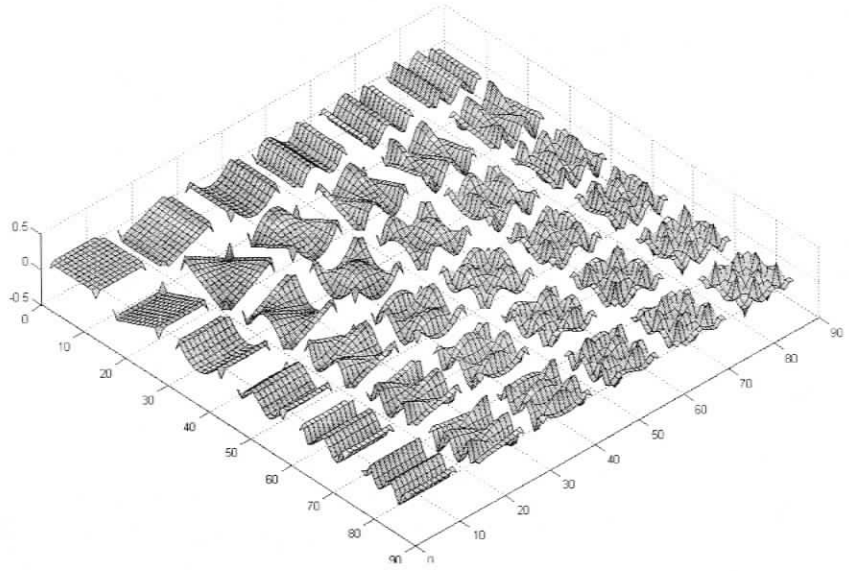

Figure 4.2: Representation of the Orthogonalized P_{6x6} set on 12x12 grids with corners set to zero

4.1.8 Actuator and Sensor Interaction

This system could not be controlled without an accurate measurement of how changes to the DM shape affect the WFS output. This calibration is done by actuating the DM in open loop and recording the steady state change of the WFS. The measurements of the interaction are combined into an interaction matrix. Each pair of rows are the x and y displacements of the centroid under a given lenslet of the WFS. Each column represents a mode that is used. So this interaction matrix can be multiplied by a vector of modal magnitudes and the result is a model of what the sensor would see. This is also explained in [5].

$$\begin{bmatrix} Interaction \\ Matrix \end{bmatrix} = \begin{bmatrix} WFS\ Change\ Caused \\ By\ DM\ Change \end{bmatrix} \begin{bmatrix} Modal \\ Matrix \end{bmatrix} \tag{4.16}$$

The changes of the WFS spot positions to DM changes are represented by a matrix in equation (4.16), but are actually properties of the optical system and not a mathematical operator. The modal matrix is determined in step 7 of section 4.1.7. Each column of the interaction matrix corresponds to how a given DM mode affects the WFS.

The pseudo-inverse of the interaction matrix is called the reconstructor matrix and has a very useful application. If the vector of sensor error measurements is multiplied into the reconstructor matrix, the result is a vector that is the magnitude of error in the modes. The reconstructor matrix can be considered as essentially a part of the WFS sensor and configures the sensor to sense the chosen set of modes. The pseudo-inverse is found with the Singular Value Decomposition as described in [13].

$$U\Sigma V^T = \begin{bmatrix} Interaction \\ Matrix \end{bmatrix} \tag{4.17}$$

$$\begin{bmatrix} Reconstructor \\ Matrix \end{bmatrix} = V\Sigma^{+}U^T \tag{4.18}$$

$$\begin{bmatrix} Modal \\ Error \\ Vector \end{bmatrix} = \begin{bmatrix} Reconstructor \\ Matrix \end{bmatrix} \begin{bmatrix} WFS \\ Error \\ Vector \end{bmatrix} \tag{4.19}$$

4.2 One Dimensional Modal Controller Implementation

The WFS error is converted into orthogonal modal error by an appropriate reconstructor matrix as discussed in the previous section. The DM output is a linear combination of orthogonal actuator shapes (modes). Therefore, the controller can be approached as a 1D controller applied to each of these modes in parallel. The output of each of these controllers is converted to actuator space via the orthogonal basis for the DM output and summed.

4.2.1 Controller Output Quantization

An important source of errors in the implementation of a digital controller is quantization error. Because of quantization, the implemented system is a nonlinear system. For the controllers considered here for implementation, the quantization errors due to mathematical operations inside the computer can be neglected due to the use of floating point arithmetic with several significant digits. However, the quantization error due to D/A conversion at the DM is significant.

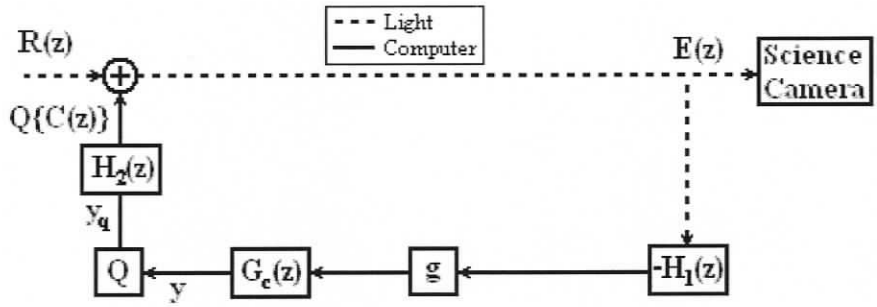

Figure 4.3: Implementation of controller that is ignorant of output quantization

One way to interpret this output quantization is that it makes the system partially open loop because it stops part of the signal. Figure 4.3 shows a controller implementation without compensation for output quantization. The WFS, Ref and R components of Figure 4.1 have been simplified to $-H_1(z)$ for this discussion. The D/A

and DM are combined as $H_2(z)$. $G_c(z)$ is any of the linear controllers designed in Chapter 3 and is shown with a quantizer, Q, on the controller's output.

$$Q\{y\} = y_q = y + y_r \tag{4.20}$$

where Q{ } is the quantization operator

y is the ideal controller output

y_q is the quantized controller output

y_r is the residual error of quantization

Controllers are often designed to be stable when y is the controller output, not y_q. The small signal that is discarded, y_r, is effectively in open loop and the portion of the signal that is retained by the quantization, y_q, is in closed loop. If the open loop system from y_q to y in Figure 4.3 is not stable, y will proceed toward ±infinity. In the closed loop system, y is bounded because it changes enough to change the quantization decision. This may generate oscillations between quantization levels as in Figure 4.4. Therefore, it is desirable to have a controller with a stable transfer function that also leads to a stable closed loop system.

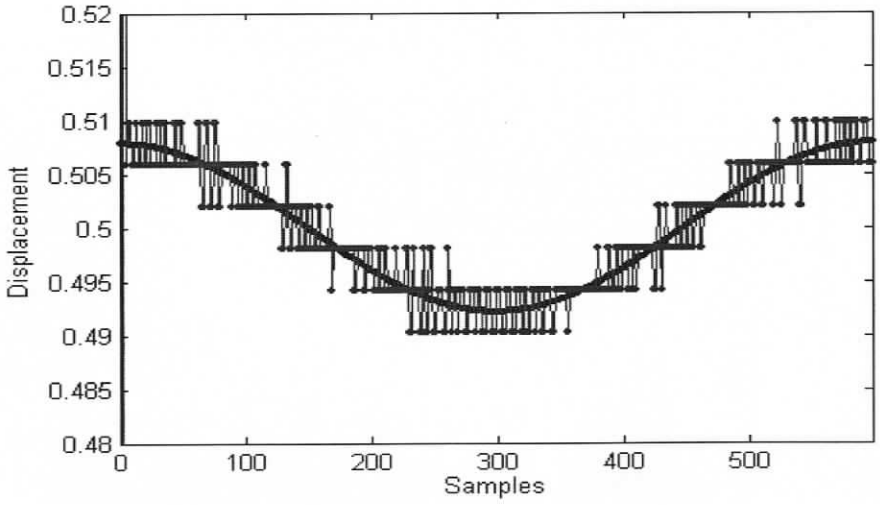

Figure 4.4: Simulation of a Type 2 system following a small input signal without residual error feedback

4.2.2 Residual Error Feedback

The problem of implementing digital filters/controllers in the presence of quantization has been extensively considered in the literature. One of the techniques leading to good performance is residual state feedback as shown in [14]. Another technique is the optimization of the state-space controller that minimizes the round off noise gain [16]. A third approach is to create a new domain space that is an augmentation of the discrete Z-domain to a new ρ-domain [15]. These approaches are overly complicated for this system because they are for large numbers of quantization points, particularly when the mathematical operations internal to the controller are significantly quantized.

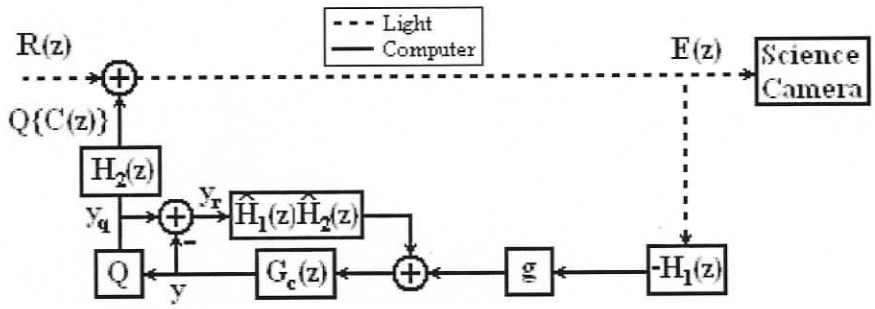

Figure 4.5: Internal feedback of the residual signal, y_r

In this implementation, there is only one point where there is significant finite word length in quantization. This point is the quantization step within the computer where the desired actuator position is transformed into an 8-bit signal prior to D/A conversion. The D/A converter decodes the 8-bit signal into the voltage that will be applied to each DM actuator. All other calculations are conducted in floating point arithmetic, which has 7 significant digits. The quantized output signal is a known signal because it is generated within the computer at the quantization step. The WFS quantization should be small enough to not significantly change the noise generated at the controller output and is ignored for this design. The following presents a method of

retaining the residual error of the output to reduce output jitter that is due to the quantization noise and is shown in Figure 4.5.

The approach to improve this system is to feedback the residual error, y_r, through the model of the external feedback path, $\hat{H}_1(z)\hat{H}_2(z)$, and feed it back to the controller input. This can be done by taking the residual error as the difference between the quantized output, y_q and the desired controller output, y and feeding the result through $\hat{H}_1(z)\hat{H}_2(z)$. Ideally, this will have the effect that the input to the controller, $G_c(z)$, will be the same as if quantization did not occur and the implemented system will behave close to the linear model without quantization. This stable performance is important for two reasons: (i) it removes the constant jitter between quantization levels of Figure 4.4 as shown in Figure 4.8 and (ii) the controller will continue to track the input even if a supervisory program imposes additional limits on the output signal, such as the boundaries of actuator stroke.

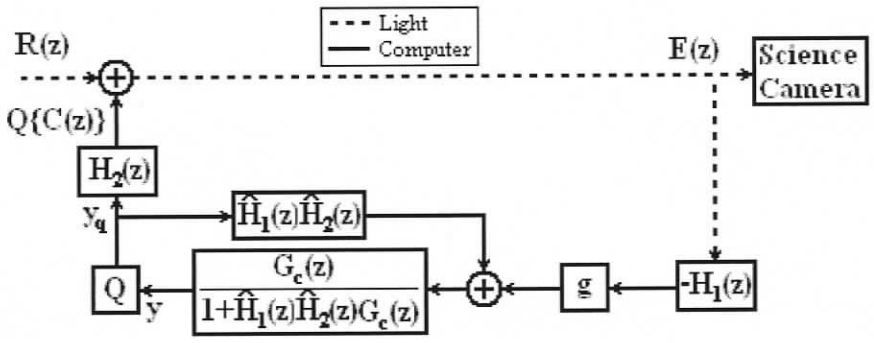

Figure 4.6: Alternate stable implementation of the $G_1(z)$ controller

From Figure 4.5, the block diagram can be modified so that an equivalent controller structure is obtained as given in Figure 4.6. The negative feedback loop of y through $\hat{H}_1(z)\hat{H}_2(z)$ to the controller input shown in Figure 4.5 can also be represented

by $\frac{G_c(z)}{1+\hat{H}_1(z)\hat{H}_2(z)G_c(z)}$. Therefore, if Q is removed and left in an open state, y will remain bounded for the given system as shown by the resulting transfer function of equation (4.21). This open loop system is also shown in Figure 4.7.

$$\frac{Y(z)}{R(z)} = -\frac{gH_1(z)G_c(z)}{1+\hat{H}_1(z)\hat{H}_2(z)G_c(z)} \tag{4.21}$$

If the system is closed by shorting y and y_q together, then y is also stable and behaves as

$$\frac{Y(z)}{R(z)} = -\frac{H_1(z)G_c(z)}{1+\hat{H}_1(z)\hat{H}_2(z)G_c(z)-\hat{H}_1(z)\hat{H}_2(z)G_c(z)+gH_1(z)H_2(z)G_c(z)} \tag{4.22}$$

$$\frac{Y(z)}{R(z)} = -\frac{gH_1(z)G_c(z)}{1+gH_1(z)H_2(z)G_c(z)} \tag{4.23}$$

It is left to the designer of the controller whether Figure 4.5 or 4.6 would be used. The Type 1 and Type 2 controllers were implemented as in Figure 4.6. In these cases, the form of Figure 4.6 was simpler than Figure 4.5 because the closed loop poles are at z = 0. Therefore, the transfer function $\frac{G_c(z)}{1+\hat{H}_1(z)\hat{H}_2(z)G_c(z)}$ can be implemented as an FIR filter. These are shown in Figures 4.11 and 4.12. $G_c(z)$ can be replaced by either of the controllers given in equations (3.38) and (3.39). The CAO controller of equation (3.37) was implemented as Figure 4.9 with out the compensation for quantization discussed in this section.

For a system to truly be stable with quantization, it must find an equilibrium point when the quantizer output is held to a constant level that is either due to the quantization or an override by a supervisory program that is not part of the linear controller. In this system, an override can occur when the controller output has crossed the boundary of

available actuator stroke and the signal must be clipped to one of the extremes. The resulting open loop system, shown in Figure 4.7, will be bounded if the controlled system, $H_1(z)H_2(z)$, its model, $\hat{H}_1(z)\hat{H}_2(z)$, and $\dfrac{G_c(z)}{1+\hat{H}_1(z)\hat{H}_2(z)G_c(z)}$ are stable. Cancellation of $y_q(k)$ by perfectly matching the model to the actual plant is not necessary.

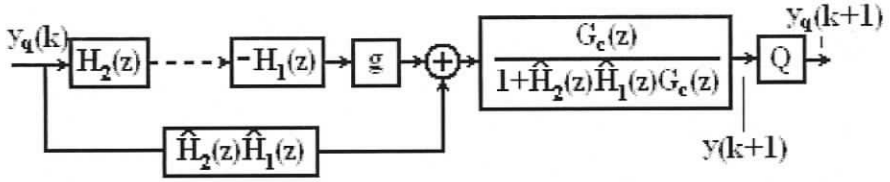

Figure 4.7: System opened at the point of quantization

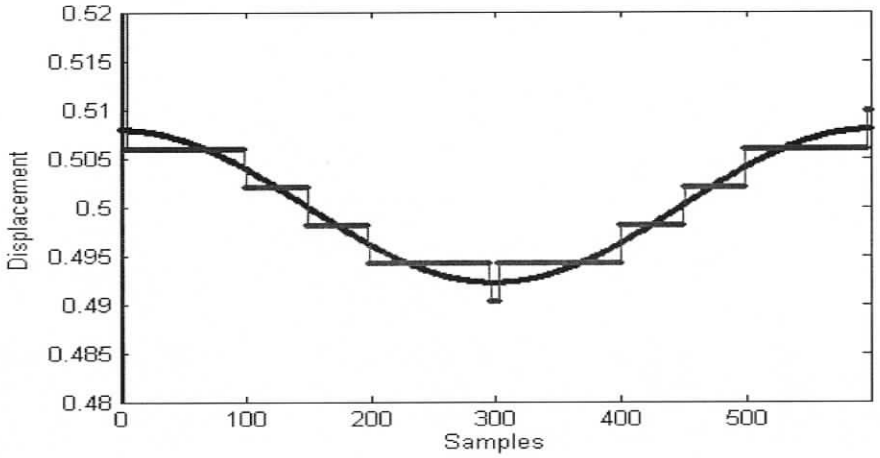

Figure 4.8: Simulation of a Type 2 system stably following a small input signal with residual error feedback

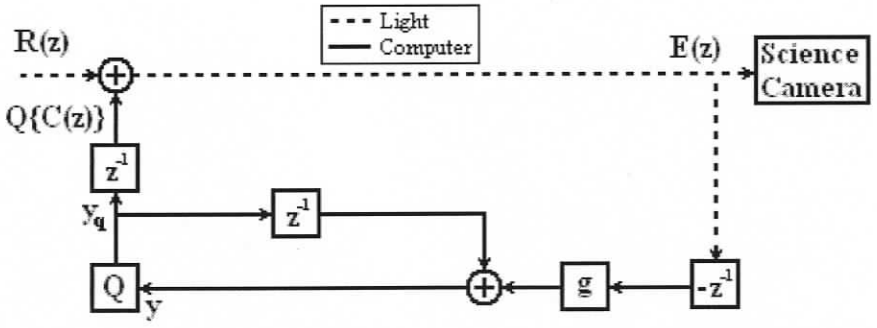

Figure 4.9: Implementation of a CAO controller, equation (3.37)

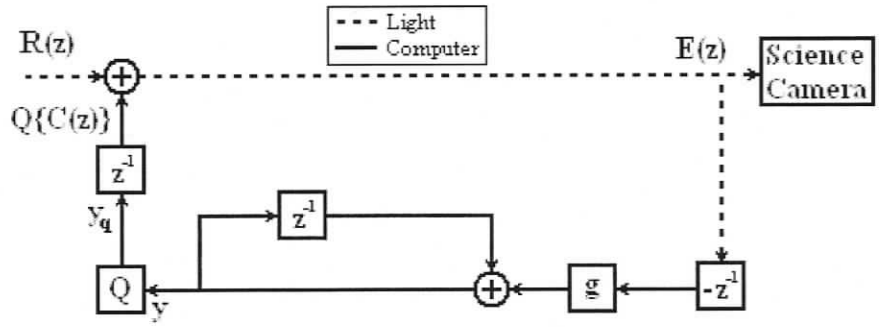

Figure 4.10: Alternate implementation of a CAO controller, equation (3.37)

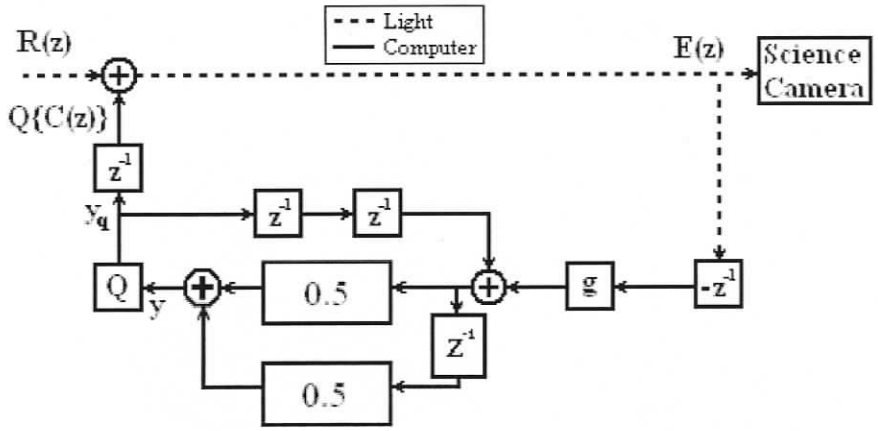

Figure 4.11: Implementation of a Type 1 controller, equation (3.38)

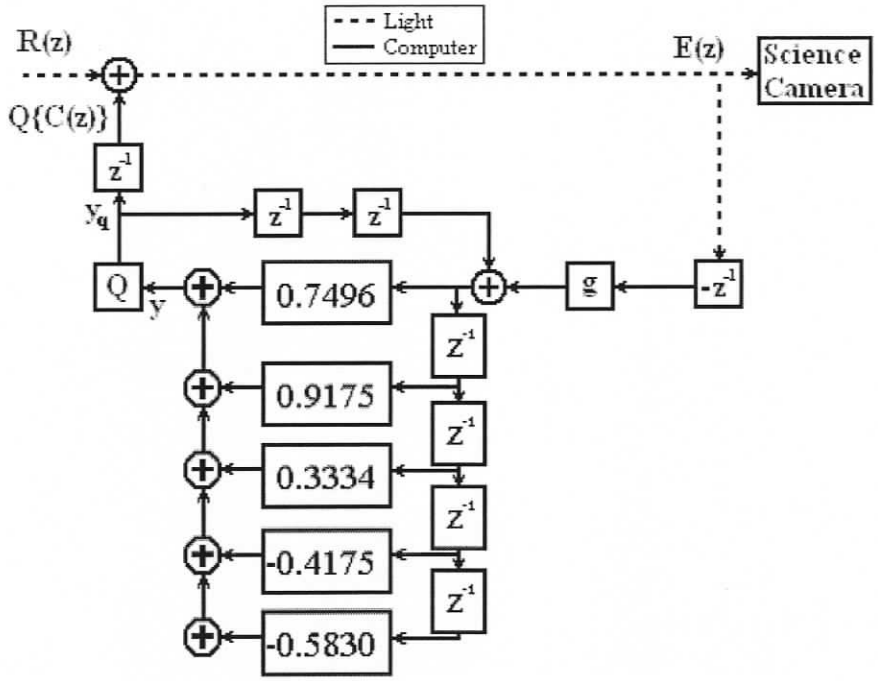

Figure 4.12: Implementation of a Type 2 controller, equation (3.39)

The entire system is shown in Figure 4.13. The WFS provides a measurement vector with W elements which is multiplied by the reconstructor matrix, R, to obtain the error for all the orthogonal modes. The reconstructor sends the two signals associated to tilt to the two 1D controllers that control the TT. It passes the M number of modal errors to the M 1D controllers that control the DM. The output of the controllers are converted to actuator space by multiplying by the "Mode to Actuator" matrix. This matrix is the orthogonal actuator basis matrix developed in section 4.1.7. The desired piston and flat state are added before the quantization step to properly bias the signals. The piston keeps the mirror actuated to mid stroke. The flat state can be used as the starting point for the controller for testing purposes. This bias is removed before conversion back to modal space. The actuators are converted back to modes by multiplying the quantized actuator signals by the transpose of the "Mode to Actuator" matrix. This result is the quantized modes that will appear on the DM.

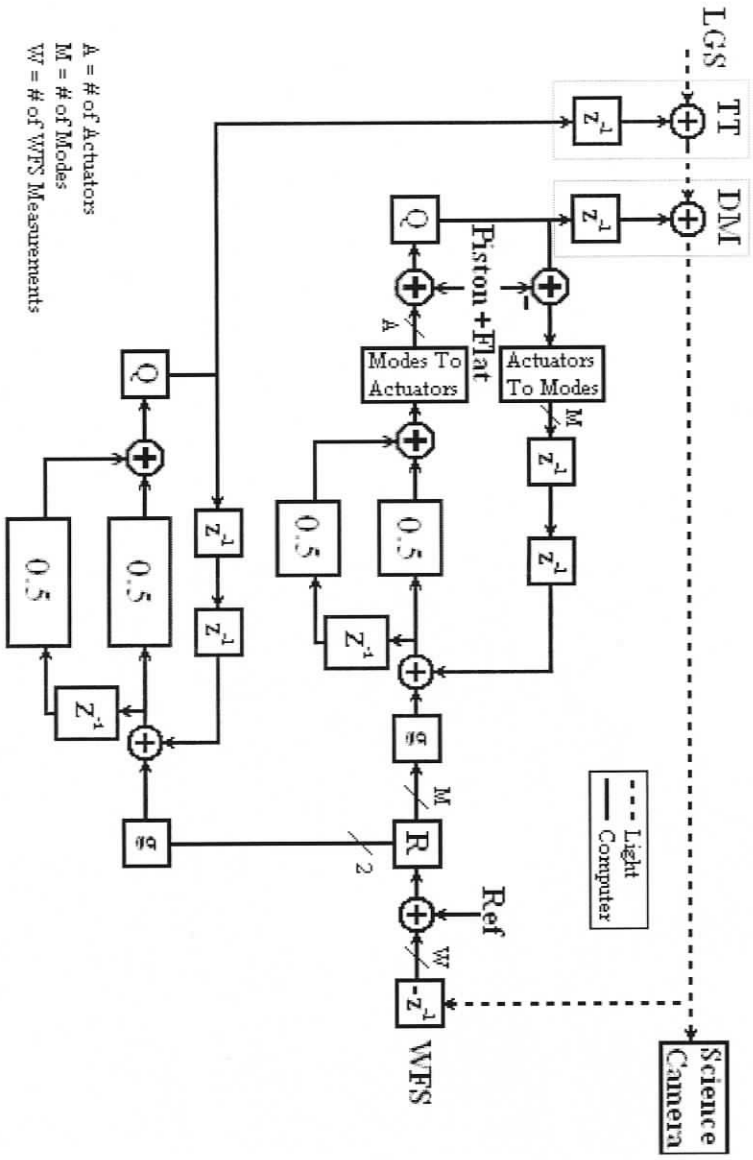

Figure 4.13: Control diagram of complete system using Type 1 control of the TT and DM

4.2.3 Output Noise Amplification

An aspect of the CAO system that has been ignored in the literature is the amplification of the output quantization noise. Both implementation methods of CAO systems shown in the previous section cause this noise source to be amplified. Ideally, the Type 1 and Type 2 controllers do not amplify the output quantization noise due to the residual error feedback implementation.

If the system shown in Figure 4.9 is used, it can be re-oriented to show the residual quantization error, y_r, as the system input as shown in Figure 4.14. For this analysis, $y_r(k)$ is considered to be an independent noise source. Equation (4.24) shows the signals that are added together to form the current quantized output, $y_q(k)$. The error term is expanded in equation (4.25) into the combination of the atmospheric turbulence, denoted by r, and y_q. Equation (4.26) shows the Z-transform of equation (4.25).

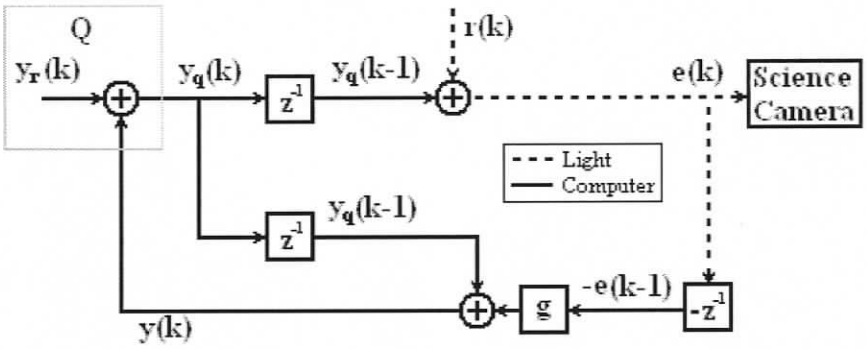

Figure 4.14: Re-orientation of Figure 4.9 (CAO) with y_r as the system input

$$y_q(k) = y_r(k) + y_q(k-1) - ge(k-1) \tag{4.24}$$

$$y_q(k) = y_r(k) + y_q(k-1) - g[y_q(k-2) + r(k-1)] \tag{4.25}$$

$$Y_q(z) = Y_r(z) + z^{-1}Y_q - gz^{-2}Y_q(z) - gz^{-1}R(z) \tag{4.26}$$

$$\frac{Y_q(z)}{Y_r(z)} = \left(\frac{1}{1 - z^{-1} + gz^{-2}}\right)\left(1 - gz^{-1}\frac{R(z)}{Y_r(z)}\right) \tag{4.27}$$

The literal meaning of $\frac{R(z)}{Y_r(z)}$ is the impact that the residual error of the DM shape has on the turbulence of the atmosphere. Therefore, this term can certainly be equated to 0. Then, the effect of the residual quantization error on the science image can be given as

$$\frac{E(z)}{Y_r(z)} = \frac{z^{-1}}{1 - z^{-1} + gz^{-2}} \tag{4.28}$$

since $E(z) = z^{-1}Y_q(z) + R(z)$ and $\frac{R(z)}{Y_r(z)} = 0$

This spectrum would be 0dB if the quantization noise had no impact. The amplitude response of equation (4.28) is equal to the amplitude response of T_{CAO}(z) (see equation (2.15) and Figure 2.2 (left)) divided by g. This is a low pass filter, but at a gain of 0.25 has a peak amplification of 4. The benefit of this method is that it is stable if the output is clipped.

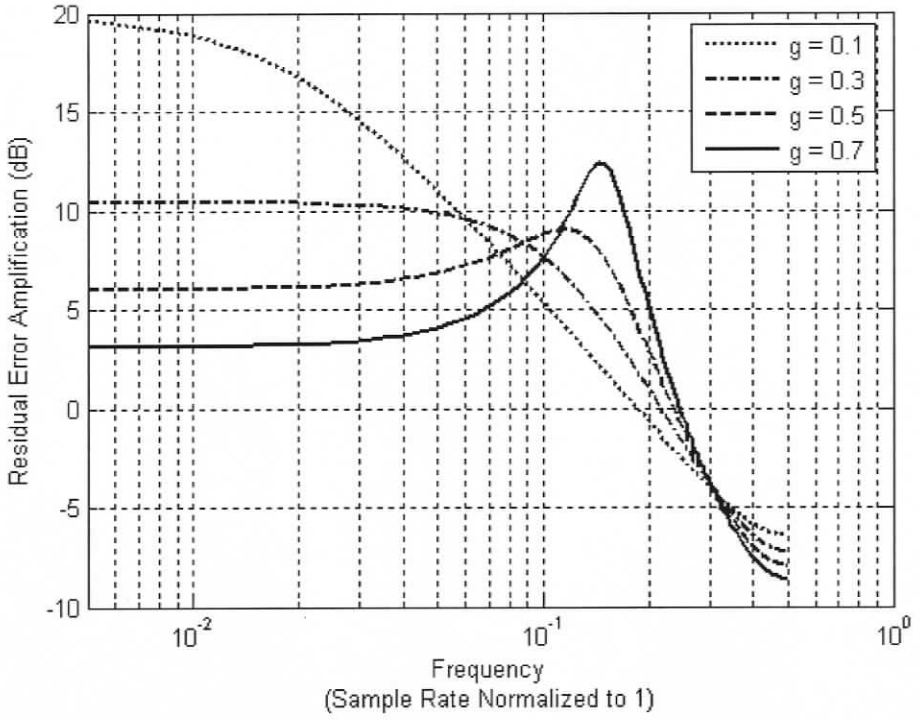

Figure 4.15: Residual error amplification of the CAO implementation of Figure 4.9

A similar treatment is given for the implementation of a CAO system as Figure 4.10. It has been re-oriented to show the residual quantization error as the input and given as Figure 4.16. This method does not handle clipping conditions well but has less amplification of the residual quantization error. Equation (4.29) is different from equation (4.25) by using $y(k\text{-}1)$ instead of $y_q(k\text{-}1)$. To make this a function involving y_q and y_r terms only, y is replaced by $y_q - y_r$ in equation (4.30). Equation (4.31) is the Z transform of the signals, and equation (4.32) is a simple algebraic manipulation to obtain the transfer function.

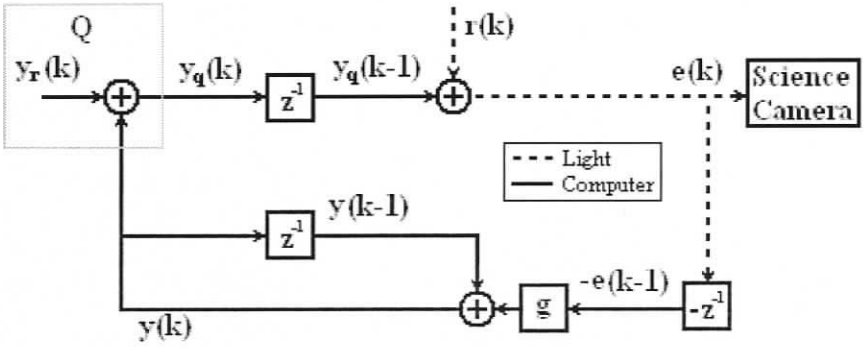

Figure 4.16: Re-orientation of Figure 4.10 (CAO) with y_r as the system input

$$y_q(k) = y_r(k) + y(k-1) - ge(k-1) \tag{4.29}$$

$$y_q(k) = y_r(k) + y_q(k-1) - y_r(k-1) - g[y_q(k-2) + r(k-1)] \tag{4.30}$$

$$Y_q(z) = Y_r(z) + z^{-1}Y_q(z) - z^{-1}Y_r(z) - gz^{-2}Y_q(z) - gz^{-1}R(z) \tag{4.31}$$

$$\frac{Y_q(z)}{Y_r(z)} = \left(\frac{1-z^{-1}}{1-z^{-1}+gz^{-2}}\right)\left(1 - gz^{-1}\frac{R(z)}{Y_r(z)}\right) \tag{4.32}$$

$$\frac{E(z)}{Y_r(z)} = \frac{z^{-1}-z^{-2}}{1-z^{-1}+gz^{-2}} \tag{4.33}$$

since $\quad E(z) = z^{-1}Y_q(z) + R(z)$ and $\dfrac{R(z)}{Y_r(z)} = 0$

Equation (4.33) is similar to the formula for the error transfer function for turbulence input but with an additional delay. The delay does not change the amplitude response, so it will have the same amplitude response as the rejection ratio as shown in Figure 4.17 (see the right side of Figure 2.2). This is essentially a high pass filter, so the assumption that high frequency noise is suppressed in CAO systems is false for this implementation scheme.

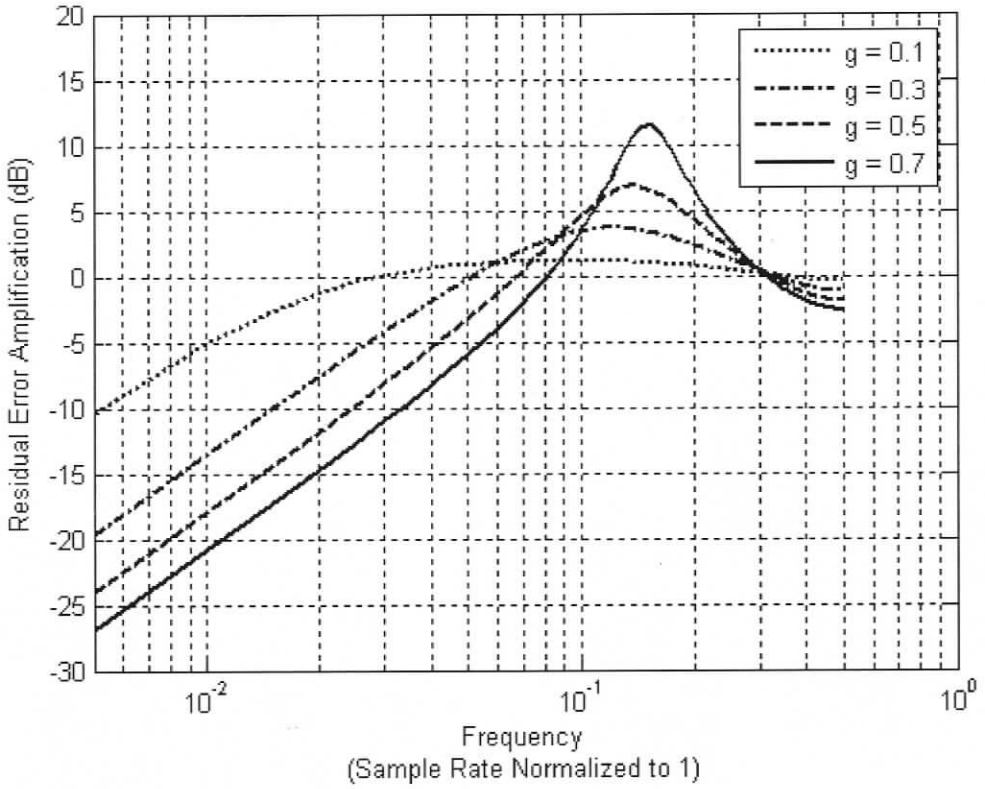

Figure 4.17: Residual error amplification of the CAO implementation of Figure 4.10

To obtain the best of both of these standard implementations, the system should be implemented as Figure 4.10 to have the least amplification of the quantization noise. Clipping of the output signals to bound the output within the available stroke of the DM should be implemented as Figure 4.9 to avoid signal run away during this open loop condition. However, neither of these approaches are the best implementation to limit the effect of quantization noise.

The effect of the residual quantization error on the Type 1 system implementation of Figure 4.11 is now considered. The re-oriented system is shown in Figure 4.18. The feedback of the residual error into the controller causes the controller to not react to the quantization noise that is contained in the measurement of $e(k)$. For simplicity of the equations, super position will be applied and $r(k)$ can be ignored.

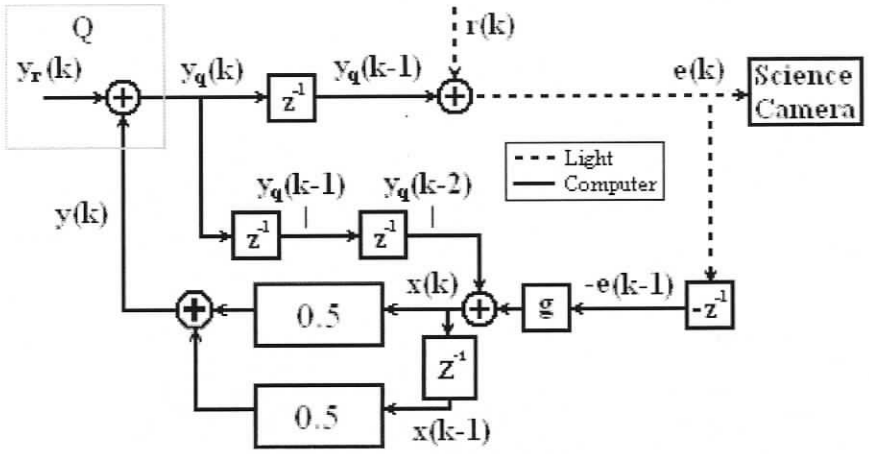

Figure 4.18: Re-orientation of Figure 4.11 (Type 1) with y_r as the system input

$$x(k) = y_q(k-2) - ge(k-1) \tag{4.34}$$

$$x(k) = y_q(k-2) - gy_q(k-2) = (1-g)y_q(k-2) \tag{4.35}$$

$$y_q(k) = y_r(k) + 0.5\big(x(k) + x(k-1)\big) \tag{4.36}$$

$$y_q(k) = y_r(k) + 0.5(1-g)\big(y_q(k-2) + y_q(k-3)\big) \tag{4.37}$$

$$Y_q(z) = Y_r(z) + 0.5(1-g)\big(z^{-2}Y_q(z) + z^{-3}Y_q(z)\big) \tag{4.38}$$

$$\frac{Y_q(z)}{Y_r(z)} = \frac{1}{1-0.5(1-g)\big(z^{-2}+z^{-3}\big)} \tag{4.39}$$

$$\frac{E(z)}{Y_r(z)} = \frac{z^{-1}}{1-0.5(1-g)\big(z^{-2}+z^{-3}\big)} \tag{4.40}$$

The gain for this system will normally be 1, which gives an amplitude response for equation (4.40) of 1 (0dB) for all frequencies. This means that the quantization noise will reach the science camera (unavoidable) and the controller does not react to it. To show that matching of the external path to the model is not necessary for the residual feedback implementation, several gains have been used in the range of ±15% as shown in Figure 4.19. Even with a gain mismatch of 15%, the peak noise gain is approximately 1.25 (2dB). The scale of this figure is equal to Figure 4.15 for ease of comparison.

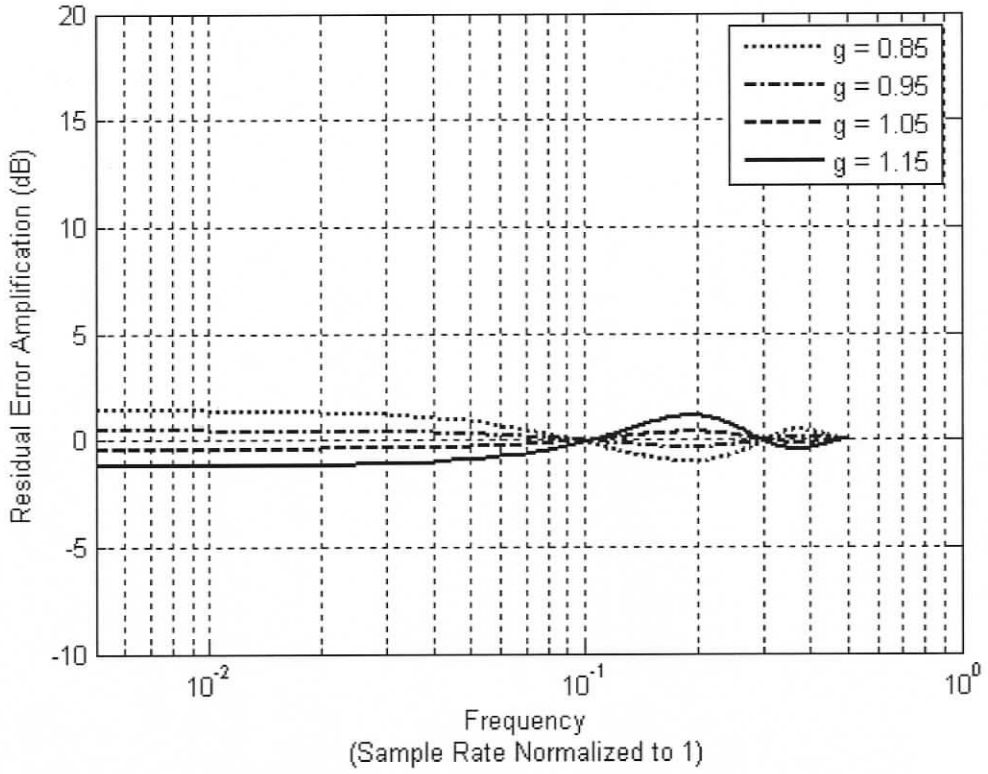

Figure 4.19: Residual error amplification of the Type 1 implementation of Figure 4.11

A similar transfer function can be found for the Type 2 system. The result is

$$\frac{E(z)}{Y_r(z)} = \frac{z^{-1}}{1-(1-g)\left(0.7496z^{-2}+0.9174z^{-3}+0.3333z^{-4}-0.4175z^{-5}-0.5829z^{-6}\right)} \qquad (4.41)$$

The ideal case is when g = 1 and the resulting amplification is 0dB. Like the Type 1 case, the amplification of residual error has been plotted for 4 gain levels in a range of

±15%. The Type 2 system is more reactive to noise than the Type 1, so it is natural that it does not perform as well when there is a gain mismatch. However, it is also generating less noise than the CAO systems.

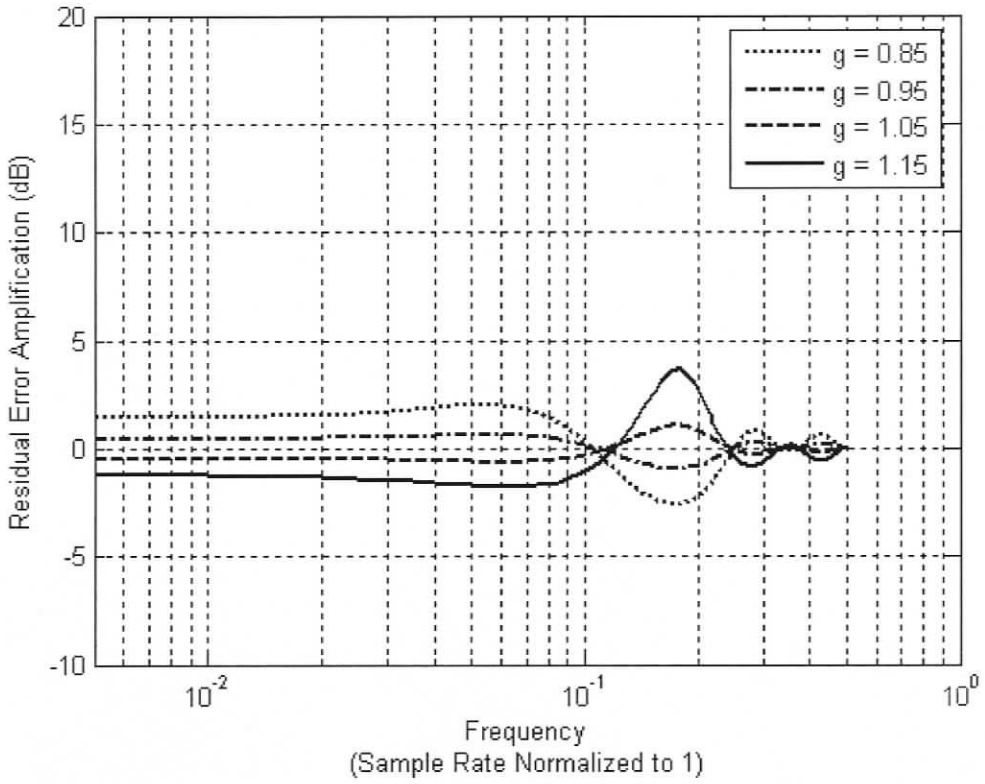

Figure 4.20: Residual error amplification of the Type 2 implementation of Figure 4.12

4.3 Conclusions

When the output signal is quantized, oscillations between quantization steps can occur in direct implementations of the controller transfer function. The system stability can be improved by feeding back the residual error through a model of the controlled system. This will be stable as long as the systems of Figures 4.5 and 4.7 are stable.

The CAO system amplifies the output quantization noise. The output quantization should be larger than the quantization in the WFS so this amplification should create the largest noise source in CAO systems.

The Type 1 and Type 2 systems are shown as Figures 4.11 and 4.12 respectively. Both systems use the quantized signal as the only source in the internal controller feedback. This makes both systems stable to the quantization noise and ideally they do not amplify the output quantization noise. Such implementations allow for tracking of the input when the y_q signal is in an override state because the stability is independent of the chosen value of y_q.

The Zernike set of modes is both complicated and not applicable to square grids at high spatial frequencies. The Legendre modes suggested by Southwell is a complicated method to obtain a set of modes that are Cartesian based and orthogonal. Finding the coefficients of multiples of 1-D Legendre modes to develop an orthogonal set of 2-D modes is unnecessary. This is because any orthogonalization process will automatically adjust the initial set of shapes to be orthogonal. The use of $x^m y^n$ as the initial shapes followed by an orthogonalization algorithm is a simple solution to obtaining a set of modes that are suited for a rectangular grid. For a set of shapes with the highest order polynomial equal to $x^M y^N$, an appropriate set of sample points is an $(M+1)$x$(N+1)$ grid.

Chapter 5

Experimental Results

This chapter describes the experimental verification of the control systems.

5.1 Procedure

The experimental test bed was operated with the following conditions:

1. The turbulence generator was operational with a temperature difference of approximately 30 ^{o}C and power supply for the fans was set at 5 volts.
2. Gain was set for critical damping of the three models, see Table 3.1.
3. The modal error was found by multiplying the WFS error with the modal reconstructor matrix that was determined in section 4.1.8. The modal error and the modal control signals were recorded for 11000 samples (approx. 42 seconds)

The discrete Fourier transform, $F\{\ \}$, was used to obtain the power spectrums of these signals. Every 11 samples of the amplitude of the resulting power spectrum were averaged to find a representative amplitude for each 0.25 Hz. The input turbulence modal magnitudes were taken as the output modal magnitudes plus the measured modal error as in equation (5.1). The time offset is due to the two sample delays for the output to become part of the error measurement. The method of determining the amplitude response of the output transfer function is shown as equation (5.2). Likewise, equation (5.3) is for the rejection ratio.

$$Input(k-2) = Output(k-2) + Error(k) \tag{5.1}$$

$$|T(z)| = \frac{|F\{Output\}|}{|F\{Input\}|} \tag{5.2}$$

$$|E(z)| = \frac{|F\{Error\}|}{|F\{Input\}|} \tag{5.3}$$

5.2 Measured Rejection Ratio

The rejection ratio shows the amplitude of the following error for a given input frequency. The rejection ratio is only valid for analyzing the residual error when following the input signal because it combines the amplitude and phase response of the system. In other words, the rejection ratio is not applicable to the noise signal because the phase delay of noise is not meaningful. An exception to this is for the CAO implementation as shown in Figure 4.10. In that particular case only, the output quantization noise is augmented by the rejection ratio.

The TG used in these experiments generated significant turbulence power at frequencies higher that the bandwidth of the system. However, for a system to be useful as a scientific instrument it uses a sampling rate that is high enough that the significant turbulence power is lower frequency than the 0dB bandwidth. For comparisons, it will be assumed that the turbulence will be contained in the frequencies less than 3% of the sampling rate.

The actual system acts similarly to the models developed in Chapter 3. The theoretical rejection ratio has been drawn on the same plot as the measured rejection ratio for easy comparison. The Type 1 and 2 systems have far less noise on the measured plots than the CAO system. This was expected from the discussion of section 4.2.3. The largest difference between the model and the actual system is found in the Type 2 system. At low frequencies, the Type 2 system does not follow the 40 dB/decade slope. This is due to the effect of quantizing the output signal. Even if the input signal power was at the full

range of available actuator stroke, the error caused by quantization is on the order of 1%. This error translates to a –40 dB limit. Therefore, it is not surprising that the Type 2 system can not reduce the error below –35 dB. The portion of the rejection ratio that is not applicable to any meaningful signal is labeled on the plots as "N/A".

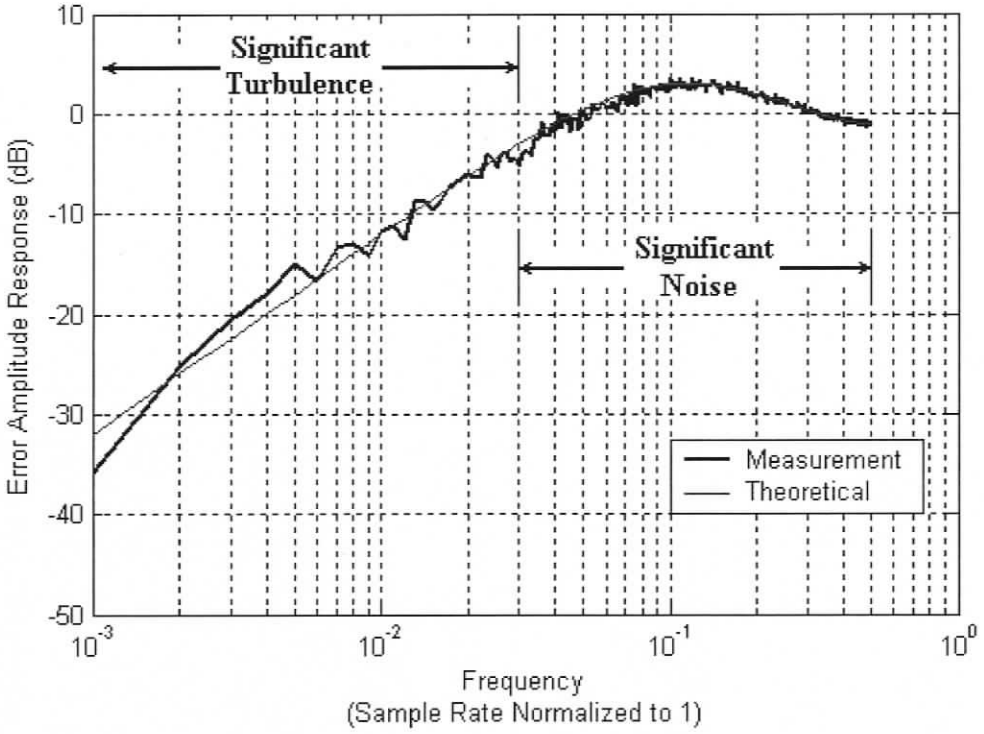

Figure 5.1: Measured rejection ratio of a 5th order mode for the CAO system

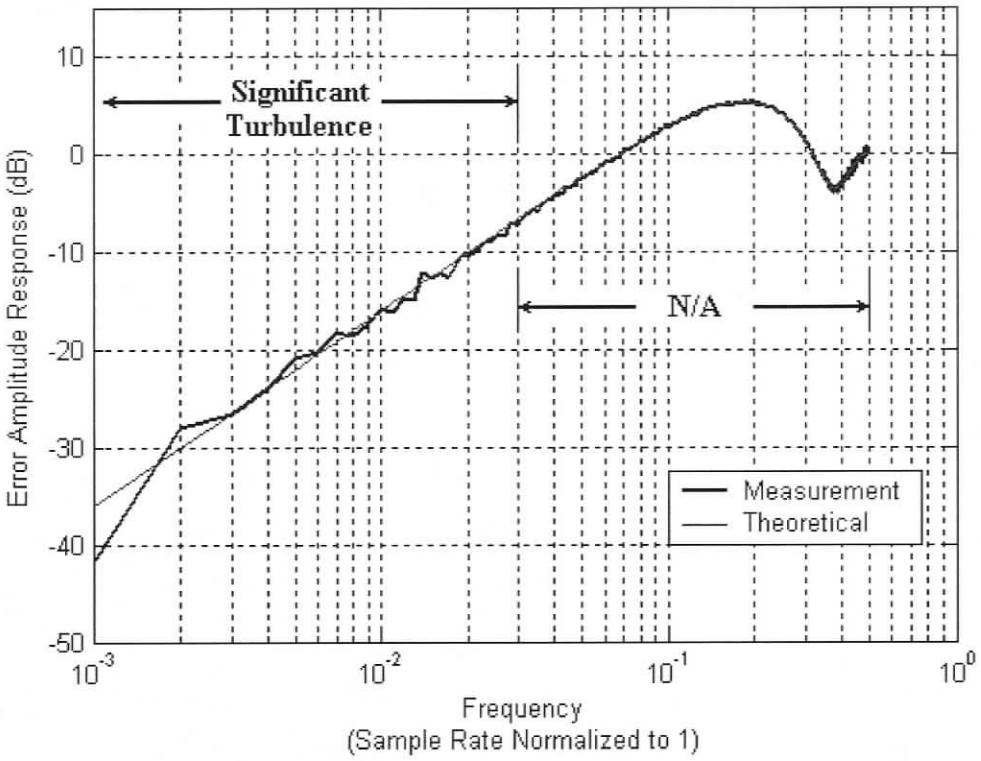

Figure 5.2: Measured rejection ratio of a 5th order mode for the Type 1 system

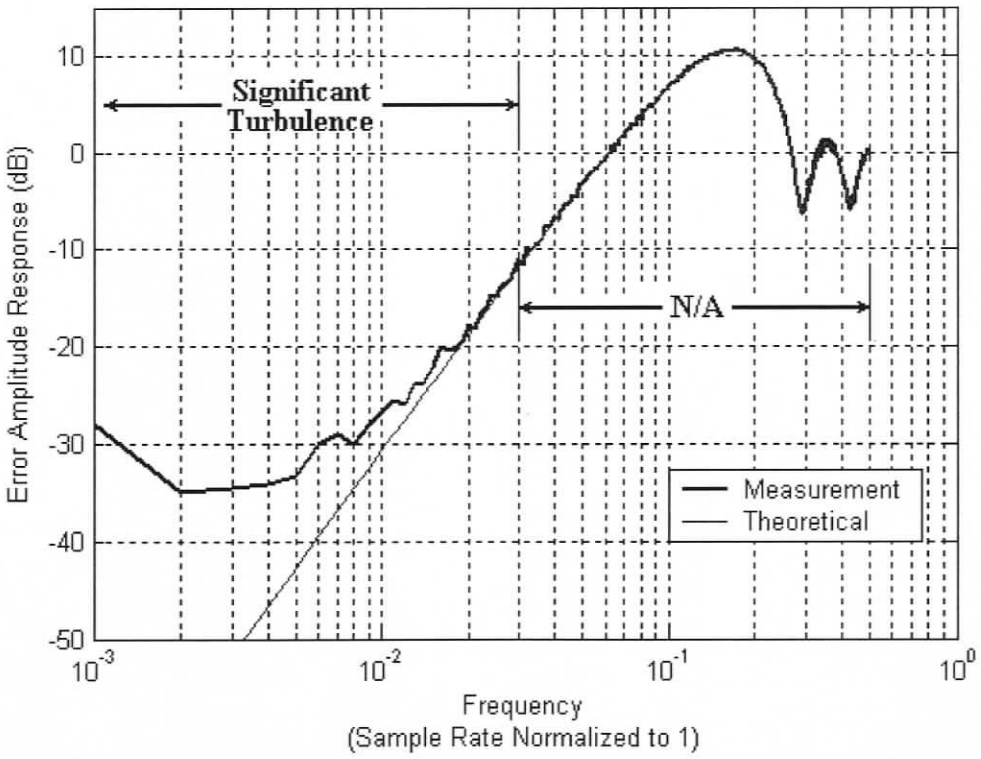

Figure 5.3: Measured rejection ratio of a 2nd order mode for the Type 2 system

5.3 DM Amplitude Response

The DM amplitude response to an input signal, as equation (5.2), is used to understand how the WFS noise affects the DM. The plot of the measured CAO system amplitude response follows the model, but with some significant noise. This shows that there may be a significant source of noise caused by the system as predicted in Section 4.2.3. The plots of the measured amplitude responses for the Types 1 and 2 systems followed the theoretical models very well with relatively little noise. An exception to this is the limit of the attenuation of the input signal at high frequencies. The actual Type 1 system is attenuating at the Nyquist frequency to a –20dB limit, or 10% of the input amplitude. It is likely that the system can not attenuate the signal further due to the coarseness of the output quantization. The Type 2 system is designed to not amplify the quantization error, but it can obviously amplify the WFS noise significantly.

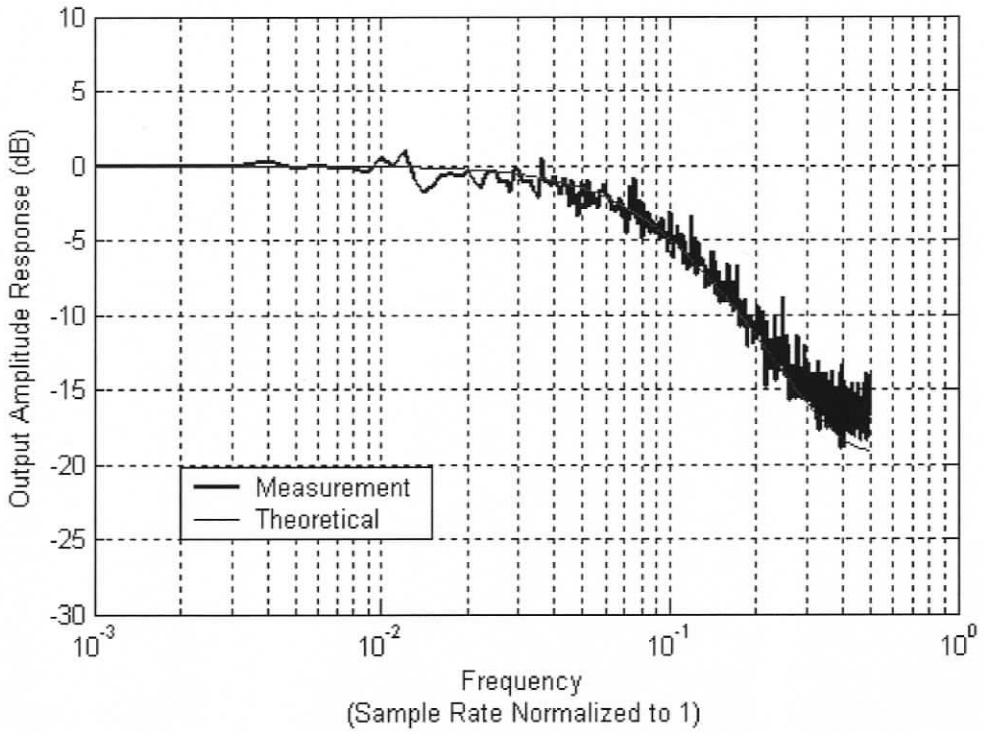

Figure 5.4: Measured amplitude response of a 5th order mode for the critically damped CAO system

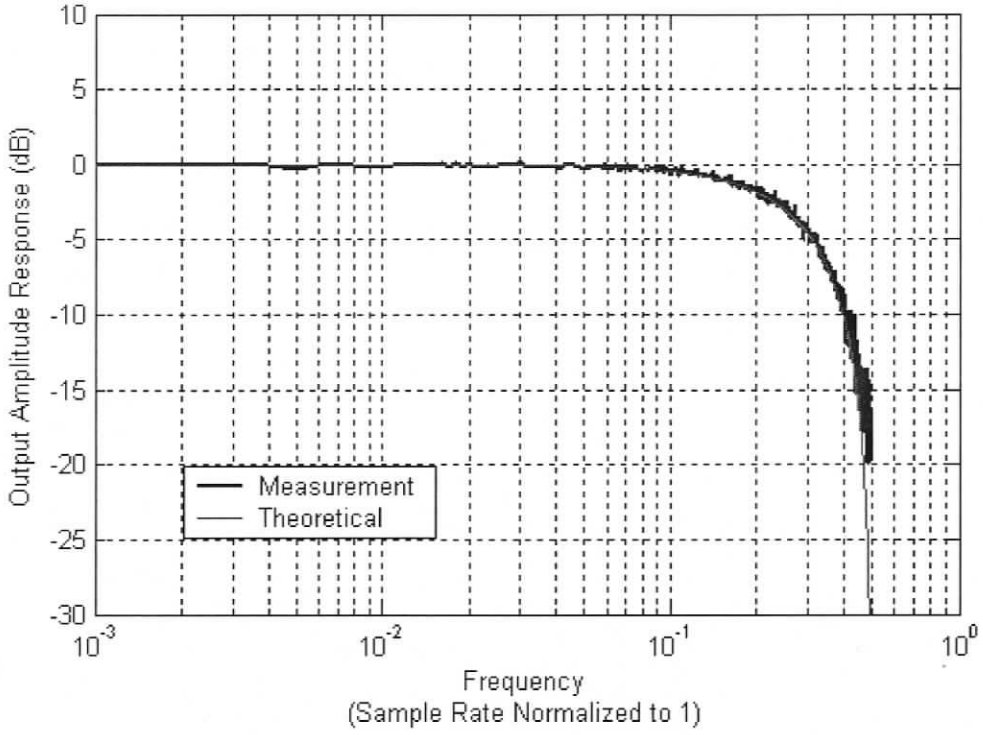

Figure 5.5: Measured amplitude response of a 5th order mode for the critically damped Type 1 system

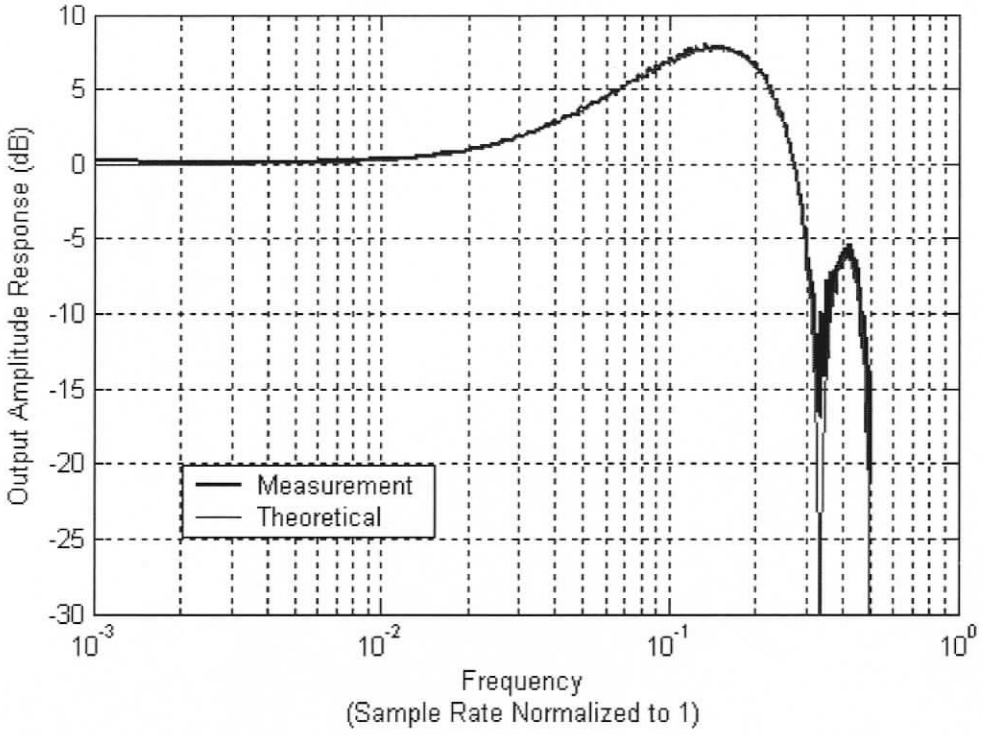

Figure 5.6: Measured amplitude response of a 2nd order mode for the critically damped Type 2 system

5.4 Corrected Image

The goal of this work is to correct for the distortions imposed on a beam of light by atmospheric turbulence. The following are some examples of a distorted image with its respective corrected image. The simulated image is the average of 261 frames to approximate a 1 second science camera exposure. The measured image is the average of 150,000 pictures to approximate the result of a 5 minute long exposure image. The simulated image is submitted only to give an example of short term turbulence and is not directly comparable to the measured example.

Figure 5.7: Simulated short exposure distorted image (left) and the Type 1 system corrected image (right)

The distorted image of Figure 5.7 is for a simulated short exposure of 1 second. In this simulated distorted image, the image is very dim and suggests that there may even be two objects. The simulated corrected image shows that a great deal of correction has been applied and the light is centered on a 2 by 2 pixel square.

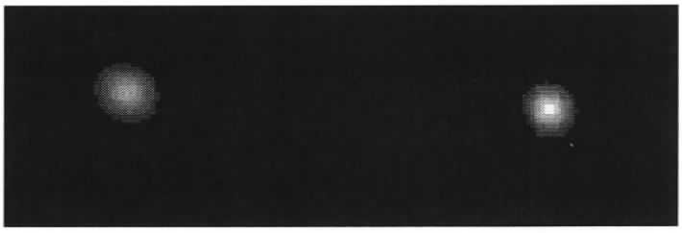

Figure 5.8: Measured distorted image (left) with the respective Type 1 system corrected image (right)

The improvement from the measured distorted image and the corrected image is not as large as that of the simulated results. There are a few reasons for this. One is that the simulated results are for turbulence that evolves at a rate that is appropriate for the system. The real system measurement has turbulence that is much higher frequency than the 0dB rejection ratio bandwidth, which causes following error. This was due to the temperature differences in the mixing chamber that were in excess of 100 °C. Another reason that the two figures are not directly comparable is that for a long exposure image, the random turbulence blurs into a bell curve shape (shown in Figure 5.9), so the short term distortions are lost.

Figure 5.9 shows a side profile of the intensities of the images, where a higher data point means that that the image is brighter on that pixel. The bell curve shapes relate to the probability distribution of where the light will hit the camera at a given moment. The corrected image has considerably more captured photons within a given radius.

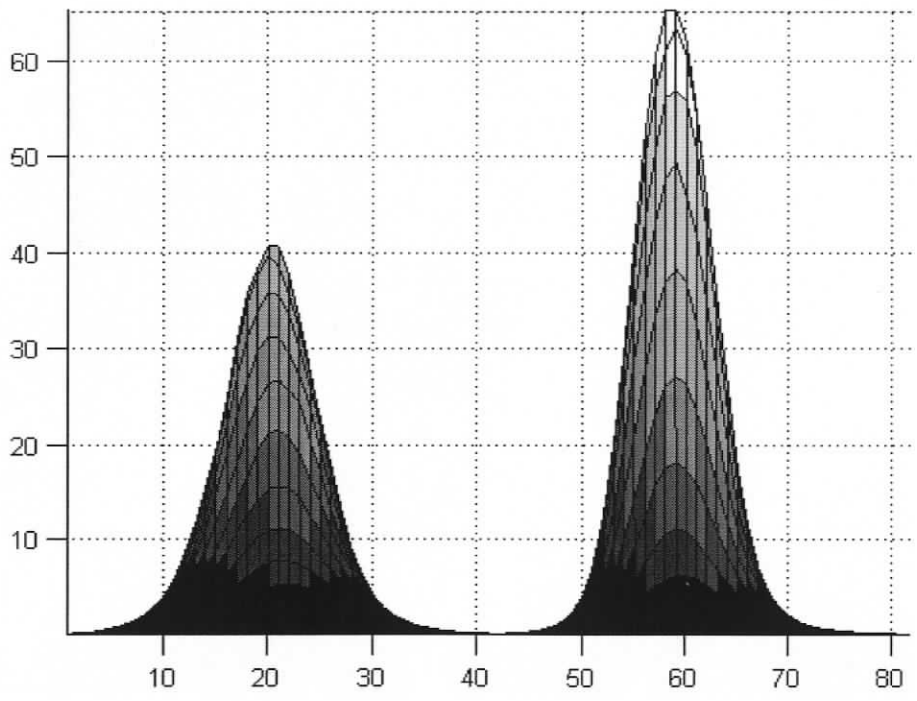

Figure 5.9: Measured profile of the distorted image (left) with the Type 1 system corrected image (right)

5.5 Conclusions

The Types 1 and 2 systems are behaving very close to the models designed in Chapter 3. There are two exceptions to this; (i) when the output quantization limits how closely the output can follow the input for the low frequency turbulence and (ii) when the output quantization is the limiting factor of the high frequency noise attenuation.

The critically damped Type 1 system theoretically passes more WFS noise to the DM than the critically damped CAO system. This is a natural trade off to obtain the higher bandwidth. However, the mismatch of the delay of the optical feedback path with the delay of the integrator in the CAO system causes noise. This effect was theoretically shown in Chapter 4 and supported by the presence of additional noise in the measurements shown in Figure 5.4. Output quantization should be a significant source of noise, if not the largest source, so the Type 1 AO controller can have less system noise than CAO.

The Type 2 system is stable and follows low frequency inputs very well. However, it reacts strongly to WFS noise. This predictive control scheme would only be useful if the system noise is reduced. An AO system must have the DM quantization noise as 4 times larger than the WFS noise to mask this negative effect to effectively use the Type 2 system for wave front correction.

The measured images show that the Type 1 system is capable of making some correction of the turbulence. In the shown example, the improvement of the maximum peak is only on the order of 50%. The main reason for this is that the significant power spectrum of the turbulence extended far beyond the 0dB bandwidth due to temperature differences in excess of 100 ^{o}C and this creates following error.

Chapter 6

Conclusions and Future Work

6.1 Conclusions

In Chapter 2 it was shown that the optical feedback loop of an AO system can be modeled as two sample delays. There are no significant dynamic effects found other than this delay. It was shown that the models for Altair, Keck and the simulated VLT-Planet Finder have similar modeling approaches. The conversion of these CAO continuous models to discrete models also shows an optical feed back model of two sample delays. This shows that other AO systems have similar dynamics to the AO system at the University of Victoria. Therefore, it is expected that the progress shown within this thesis as well as further AO control developments can be applied to AO systems that have the CAO model.

Commissioned CAO systems often have an optimizer for the gain. These optimizers use the model of the output transfer function and its rejection ratio to determine what gain would give the smallest error. These systems are often designed with the continuous model, which significantly loses accuracy above 10% of the sampling rate. Therefore, using the discrete output amplitude response shown in equation (2.16) could improve the gain optimization of CAO systems.

Chapter 3 presented a reduced form of the Sylvester matrix. The Sylvester matrix is always size $2n$ by $2n$, where n is the order of $A(z)$ or $B(z)$ (which ever is higher). The Reduced Sylvester matrix formulation uses a matrix that is $n+m-1$ by $n+m-1$ which is always smaller than the Sylvester matrix. This improvement was found because the Sylvester matrix is for the general case for arbitrary $A(z)$, $B(z)$ and $D(z)$. The reduced

method presented in section 3.2 is for digital control systems that will always have a_o = $a_o = d_o = 1$ and $b_o = 0$. The design example shown in section 3.3 would have been solved with a 4 by 4 Sylvester matrix, as opposed to 2 by 2 with the reduced form. The Type 2 control system was designed with a 6x6 Reduced Sylvester Matrix. It would require a 10x10 Sylvester Matrix for this task.

The critically damped Type 1 system provides 62.5% higher real bandwidth than the critically damped CAO system. This was accomplished with out amplifying any frequency beyond a factor of 1 (0dB). It is conceded that this method does not attenuate all the upper frequencies as well as the CAO method. However, this should not be a noticeable difference since the noise source is sensor quantization, and is followed by the output quantizer. The output should have coarser quantization than the input sensor so this effect should be hidden. Noise of these systems was also discussed in Chapter 4 and will be revisited shortly.

The Type 2 system has lower following error at low frequency by orders of magnitude over the other two presented systems. This is because Type 2 systems have 0 following error of ramp inputs and a low frequency signal can be approximated by a ramp over a short period of time. Its limitation is that it amplifies noise as well. This may be acceptable as the peak is approximately the same as when the gain is high in a CAO system.

In Chapter 4 it was shown that when the output signal is quantized, the system can have reduced oscillations between quantization steps if the residual error is used as a feedback signal within the controller. When this signal is added to the measured error, the result is similar to what would be expected if quantization never occurred. The

implemented Type 1 and Type 2 systems are shown as Figures 4.11 and 4.12 respectively. Both systems use the residual error within the controllers. This makes both systems insensitive to quantization noise. Such implementations also allow for tracking of the input when the computer output is in an over ride state.

The Zernike set of modes [3] is both complicated and not applicable to square grids at high spatial frequencies. The Legendre modes suggested by Southwell [19] is a complicated method to obtain a set of modes that are Cartesian based and orthogonal. The determination of the coefficients of multiples of 1D Legendre modes to develop an orthogonal set of 2D modes is unnecessary. This is because any orthogonalization process will automatically adjust the initial set of shapes to be orthogonal. The use of $x^m y^n$ as the initial shapes followed by an orthogonalization algorithm is a simple solution to obtain a set of modes that are appropriate for a square grid [18].

The plots shown in Chapter 5 show that the systems are behaving very close to the models designed in Chapter 3. Exceptions to this are caused by the output quantization. This limits how closely the output can follow the input as well as the amount of noise attenuation.

The critically damped Type 1 system theoretically retains more system noise than the critically damped CAO system. Unfortunately, the WFS system noise in this experimental system is larger than the output quantization, so this effect is not hidden. However, the mismatch of the delay of the optical feedback path with the delay of the integrator in the CAO system causes noise. Also, for a CAO system to obtain the same bandwidth as the Type 1 system, the gain must be increased and some frequencies of the noise become amplified. The measured images show that the Type 1 system is capable of

making corrections of the turbulence, even though the amount of turbulence is beyond what would be reasonable.

The Type 2 system is stable and follows low frequency inputs very well. However, the WFS is generating too much noise to effectively use the Type 2 system for wave front correction on this experimental set up. This system would only be useful if the WFS noise is reduced.

6.2 Future Work

The future of this research will be the implementation of a second DM into the system. This second DM will be a larger stroke DM that will have fewer actuators. Its job will be to correct for the low order modes. These modes have the highest power in atmospheric turbulence. A similar DM to the one used in this work will be used to correct for the small amplitude, high order modes.

The conversion of wave front data to actuator positions can be computationally intensive for mirrors with large numbers of actuators. Research into methods to reduce the computational complexity of the problem is necessary for mirrors with thousands of actuators.

Many commissioned AO systems have an adaptive process that tunes the gain of the CAO system to balance the bandwidth of each mode with the noise amplification to minimize the total error. The Type 1 system could have an adaptive system adjusting the two tap weights of the filter as well as the gain. This would give the system at least two degrees of freedom to find the optimum balance between bandwidth and noise.

Bibliography

[1] B. Wallace, *Design, Implementation and Testing of an Adaptive Optics Test-Bench*, University of Victoria, Victoria, British Columbia, Canada, 2005

[2] O. Keskin, *Hot Air Turbulence Generator for Multi-Conjugate Adaptive Optics*, University of Victoria, Victoria, British Columbia, Canada, 2003

[3] R.J. Noll, "Zernike polynomials and atmospheric turbulence," *J. Optical Society of America, Vol. 66, No.3*, Optical Society of America, pp. 207-211, March, 1976

[4] J. Hartmann, "An Improvement of the Foucalt Knife-Edge Test in the Investigation of Telescope Objectives", Translated from Sitzungsberichte der K. Preussichen Akademie der Wissenshaften Session of December 19, 1907

[5] R.K. Tyson, *Introduction to Adaptive Optics*, SPIE Press, Bellingham, Washington, USA, 2000

[6] P.J. Hampton, C. Bradley, A. Hilton P. Agathoklis, "Adaptive Optics Control System Development," *Proceedings of SPIE Vol. 5169*, SPIE, Bellingham, WA, USA, pp. 321-330, 2003

[7] P.J. Hampton, C. Bradley, P. Agathoklis, "Multiple Mirror Control," *Proceedings of SPIE Vol. 5490*, SPIE, Bellingham, WA, USA, pp. 1374-1383, 2004

[8] S. Haykin, *Adaptive Filter Theory, Fourth Edition*, Prentice-Hall, New Jersey, USA, 2002

[9] J.-P. Véran, M Smith, "Optimizer Detail Design Description", *Altair Software System Report*, Herzberg Institute of Astrophysics Internal Report, Victoria, BC, June 2003

[10] "VLT-Planet Finder - Adaptive Optics modal control modeling", Internal Report, May 2004

[11] K. Ogata, *Discrete-Time Control Systems, Second Edition*, Prentice-Hall, Inc., New Jersey, USA, 1995

[12] M.A. van Dam, D. Le Mignant, B. Macintosh, "Characterization of adaptive optics at Keck Observatory: part II", *Proceedings of SPIE Vol. 5490*, SPIE, Bellingham, WA, USA, pp.174-183, June, 2004

[13] D.S. Watkins, *Fundamentals of Matrix Computations*, John Wiley & Sons, Inc., New York, USA, 2002

[14] D. Williamson, K. Kadiman "Optimal Finite Wordlength Linear Quadratic Regulation," *IEEE Transactions on Automatic Control, Vol. 34. No. 12*, IEEE, pp. 1218-1228, December 1989

[15] J. Hao, G. Li, "Optimal ρ-realisation for digital controller implementation with stability consideration," *Electronics Letters* online no: 20040185, *Vol. 40. No. 4*, IEE, February 2004

[16] W. Xu, X. Hu, J. Chu, "An l_1-based Approach of Designing Optimal Structures of Finite Precision Digital Controller," *Conference on Control Applications Proceedings*, IEEE, pp. 760-763, 2003

[17] G. Dai, "Modal wave-front reconstruction with Zernike polynomials and Karhunen-Loève functions", *J. Optical Society of America, Vol. 13, No.6*, Optical Society of America, pp. 1218-1225, June 1996

[18] P.J. Hampton, C. Bradley, P. Agathoklis, "Modal Control Using a Deformable Mirror for Adaptive Optics", *IEEE Pacific Rim Conference on Communications, Computers and Signal Processing*, IEEE Catalog Number: 05CH37690C, IEEE, 2005

[19] W.H. Southwell, "Wave-front estimation from wave-front slope measurements," *J. Optical Society of America, Vol. 70. No. 8*, Optical Society of America, pp. 998-1006, August 1980